

ABSTRACT

JEVNIKAR, EVAN MCKAY. A Comprehensive Ontogenetic Analysis of *Tarbosaurus bataar* Provides Insight into Intraskelatal and Individual Variation of tyrannosaurid Growth (Under the direction of Dr. Lindsay Zanno).

Tyrannosaurs, especially *T. rex*, are some the largest land predators to exist and as a result ruled their end Cretaceous ecosystems. This success has been attributed to their exponentially rapid growth that appears to become increasingly accelerated in the latest-diverging taxa. However, how these dynamics vary throughout the skeleton and whether individual variation contributes to high developmental plasticity is unknown. Current studies on tyrannosaur growth are missing either high volume sampling of limb elements and individuals from different growth stages or computationally advanced methods needed to model growth accurately. Therefore, this study combines a robust multi-element sample of *Tarbosaurus bataar* from multiple growth stages with current model-fitting methods to understand how growth varies interskeletally and intraspecifically. By examining the same limb elements across multiple individuals, results show that *Tarbosaurus* deposits rapidly growing tissue for the majority of this species' life history. Cyclical growth marks (CGMs) varied significantly across all elements, except for the two youngest specimens, which support the idea that CGMs do not deposit exclusively on an annual basis and also support growth modulation in tyrannosaurs resulting from environmental stress. Growth curve reconstructions reveal that the femur, tibia, and fibula of *Tarbosaurus* show unique growth patterns, but the femur is the most accurate when CGM couplets are disregarded. Future work on extant animals centered around the ontogenetic relationship between limb-bone scaling and body mass increase, as well as the physiological cause and effects of CGM couplets, will be instrumental in furthering paleohistology.

© Copyright 2022 by Evan Jevnikar

All Rights Reserved

A Comprehensive Ontogenetic Analysis of *Tarbosaurus bataar* Provides Insight into
Intraskkeletal and Individual Variation of tyrannosaurid Growth

by
Evan McKay Jevnikar

A thesis submitted to the Graduate Faculty of
North Carolina State University
in partial fulfillment of the
requirements for the degree of
Master of Science

Biology

Raleigh, North Carolina
2022

APPROVED BY:

Lindsay Zanno
Committee Chair

Randall Langerhans

Brian Wiegmann

Holly Woodward

DEDICATION

This thesis is dedicated to my wife, McKenzie, and my parents, Nick and Stacy, who supported and encouraged me to fulfill my dream of studying paleontology.

BIOGRAPHY

My passion for paleontology is as fundamental to who I am as the color of my hair or the clothes I wear. My love of dinosaurs began early in life after watching the 1999 documentary, *Walking with Dinosaurs*. What captured my interest in this show was how creatures as massive, unique, and sometimes terrifying as dinosaurs were still just animals that had to eat, pass on their genes, and survive like any other animal you would see in the wild. From then on, I held to the singular goal of becoming a paleontologist and studying these ancient animals. It was a combination of hard work, unyielding determination, luck, support from my parents and family, and grace from God that I was able to travel from my hometown of Peoria, Arizona to the University of Kansas for college.

There in Lawrence, Kansas, my horizon expanded as I was introduced to a welcoming environment that fostered my academic growth and a group of friends that became family. I nervously stuck my foot in the door at the Biodiversity Institute on campus for the hopes of joining their paleontology team. Not only did their dinosaur paleontologist, Dr. David Burnham, welcome me immediately, he let me join their field team to dig in Montana and soon afterwards join their team as a lab assistant. Dr. Burnham graciously gave me opportunity after opportunity to communicate science to the public and grew this passion far beyond what I had imagined. To my surprise, I was lucky enough to continue this passion as a grad student at North Carolina State University with Dr. Lindsay Zanno and a lab I instantly connected with. While leaving my new home was a bittersweet goodbye, I knew it was the opportunity of a lifetime that would forever change my world.

Grad school was a whole new environment. I was surrounded by the smartest people I had ever interacted with and working at a level of science I didn't think was attainable. To be honest, I failed quite a lot throughout my time as a researcher. In fact, I feel as though I have failed more in these past two and a half years than in the entirety of my previous 16 years of schooling. But every failure was a lesson that built upon the last. Every lesson made me a better scientist. Every time I got better, I felt as though I could solve a problem more complex than the last. And now at the end of this degree, and with the guidance of Dr. Lindsay Zanno and so many other essential mentors, I can finally take pride in the paleontologist *and* the scientist that I have become.

ACKNOWLEDGMENTS

Almost the entirety of this research has taken place during the global pandemic caused by COVID-19. This pandemic restricted international travel to the IPMAS to collect required data for this project and left this project stalled for a brief period. The fact that this project was completed despite such a difficult situation, is a testament to all of those who put in the effort to support such a project. First among them, is Dr. Zanno, who continually advised this research and coordinated the processing and shipment of the *Tarbosaurus* individuals used in this study. Dr. Zanno also helped secure funding during summer sessions and an additional semester to finish this research due to setbacks from this pandemic. Another group of people essential to the success and development of this project are Dr. C. Tsogtbataar, Dr. K. Tsogtbataar, and the lab of the IPMAS who also coordinated the data collection, processing, and shipment of these specimens. This was all accomplished despite working with a reduced staff and facility due to restrictions put in place because of the pandemic. The team worked efficiently to ship specimens as quickly as possible before more restricted measures were put in place that would have stalled this project even longer. Additionally, the Mongolian Heritage is thanked for allowing permission to histologically sample MPC-D 100/70 and MPC-D 107/2. Both specimens were crucial in their position within the growth stages of *Tarbosaurus* and provided invaluable data for this study. My deepest thanks to all of you.

A very special thank you to Dr. H. Ballard-Woodward who hosted my visit to the OSU paleontology lab for histological consultation in addition to being a committee member for this thesis. Another special thank you to Dr. R. Langerhans and Dr. B. Wiegmann who offered guidance and were committee members for this thesis. Thanks to the Jurassic Foundation for

funding this research. Thanks to North Carolina State University and the North Carolina State Museum of Natural Sciences for access to facilities and equipment used to complete this study. Thanks to the continuous support and feedback of my fellow peers at the North Carolina State Museum of Natural Sciences. Thanks to Dr. E. Griffith for consultation on statistical methods. Thanks to Jack Myer Wood for silhouettes used in images.

TABLE OF CONTENTS

LIST OF TABLES	ix
LIST OF FIGURES	x
Chapter 1: Introduction	1
A Brief Background on Bone Biology	1
Evaluating Growth in Extinct Taxa	3
Skeletochronology (determining age)	4
Size Estimates	6
Approaches to Modeling Growth	9
Tyrannosauroid Growth	10
Life History of <i>Tarbosaurus</i>	15
References	20
Figures	31
 Chapter 2: Materials and Methods	 42
Specimens	42
Histological Methods	42
Descriptions	43
CGM Measurements	43
Mass Estimates	44
Growth Curve Reconstruction	45
References	48
Figures & Tables	50
 Chapter 3: Results	 53
Histological Descriptions	53
MPC-D 107/7	53
MPC-D 100/66	54
MPC-D 100/62	55
MPC-D 107/5	55
MPC-D 107/14	56
MPC-D 100/70	57
MPC-D 100/98	58
MPC-D 100/61	59
MPC-D 107/4	60
MPC-D 100/64	60
MPC-D 100/63	61
MPC-D 107/2	62
Annual Variation in CGM Spacing	63
Growth Curve Reconstructions	64
Variation Based on Locality	67
References	68
Figures & Tables	70
 Chapter 4: Discussion	 141

Histological Trends	141
Growth Mark Variation	142
Paleopathologies	144
Developmental Plasticity	145
Determining the Most Accurate Model	147
Comparing MPC-D 107/2 to FMNH PR 2081	148
Limitations in Method	149
Life History of <i>Tarbosaurus bataar</i>	151
References	153
Figures & Tables	157
Chapter 5: Conclusion	161
Appendices	163

LIST OF TABLES

Table 2.1	General Specimen Information	52
Table 3.1	Femur CGM circumferences	121
Table 3.2	Tibia CGM circumferences	124
Table 3.3	Fibula CGM circumferences	127
Table 3.4	Model Parameters	130
Table 3.5	Couplet Subsampled Model Parameters.....	134
Table 3.6	Annuli Subsampled Model Parameters	136
Table 3.7	All Age Estimates Produced from Models for <i>Tarbosaurus</i> Individuals.....	139
Table 3.8	Age Estimates and Confidence Intervals of <i>Tarbosaurus</i> Individuals.....	140
Table 4.1	CGM Types and Amounts Preserved in <i>Tarbosaurus</i> Limb Bones.....	160

LIST OF FIGURES

Figure 1.1	Examples of common bone tissue and complexes	31
Figure 1.2	Examples of common vascularization types	32
Figure 1.3	Histological section of a skeletally mature <i>T.rex</i> fibula	33
Figure 1.4	Retro-calculation of a specimen's age using the superimposition method and the non-linear modeling method	34
Figure 1.5	Histological section of skeletally immature <i>T. rex</i> femur and tibia	35
Figure 1.6	Histological section of <i>Moros intrepidus</i> femur in polarized light with lambda filter, natural light with numbered LAG circumferences, and polarized light	36
Figure 1.7	Linear regression showing the relationship between growth rate and body mass at skeletal maturity	37
Figure 1.8	Time calibrated phylogeny of <i>Tyrannosauroidae</i> with global occurrences and phylogenetic distribution of body sizes	38
Figure 1.9	Growth curve reconstruction of North American tyrannosaurids	39
Figure 1.10	Growth curve reconstructions for skeletally mature <i>T. rex</i> using peramorphic acceleration and Carcharodontosaurid using hypermorphosis	40
Figure 1.11	Gigantic Theropods	40
Figure 1.12	Nemegt Stratigraphic column including localities that preserve <i>T. bataar</i> fossils and a typical outcrop of the formation in Mongolia	41
Figure 2.1	<i>Tarbosaurus bataar</i> individuals used in this study	50
Figure 2.2	Graphical representation of different model shapes	51
Figure 3.1	Histological thin section of MPC-D 107/7 Femur under plain polarized light	70
Figure 3.2	Histological thin section of MPC-D 107/7 Tibia under plain polarized light	71
Figure 3.3	Histological thin section of MPC-D 107/7 Fibula under plain polarized light	72
Figure 3.4	CGMs found in MPC-D 107/7 under plain polarized light	73
Figure 3.5	Histological thin section of MPC-D 100/66 Femur	74

Figure 3.6	Histological thin section of MPC-D 100/66 Tibia	75
Figure 3.7	Histological thin section of MPC-D 100/66 Fibula.....	75
Figure 3.8	CGMs found in MPC-D 100/66	76
Figure 3.9	Histological thin section of MPC-D 100/62 Femur	77
Figure 3.10	Histological thin section of MPC-D 100/62 Tibia	78
Figure 3.11	Histological thin section of MPC-D 100/62 Fibula.....	79
Figure 3.12	CGMs found in MPC-D 100/62 under plain polarized light.....	79
Figure 3.13	Histological thin section of MPC-D 107/5 Femur	80
Figure 3.14	Histological thin section of MPC-D 107/5 Fibula.....	80
Figure 3.15	CGMs found in MPC-D 107/5 under plain polarized light.....	81
Figure 3.16	Histological thin section of MPC-D 107/14 Femur	81
Figure 3.17	CGMs found in MPC-D 107/14 Femur under plain polarized light	82
Figure 3.18	Histological thin section of MPC-D 100/70 Femur	83
Figure 3.19	Histological thin section of MPC-D 100/70 Tibia	84
Figure 3.20	Histological thin section of MPC-D 100/70 Fibula.....	85
Figure 3.21	CGMs found in MPC-D 100/70 under plain polarized light.....	86
Figure 3.22	Pathology found in medullary cavity of MPC-D 100/70 Femur.....	87
Figure 3.23	Histological thin section of MPC-D 100/98 Femur	88
Figure 3.24	Histological thin section of MPC-D 100/98 Tibia	89
Figure 3.25	Histological thin section of MPC-D 100/98 Fibula.....	90
Figure 3.26	CGMs found in MPC-D 100/98 under plain polarized light.....	90
Figure 3.27	Histological thin section of MPC-D 100/61 Femur	91
Figure 3.28	Histological thin section of MPC-D 100/61 Tibia	91

Figure 3.29 Histological thin section of MPC-D 100/61 Fibula.....	92
Figure 3.30 CGMs found in MPC-D 100/61 under plain polarized light.....	92
Figure 3.31 Histological thin section of MPC-D 107/4 Tibia	93
Figure 3.32 CGMs found in MPC-D 107/4 Tibia under plain polarized light	94
Figure 3.33 Histological thin section of MPC-D 100/64 Tibia	95
Figure 3.34 Histological thin section of MPC-D 100/64 Fibula from diaphysis.....	96
Figure 3.35 Histological thin section of MPC-D 100/64 Fibula near metaphysis.....	97
Figure 3.36 CGMs found in MPC-D 100/64 under plain polarized light.....	98
Figure 3.37 Histological thin section of MPC-D 100/63 Femur	99
Figure 3.38 Histological thin section of MPC-D 100/63 Tibia	100
Figure 3.39 Close up of a single microfracture undergoing secondary remodeling in MPC-D 100/63 Tibia	101
Figure 3.40 Histological thin section of MPC-D 107/2 Femur	102
Figure 3.41 Histological thin section of MPC-D 107/2 Tibia	103
Figure 3.42 Histological thin section of MPC-D 107/2 Fibula.....	104
Figure 3.43 CGMs found in EFS of MPC-D 107/2 under plain polarized light.....	104
Figure 3.44 Histograms showing CGM distances throughout femora	105
Figure 3.45 Histograms showing CGM distances throughout tibiae.....	106
Figure 3.46 Histograms showing CGM distances throughout fibulae.....	107
Figure 3.47 CGM distances proportional to the cortex depth within all elements	108
Figure 3.48 Histograms showing CGM distances throughout femora with couplet removed ..	109
Figure 3.49 Histograms showing CGM distances throughout tibiae with couplets removed ...	110
Figure 3.50 CGM distances proportional to the cortex depth within all elements with couplets removed.....	111

Figure 3.51 Growth model reconstructions using CGM circumferences	112
Figure 3.52 Growth model reconstruction of fibulae CGM circumferences including samples away from the mid-diaphysis	113
Figure 3.53 Growth model reconstructions using only LAG circumferences modeled	114
Figure 3.54 Growth model reconstructions using CGM circumferences with couplets averaged.....	115
Figure 3.55 Growth model reconstructions using estimated body masses	116
Figure 3.56 Growth model reconstructions using estimated body masses with only LAGs modeled	117
Figure 3.57 Growth model reconstructions using estimated body masses with couplets averaged.....	118
Figure 3.58 All possible body mass growth curve reconstructions based on figures	119
Figure 3.59 Body mass and age estimates with 95% confidence intervals	120
Figure 4.1 Examples of CGM couplet present within the sample	157
Figure 4.2 Growth curve reconstruction of FMNH PR 2081 and MPC-D 107/2.....	158
Figure 4.3 Selective sampling of growth data within this sample of <i>Tarbosaurus</i>	159
Figure 4.4 Best growth curve reconstruction with important life history events.....	159
Figure 5.1 MPC-D 107/7 before histological processing	163
Figure 5.2 MPC-D 100/66 before histological processing	164
Figure 5.3 MPC-D 107/5 before histological processing	165
Figure 5.4 MPC-D 100/62 before histological processing	166
Figure 5.5 MPC-D 107/14 before histological processing	167
Figure 5.6 MPC-D 100/70 before histological processing	168
Figure 5.7 MPC-D 100/98 before histological processing	169
Figure 5.8 MPC-D 100/61 before histological processing	170

Figure 5.9 MPC-D 107/4 before histological processing	171
Figure 5.10 MPC-D 100/64 before histological processing	172
Figure 5.11 MPC-D 100/63 before histological processing	173
Figure 5.12 MPC-D 107/2 before histological processing	174

CHAPTER 1: Introduction

A Brief Background on Bone Biology

Like modern-day animals, extinct tetrapods grew and metabolized in similar ways, thus cortical bone structures can qualitatively inform us about life history dynamics. Bone tissue in particular is very informative about bone apposition rates (Huttenlocker *et al.*, 2013) and can be broken down into several types based on collagen fiber orientation and osteocyte lacunae morphology (*sensu* Francillon-Vieillot *et al.*, 1990). Woven-fibered bone consists of randomly organized collagen fibers and rounded osteocyte lacunae that infer rapid appositional rates (Fig. 1.1).

Lamellar bone consists of thin, well-stratified collagen layers with thin osteocyte lacunae which instead indicate very slow appositional rates (Fig. 1.1). Intermediate to these is parallel-fibered bone where thin layers of collagen fibers are arranged in parallel patterns and osteocyte lacunae are moderately round (Fig. 1.1).

In addition to bone tissue, vascularization canals are also indicators of metabolism based on morphology (Fig. 1.2) (Huttenlocker *et al.*, 2013). As bone grows, the cortex is penetrated by blood vessels to provide nutrients, which can take many shapes and patterns; meaning that greater amounts of primary osteons, as well as higher degrees of anastomosis between canals, correlate with rapid growth (de Ricqlès, 1974; 1980). In contrast, avascular bone tissues represent slow to a near cessation of growth (de Ricqlès, 1974; 1980). Remodeling of tissue takes place in these canals as bone becomes more mature to re-metabolize old tissue for repair, bone shape change, or other biological processes (Huttenlocker *et al.*, 2013). As a result, these canals are filled with concentrically cemented rings of lamellar bone that have a scalloped edge and are defined as secondary osteons (Fig. 1.1).

From these cortical features, two common diagnostic complexes can be identified in bones to provide insight into the maturity of a specimen. The first, fibrolamellar bone (Fig. 1.1), is described in specimens where bone tissue is predominately woven-fibered with varying vascularization types (usually plexiform and reticular or occasionally laminar in slower growth; Enlow & Brown, 1957; Currey, 1960) and is characteristic of skeletally immature specimens that are rapidly growing (Currey 1987, 2003). The second complex known as Dense Haversian Tissue (Fig. 1.1) is characterized by dense packing of secondary osteons that entirely cover portions of primary bone (Huttenlocker *et al.*, 2013). When comparing similar bones, the proportion of primary bone that Haversian tissue covers correlates with specimen maturity, thus the oldest and most skeletally mature specimens are composed almost entirely of Haversian tissue (Persons *et al.*, 2019).

If an organism grows for longer than one year, it will deposit concentric features on an annual cycle within the bone cortex and therefore can be identified as a cyclical growth marker (**CGM**) (Castanet *et al.* 1993; Hutton, 1986; Castanet *et al.*, 1988, 1993; Tucker, 1997). Growth intervals can be broken down into zones, annuli, and lines of arrested growth (**LAGs**). A zone is a portion of bone that is actively growing and is commonly represented by fast-growing complexes (i.e., fibrolamellar). These portions of the cortex correspond to the majority of the annual cycle. An annulus is identifiable as a semi-distinct thin line with reduced vascularity and slower-growing tissue (i.e., lamellar bone); this feature corresponds to growth that has temporarily slowed but has not completely stopped (Padian *et al.*, 2004; Horner & Padian, 2004). However, a LAG is identifiable as a much more distinct line that is darker, has the slowest growing tissue, and has no

vascularity (Fig. 3). These features of LAGs are commonly found within annuli, thus representing a gradual slowing that completely stops and then gradually quickens. Thus, a combination of one zone and one annulus/LAG corresponds to a growth interval of one year (Castanet *et al.*, 1993; Hutton 1986). This pause in growth has been shown to correspond with environmental cues such as temperature, resource availability, and photoperiodicity that reoccur on an annual basis (Horner *et al.*, 1999; Castanet *et al.*, 2004; Köhler *et al.* 2012). The space between these LAGs is larger in young organisms as they quickly grow and then decrease in spacing as the organism ages and slows its growth (Chinsamy, 1993). Organisms vary in whether they have indeterminate or determinate growth. Indeterminate growth is when an organism effectively grows for their entire life (Padian & Stein, 2013). Determinate growth is the opposite condition in which an organism will achieve skeletal maturity and experience a near cessation in growth (Padian & Stein, 2013). Usually, animals that grow slower have indeterminate growth, like lepidosaurs and crocodylians (Padian *et al.*, 2001; Cubo *et al.*, 2012; Padian & Stein, 2013). Faster growing animals, like mammals and birds, display determinate growth (Erickson *et al.*, 2001; Padian *et al.*, 2001; Cubo *et al.*, 2012; Padian & Stein, 2013). When organisms that experience determinate growth achieve skeletal maturity, they drastically reduce the spacing of these growth markers near the periosteal surface (Cormack, 1987; Francillon-Vieillot *et al.*, 1990; Horner *et al.*, 2001; Klein & Sanders 2008). This near cessation of growth, known as an External Fundamental System (EFS) (Fig. 1.3), is described as a tightly packed stack of LAGs surrounded by avascular lamellar bone (Horner *et al.*, 1999; Horner & Padian, 2004; Woodward *et al.*, 2011; 2013; Lee *et al.*, 2013).

Evaluating Growth in Extinct Taxa

Evaluating the growth patterns of extinct taxa via histology involves collecting data on both the age of individuals and their size at a given age. These can then be combined via different approaches to generate growth curves, with different methods often yielding quite different results.

Skeletochronology (determining age)

Age is typically determined histologically by CGMs. As discussed, growth markers can occur in the form of LAGs or annuli. By counting the preserved number of LAGs and/or annuli in the cortex, one can observe the record of growth in an organism and determine its age (Chinsamy 1993; Horner *et al.* 1999, 2000; Erickson & Tumanova 2000). However, as a specimen grows, the medullary cavity in the bone expands and destroys earlier records of growth (Francillon-Vieillot *et al.*, 1990). This makes aging young organisms a relatively simple process but aging older organisms is more difficult. Therefore, much work has gone into being able to retro-calculate the age of a specimen.

Initial methods for reconstructing resorbed growth markers required examining a large ontogenetic series and superimposing all the specimens over each other (Chinsamy, 1993; Castanet, 1994; Erickson and Tumanova, 2000; Bybee *et al.*, 2006); younger specimens would fill in the gaps of the older specimens to provide an estimation of the missing growth intervals (Fig. 1.4). However, this method requires an assumption that all individuals in the ontogenetic series grew in nearly the same way, leaving individual variation unaccounted for. It also required a complete ontogenetic series for a species to make comparisons, which may not always be possible.

Further methods sought to account for individual variation by measuring the thickness of successive LAG spacing in each specimen (Horner and Padian, 2004; Klein & Sander, 2007; Xu *et al.*, 2007; Hubner, 2012). Because LAG spacing decreases with age, one could measure the rate at which the observable growth intervals are shrinking and then back-calculate to estimate the size of the initial larger growth intervals. Although an improvement upon the superimposition method by allowing for extrapolation of data, it assumes growth decreased at a constant rate for all of an organism's life and that the maximum amount of growth would have always been achieved in the first year of life.

A third more computationally involved method has been adopted in recent studies that fit a set of non-linear models to LAG circumferences and derives an estimate of the time elapsed between a hypothesized neonatal measurement and the current data (Cooper *et al.*, 2008; Lee *et al.*, 2013a; Lee *et al.*, 2013b; Woodward *et al.*, 2015) (Fig. 1.4). By comparing AIC scores of the models, each one can be tested to see how well it explains the data and thus the age of the specimen. Additionally, this method does not assume that each data point is independent and allows for accurate assessment of confidence intervals (Cooper *et al.*, 2008; Lee *et al.*, 2013b).

Recent work has shown that element choice and LAG count interpretation plays a huge role in skeletochronology results. Pedal elements, such as metatarsals and phalanges, preserve more variable LAG spacing suggesting they grow variably throughout life and are less reliable, while femora and tibiae LAG spacing is more uniform and consistent (Cullen *et al.*, 2014).

Additionally, smaller dinosaurs preserve the most accurate LAG counts in non-weight-bearing

bones such as ribs, gastralia, and the fibula, while larger dinosaurs preserve the most accurate counts in weight-bearing bones such as the femur and tibia (bones with accurate LAG counts are considered to contain the most LAGs within the cortex as a result of minimal remodeling; Cullen *et al.*, 2020a). The reason weight-bearing bones are more accurate in larger dinosaurs is that the rate of bone growth exceeds the rate of bone remodeling unlike smaller non-weight bearing bones (Padian *et al.*, 2016).

Several theropods have been recorded to occasionally deposit LAGs close together and leave only a small space in between each other producing double, triple, or even multiple LAGs (four or more LAGs) (Castanet, 1990; Xu *et al.*, 2007; Cullen *et al.*, 2014; Woodward *et al.*, 2020; Jin *et al.*, 2020; Cullen *et al.*, 2020a). Bone tissue between each LAG may not differ as it usually would between a zone and annuli, thus Multi-LAGs are commonly found in homogeneous bone tissue (Woodward *et al.*, 2013). If these growth markers do not encircle the entire circumference or at any point combine with other closely packed to create one single LAG, then these can be considered to be a single growth event (Castanet, 1990; Werning 2012; Cullen *et al.*, 2020a) (Fig. 1.5). When examining bone tissue under cross-polarized light, zone and annuli in the cortex can produce extinction patterns, thus counting up individual extinction patterns can be used to identify growth events when Multi-LAGs are present (Fig. 1.6) (Zanno *et al.*, 2019). Based on the above guidelines, Multi-LAGs are often interpreted as single growth events. Determining if each LAG is a separate growth event or if closely packed LAGs represent a single CGM introduces subjectivity in the evaluation of growth marker and zone counts and different workers have interpreted different numbers of CGMs within the same sections (Woodward *et al.* 2020; Cullen *et al.* 2020b).

Size Estimates

Modeling growth patterns and rates in extinct taxa requires not only the use of skeletochronology to determine absolute ages of individuals, but it also requires estimates of size at a given age.

Organismal size is often considered via proxy, such as the use of femoral lengths or circumferences, or these measurements may be used to generate estimates of an organism's mass, which is then used as a variable in growth curve reconstruction.

There are many ways to estimate the mass of an extinct organism. These can be divided into two main categories. Volumetric methods, as the name implies, derive estimations based on the volume of 3D scale models (Henderson, 1999; Seebacher, 2001; Christiansen & Farina, 2004). 3D models require nearly complete knowledge of the skeleton to estimate body shape as well as the density of any air sacs, skin, and other soft tissue structures (Alexander, 1989; Hurlburt, 1999; Christiansen, 1998). A major criticism of volumetric methods comes from their reliance on reconstructions that require estimating the weight of soft tissue structures, all of which are extremely rare in the fossil record. This can provide radically variable estimates for the same specimen depending on the arbitrary choices for soft tissue density (Campione & Evans, 2012). Another major criticism of these methods is the rigor in using these types of models; such calculations are often time-consuming and mathematically strenuous, which has led to these studies often relying on small sample sizes (Christiansen & Farina, 2004 was the largest volumetric study with only 16 samples). These methods may be more reliable for extinct organisms with very closely related extant species or analogs with very similar morphology (Hurlburt, 1999); however, the unique morphology of non-avian dinosaurs leaves much of these reconstructions up for debate. Volumetric methods are considered less effective than limb-

scaling because they: 1) do not take into account small theropods, 2) are more prone to arbitrary reconstructions, 3) are less accurate when estimating the mass of ratites (who share bauplans similar to non-avian theropods) and 4) do not account for all postures in bipedality (e.g., humans vs. birds) (Campione *et al.*, 2014).

Alternatively, limb-scaling methods examine the linear regression between limb measurements and the live weight of extant animals and apply this regression to extinct animals (Anderson *et al.*, 1985). Circumferences of stylopodial elements (humerus and femur for quadrupeds, femur for bipeds) produce the closest correlation with mass since a larger circumference is better equipped to handle the stress of weight and strenuous activity (Maloiy *et al.*, 1979). This method was initially met with heavy criticism due to claims that animals were so vastly different in size, shape, and posture to be considered reliable for estimation (Blob & Biewener, 1999; Rubin & Lanyon, 1984; Carrano, 2001; Packard *et al.*, 2009). However, robust sampling across all clades of animals, sizes, and body types revealed that femoral and humeral circumferences universally scale with mass (Campione *et al.*, 2012). Thus, body mass estimates based on limb-scaling of stylopodia circumference are the most effective method and, conveniently, the simplest method too.

An early study in *Psittacosaurus mongoliensis* mass estimation by Erikson and Tumanova (2000) stated that body mass estimates are not as accurate in skeletally immature individuals as they are for skeletally mature individuals. The methods of Anderson and team (1985) did not account for any growth stage other than skeletally mature individuals, thus would not be indicative of the interspecific variation in growth (Calder, 1984). Their proposed method,

Developmental Mass Extrapolation (DME), cubed their mass estimate proxy for each *Psittacosaurus mongoliensis* specimen, found what percentage of skeletally mature size this specimen was, and multiplied the skeletally mature size by this percentage to find the mass at the specimen's respective growth stage. By applying DME to mass estimates derived from limb-scaling equations, a seemingly more accurate assessment of masses can be obtained for growth studies. However, this method has been criticized because it has never been tested on extant species and there has been no study showing that limb-scaling is more or less accurate when examining skeletally immature individuals (Mhyrvold, 2013).

Approaches to Modeling Growth

Once an ontogenetic series of specimens has been aged, a growth curve can be constructed for the species by graphing age against a measure of size in two ways. The Whole Bone method (sensu Chinsamy, 1993) plotted each specimens' age at death with a selected whole bone measurement (e.g., femoral length or circumference, etc.) or mass estimate and fit these data points with an asymptotic regression (Erickson *et al.*, 2001; Cooper *et al.*, 2008). However, this method only captured one moment of each specimen's growth, leaving most of the growth data missing (Mhyrvold, 2013). The Longitudinal method (sensu Woodward, 2005) is a more comprehensive method that plots each LAG circumference its mass estimate with the age of these respective measurements calculated using the non-linear modeling described above. Combining multiple growth trajectories from an ontogenetic series can create a composite growth curve for the species (Lee & O'Connor, 2013). This can be done by lining up overlapping trajectories by eye or by using least-squares optimization to provide a more objective synthesis of the trajectories (Mhyrvold, 2013). Finally, these data points are fit with a suite of non-linear

models (much like the methods used for retro-calculation) to determine the most likely growth curve.

Tyrannosauroid Growth

Because of the phylogenetic position of dinosaurs within Archosauria, there has long been debate as to whether dinosaurs grew slowly like basal reptiles (Case, 1978), quickly like their extant representatives (endothermic birds) (Bakker, 1986), or displayed transitional qualities in their growth (Reid, 1997). Initial histological studies found that the bone cortex of several phylogenetically distant dinosaurs all contained fibrolamellar bone and Haversian systems (Enlow & Brown, 1957; Currey, 1960; Tarlo & Mercer, 1968), suggesting that dinosaurs did not grow like ectothermic reptiles, but instead grew rapidly (Bakker, 1972). Later studies expanded on this by showing that, the cortex of smaller, younger dinosaur individuals was composed largely of fibrolamellar bone, whereas larger, older individuals transitioned to a cortex composed of lamellar bone with decreasing vascularity (Chinsamy, 1990, 1993; Varrichio, 1993). The fossilized bones of dinosaurs also showed cyclical deposition of zones and annuli like modern endotherms (Enlow, 1969; Castanet & Cheylan, 1979; de Ricqlès, 1976, 1980; Hutton 1986). These results strongly suggested that dinosaurs grew in an asymptotic fashion: achieving rapid growth in early life and eventually slowing as they matured.

Dinosaurs were commonly thought to have lived several decades or even centuries because of the assumption that they grew slowly like reptiles yet attained massive sizes (Erickson 2005). However, examination of growth markers and LAG counts within the bone microstructure show that dinosaurs had a variety of lifespans that were shorter than originally anticipated. Large

sauropods lived from 41-55 years, the longest of any dinosaurs (Sanders *et al.*, 2011b), whereas derived ornithopods and ceratopsians lived an estimated 13-18 years (Cooper *et al.*, 2008; Erickson & Druckenmiller, 2011). Estimated theropod lifespans range vastly: the largest theropods lived 28-53 years (Cullen *et al.*, 2020b), theropods 1,000-3,000 kg in size lived around 20 years (Bybee *et al.*, 2006; Erickson *et al.*, 2001; 2006), smaller theropods weighing under 1,000 kg lived 5-18 years (Chinsamy 1990; Erickson *et al.*, 2007; Zanno *et al.*, 2019), and theropods only weighing a few kilograms living 1-3 years (Erickson *et al.*, 2001; Prondvai *et al.*, 2018). Coupling these ages with histological data further supported the idea that dinosaurs grew rapidly. Studies on dinosaurian growth curves have shown that they achieve growth rates that are greater than those of any extant reptiles, much like mammals and birds. (Chinsamy 1990, 1993; Curry, 1999; Erickson & Tumanova, 2000; Horner *et al.*, 2000; Padian *et al.*, 2001) (Fig. 1.7). Larger dinosaurs (e.g., sauropods and ornithischians) grew at rates comparable to modern eutherians and precocial birds, while smaller basal dinosaurs grew relatively slower, like modern marsupials (Erickson *et al.*, 2001; Padian *et al.*, 2001) (Fig. 1.7).

Among all dinosaurs, the growth of certain clades has been the subject of more research. Examination of sauropods stems from their gigantic body sizes and their exaggerated growth rates (Sander *et al.*, 2004; Woodward & Lehman, 2009; Cerda *et al.*, 2017). Hadrosaurs and other ornithopods have received special attention as well for their abundance, with multiple studies examining populations from bone beds, resulting in easier access to destructively sample and more detailed studies from this abundance (Horner *et al.*, 1999; Horner *et al.*, 2000; Cooper *et al.*, 2008; Woodward *et al.*, 2015). Theropods have received the majority of attention in histological studies, with nearly every major clade being sampled in an effort to understand the

timing of avian-style growth rates (Varrichio, 1993; Padian *et al.*, 2001; Erickson *et al.*, 2001; Erickson *et al.*, 2007; Cubo *et al.*, 2012; Erickson *et al.*, 2014; Prondvai *et al.*, 2018; Cullen *et al.*, 2020b) and patterns associated with gigantism, including a theropod clade having obtained some of the largest body sizes among predatory dinosaurs—Tyrannosauroida.

In contrast to the extensive research that has been conducted on the histology and growth of late-diverging, Late Cretaceous tyrannosaurids, the life history of the earliest diverging tyrannosauroids is only poorly known. To date, the only non-tyrannosaurid tyrannosauroids that have been studied histologically are *Guanlong wucaii* (from the Late Jurassic Shishugou Formation in China; Xu *et al.*, 2007), *Moros intrepidus* (from the Early Cretaceous Mussentuchit Member of the Cedar Mountain Formation; Zanno *et al.*, 2019), and *Suskityrannus hazelae* (from the Early Cretaceous Lower Member of the Moreno Hill Formation; Nesbitt *et al.*, 2019) (Fig. 1.8). The growth patterns of these taxa are distinct from those of later-diverging tyrannosaurids. These diminutive species (<37kg) display parallel-fibered tissue with simple longitudinal, reticular, and circumferential vascularity (Xu *et al.*, 2007; Zanno *et al.*, 2019; Nesbitt *et al.*, 2019). LAG counts of a skeletally mature *Guanlong wucaii* individual indicate that this species attained skeletal maturity at seven years old with no tyrannosauroid specimen growing older than 12 (Xu *et al.*, 2007). Although these results may not be indicative of larger tyrannosauroids like *Yutyranus huali* or *Sinotyrannus kazuoensis* due to a lack of sampling, it suggests that small tyrannosauroids had a slow to moderate growth pattern for most of their evolution.

However, later on in their evolution, tyrannosauroids seem to have achieved much more rapid growth, as evidenced by the presence of fibrolamellar bone with laminar and plexiform

vascularity in tyrannosaurids (Erickson *et al.*, 2004; Erickson *et al.*, 2006; Brusatte *et al.*, 2009; Cullen *et al.*, 2020b). Tyrannosaurids seemingly also employed a sigmoidal growth pattern in which growth was relatively slow in early life, accelerated after about 10 years to a much more rapid growth stage, and finally began to asymptote at around age 16-18 (Cullen *et al.*, 2020b). Non-tyrannosaurini tyrannosaurids (Fig. 1.8) would have achieved sizes double or triple that of tyrannosauroids of the same age and would have matured at estimates of 500-2,900 kg (Erickson *et al.*, 2004).

Of the tyrannosaurids, the gigantic size of *Tyrannosaurus rex* has made aspects of its life history a point of interest in paleontology. Initial studies histologically examined femora, tibiae, fibulae, and ribs of *T. rex* across several size classes (Erickson *et al.*, 2004; Horner & Padian, 2004). These studies found that even at large sizes (MOR 1125 mass et. = 6100kg), all specimens contained fibrolamellar tissue and vascularization that is laminar and radial that frequently changes to plexiform vascularization (Erickson *et al.*, 2004; Horner *et al.*, 2004). The largest and oldest specimens (e.g., FMNH PR 2081 mass et. = 8500kg) preserved varying amounts of lamellar bone, Haversian systems, and even an EFS, signaling that these specimens achieved skeletal maturity (Erickson *et al.*, 2004; Horner *et al.*, 2004; Persons *et al.*, 2019; Cullen *et al.*, 2020).

An initial growth curve produced by Erickson and team (2004) using the whole bone method (Fig. 1.9), found that *T. rex* also utilized a sigmoidal growth pattern that plateaued at 20 years of age and exhibited growth rates of up to 767 kg/yr. Although growth rates from this study were subsequently found to be miscalculated (Myhrvold, 2013), microstructure transitions corroborate

with this timeline and the sigmoidal growth pattern has been validated by Cullen *et al.*, (2020b) using the longitudinal method (Fig. 1.10). Cullen *et al.*, (2020b) reexamined growth rates of this species and found that *T. rex* achieved estimated growth rates of 319.14 kg/yr before reaching skeletal maturity. Such growth rates are comparable to some of the faster-growing altricial birds (Fig. 1.7)

What is more interesting about the growth of *T. rex* is how it relates to the macroevolution of theropod life history. Erickson *et al.* (2004) compared the growth pattern of *T. rex* to that of other North American tyrannosaurids and found that *T. rex* had a noticeably accelerated growth curve (Fig. 1.9); within the same amount of time, more basal species achieved only a fraction of *T. rex*'s size at skeletal maturity (Erickson *et al.*, 2004). *T. rex* was able to achieve extreme gigantism due to peramorphic acceleration of their growth trajectory, meaning successive species increased their growth rates while maintaining the same life span. Cullen *et al.*, (2020b) histologically examined a suite of other theropods, including a gigantic carcharodontosaurid, and found that theropods grew in two separate ways. Earlier-diverging theropods (e.g., allosauroids and carcharodontosaurids) grew more isometrically and utilized hypermorphosis to attain gigantism (Fig. 1.10), thus successive species maintained the same growth rate yet grew for longer periods of time. Later-diverging theropods (i.e., coelurosaurs) utilized accelerated growth (Fig. 1.10) to achieve similar sizes. These results showed that gigantism was achieved in two independent ways by exaggerating these different growth trajectories (Cullen *et al.*, 2020b).

Gigantism in theropod predators is well documented in non-coelurosaurs (Fig. 1.11) (Coria & Saldago, 1995; Coria & Currie, 2006; Brusatte & Sereno, 2007; Ibrahim *et al.*, 2014); however,

T. rex is currently the only theropod predator known to utilize this accelerated sigmoidal growth pattern to attain gigantism. Significant phylogenetic gaps in the study of tyrannosaur growth currently prevent us from being able to determine whether highly accelerated growth rates are autapomorphic for *Tyrannosaurus rex* or evolved in tandem with extreme gigantism in the clade. If the latter pattern is true, it provides key information on how coelurosaurian theropod dinosaurs achieved gigantism more generally and provides information on large-scale evolutionary and physiological processes in the clade. One way to explore the evolutionary timing, phylogenetic distribution, and mass correlates of accelerated growth in tyrannosaurid theropods, that has yet to be conducted is to examine growth patterns in the closest relative of *T. rex*—*Tarbosaurus bataar*.

Tarbosaurus bataar lived during the Maastrichtian Stage of the Late Cretaceous (70.6 – 68 myr ago; Maleev, 1955) in what is now Mongolia and China. The species is hypothesized to be the sister taxon to *T. rex* in most phylogenetic studies (Loewen *et al.*, 2013; Zanno *et al.*, 2019; Nesbit *et al.*, 2019) and has even been considered by one researcher to be congeneric with *Tyrannosaurus* (Carr *et al.*, 2005). *Tarbosaurus* is known from an unusually high number of specimens (>30) of presumably multiple age classes and recovered from multiple localities within the Nemegt Formation (Maleev, 1955; Rozhdestvensky, 1965; Carpenter, 1992; Carr, 1999) (Fig. 1.12). Additionally, *T. bataar* is both phylogenetically and chronostratigraphically younger than *T. rex*. Thus, this species represents a transitional species between smaller, basal, North American tyrannosaurids, like *Daspletosaurus torosus* (max femur length = 940mm; Lu *et al.*, 2014), and *T. rex* (max femur length = 1350mm; Persons *et al.*, 2019). Due to all these factors, *T. bataar* is an exemplary taxon to explore growth trajectories in late diverging tyrannosaurids and yet, to date, little histological analysis has been conducted on this species.

Life History of *Tarbosaurus*

The life history of *Tarbosaurus* has been the center of much debate for nearly 40 years. The first Nemegt tyrannosaur remains (PIN 551-1) were originally thought to be a species of *Tyrannosaurus* based on their robust morphology and size and were classified as *Tyrannosaurus bataar* (Maleev, 1955a). After the initial discovery of PIN 551-1, three other large to mid-sized tyrannosaurs were discovered in the Nemegt formation, all with different taxonomic classifications based on size and a suite of apparent morphological differences (Maleev, 1955b). Maleev (1955b) believed that the largest of these three specimens, PIN 552-1, was a different genus called *Tarbosaurus efremovi*, and the smaller two, PIN 553-1 and PIN 552-2, were more basal tyrannosaurids known as *Gorgosaurus lacinator* and *Gorgosaurus novojilovi*, respectively. Later examination by Rozhdestvensky (1965) found that all four of these species were different growth stages of the same species and the anatomy was not as different as previously stated. These specimens were still diagnostic enough to be distinguished from the North American *Tyrannosaurus rex* and so all four specimens were classified as *Tarbosaurus bataar* (Rozhdestvensky, 1965). These specimens were later re-examined and PIN 522-2 (formerly known as *Gorgosaurus novojilovi*) was considered to be a unique species known as *Maleevosaurus novojilovi* this time being diagnosed based on the morphology of the rostral skull bones (Carpenter, 1992). However, careful examination of ontogenetic changes in *Albertosaurus* skull morphology revealed that the apparent differences in *Maleevosaurus* could be explained by ontogenetic variation and was once again classified as a skeletally immature *Tarbosaurus bataar* (Carr, 1999).

Only two specimens of *T. bataar* have been histologically sampled, both of which are skeletally immature near the age of three (Tsuihiji *et al.*, 2011; Fowler *et al.*, 2011). The first specimen, LH PV18, was initially described as a separate species dubbed *Raptorex kirgsteini* and was supposedly discovered in the Lujiatun Beds of the Lower Cretaceous Jehol Group (Serenó *et al.*, 2009); however, the specimen was bought in the USA, so the describing team did not actually discover the specimen in situ (Fowler *et al.*, 2011). Histological analysis showed the specimen was composed almost entirely of fibrolamellar bone, a thin layer of lamellar bone near the periosteal surface, and contained three LAGs throughout the cortex. The lamellar bone layer and the spacing of the outermost LAG in relation to the second LAG suggested that it had recently undergone exponential growth. Based on this interpretation, the original authors hypothesized that two more LAGs were erased from medullary cavity expansion and would therefore make this specimen a sub-adult between five and six.

The second specimen, MPC-D 107/7, was found in the Bugin Tsav locality within the Nemegt Formation of Mongolia (Fig. 1.12) yet was nearly identical in morphology and size to LH PV18 (Tsuihiji *et al.*, 2011). This specimen was interpreted as a skeletally immature *T. bataar* based on its stratigraphic position and a suite of cranial autapomorphies that it shared with skeletally mature specimens. Histological analysis found two LAGs within the left fibula and three LAGs in the left tibia. The fibula had minimal remodeling due to an absence of a medullary cavity and only small amounts of secondary osteons, making the LAG counts reliable and without the need for retro-calculation. Based on the presence of a medullary cavity, the tibia was retro-calculated by fitting LAG circumferences to a linear difference equation and back-calculated to find the neonatal size and the time that had passed since then (Cooper *et al.*, 2008). Their analysis

concluded that the age of the specimen was between two and three. By retro-calculating this specimen, a neonatal *T. bataar* would have been roughly 14 kg.

This study led Fowler *et al.* (2011) to reevaluate the previous interpretation of LH PV18. Careful examination of the femoral section found that the bone tissue was similar to that of MPC-D 107/7 (Tsuihiji *et al.*, 2011). If the specimen truly was a sub-adult, it would need to display some level of Haversian tissue (Francillon-Vieillot *et al.*, 1990; Horner *et al.*, 2001; Klein & Sanders 2008) and if it was from a smaller species, it would display both smaller LAG spacing and relatively less vascularization (Padian *et al.*, 2001). Not all of these criteria were met; therefore, it was considered to be a skeletally immature individual of a larger species. Retro-calculation of the section confirmed the immature status of the specimen by estimating an age between two and three as well. However, the taxonomic identity of the specimen was challenged based on associated fish material that is consistent with an origin in the Nemegt Formation rather than in the Jehol Group, leading the authors to believe that *Raptorex* was to be considered *nomen dubium* and LH PV18 was actually another skeletally immature *T. bataar*. These histological studies, although limited, give us a glimpse into the early ontogeny of *T. bataar*. However, outside of these two specimens, no other *T. bataar* has been histologically examined, leaving the growth dynamics for this species unknown.

Here I provide histological descriptions of hind limb elements (femur, tibia, and fibula) from a large ontogenetic sample (12 individuals) of *Tarbosaurus bataar*. I then compare and contrast the histological microstructure and skeletochronology of individuals based on these various elements, providing new information on how bone microstructure varies between individuals,

throughout ontogeny, and between elements, as well as how skeletal element choice affects age estimates in theropods. I then reconstruct the growth dynamics of *T. bataar* and contrast growth curves derived from: 1. different hind limb elements; and 2. different interpretations of growth markers to better understand how subjectivity in interpreting CGMs affects results and provide a range of growth estimates based on maximum and minimum numbers of interpreted CGMs in the sample. These data provide new information on the life history of *T. bataar* as well as the timing of growth rate acceleration in tyrannosaurs.

REFERENCES

- Alexander RM (1989) “*Dynamics of Dinosaurs and Other Extinct Giants*” Columbia University Press
- Anderson JF, Hall-Martin A, Russell DA. (1985). “*Long-bone circumference and weight in mammals, birds and dinosaurs.*” J. Zool. Soc. Lond. A 207:53–61
- Bakker, R.T. (1972) “*Anatomical and Ecological Evidence of Endothermy in Dinosaurs*” Nature (238)
- Bakker, R.T. (1986) “*The Dinosaur Heresies*”, William Morrow
- Blob RW, Biewener AA (1999) “*In vivo locomotor strain in the hindlimb bones of Alligator mississippiensis and Iguana iguana: implications for the evolution of limb bone safety factor and non-sprawling limb posture.*” J Exp Biol, 202:1023-1046.
- Brusatte, S.L. and Sereno, P.C. (2007). "A new species of *Carcharodontosaurus* (dinosauria: theropoda) from the Cenomanian of Niger and a revision of the genus." Journal of Vertebrate Paleontology, 27(4):.
- Brusatte S.L., Carr T.D., Erickson G.M., Bever G.S., Norell M.A. (2009) “*A long-snouted, multihorned tyrannosaurid from the Late Cretaceous of Mongolia*” PNAS 106: 17261–17266
- Bybee PJ, Lee AH, Lamm ET. (2006) “*Sizing the Jurassic theropod dinosaur Allosaurus: assessing growth strategy and evolution of ontogenetic scaling of limbs.*” J. Morphology. 267:347–59
- Calder WAI (1984) “*Size, Function, and Life History Cambridge*” Harvard University Press
- Campione N.E., Evans, D.C., Brown, C.M., Carrano, M.T. (2014) “*Body mass estimation in non-avian bipeds using a theoretical conversion to quadruped stylopodial proportions*” Methods in Ecology and Evolution, 5, 913–923

- Campione NE, Evans DC. (2012) “*A universal scaling relationship between body mass and proximal limb bone dimensions in quadrupedal terrestrial tetrapods*” *BMC Biology*. 10:60
- Carpenter K, (1992) “*Tyrannosaurids (Dinosauria) of Asia and North America*” *Aspects of Nonmarine Cretaceous Geology*.
- Carr TD (1999) “*Craniofacial ontogeny in Tyrannosauridae (Dinosauria, Coelurosauria)*.” *J Vertebr Paleontol* 19:497–520.
- Carr TD, Williamson TE, Schwimmer DR, (2005) “*A New Genus And Species Of Tyrannosauroid From The Late Cretaceous (Middle Campanian) Demopolis Formation Of Alabama*” *Journal of Vertebrate Paleontology* 25(1):119–143
- Carrano MT, (2001) “*Implications of limb bone scaling, curvature and eccentricity in mammals and non-avian dinosaurs.*” *J Zool*, 254:41-55.
- Case TJ. (1987) “*Speculations on the growth rate and reproduction of some dinosaurs.*” *Paleobiology*” 3:320–28
- Castanet, J., Francillon-Viellet, H., Meunier, F. J. & de Ricqlès A, (1990) “*Bone and individual aging*” in *Bone* (ed. Hall, B. K.) 245–284
- Castanet, J. (1994) “*Age estimation and longevity in reptiles.*” *Gerontol.* 40, 174–192
- Castanet & Cheylan, (1979) “*Growth marks of bones and scales as an indicator of age in Testudo hermanni and Testudo graeca (Reptilia , Chelonia , Testudinidae)*” *Canadian Journal of Zoology* 57:8
- Castanet J, Newman DG, Girons HS. (1988) “*Skeletochronological data on the growth, age, and population structure of the tuatara, Sphenodon punctatus, on Stephens and Lady Alice Islands, New Zealand.*” *Herpetologica* 44: 25–37.

- Castanet J, Francillon-Vieillot H, Meurnier FJ, de Ricqlès A. (1993) “*Bone and individual aging.*” In *Bone*, Vol. 7: Bone Growth, ed. BK Hall, pp. 245–83. Boca Raton: CRC
- Castanet J, Croci S, Aujard F, Perret M, Cubo J, Margerie E de. (2004) “*Lines of arrested growth in bone and age estimation in a small primate: Microcebus murinus.*” *Journal of Zoology* 263: 31–39.
- Cerda IA, Chinsamy A, Pol D, Apaldetti C, Otero A, Powell JE, *et al.* (2017) “*Novel insight into the origin of the growth dynamics of sauropod dinosaurs*” *PLoS ONE* 12(6): e0179707.
<https://doi.org/10.1371/journal.pone.0179707>
- Chinsamy, A (1990) “*Physiological Implications Of The Bone Histology Of Syntarsus Rhodensis (Saurischia: Theropoda)*” *Palaeont. afr.*, 27, 77-82
- Chinsamy A. (1993) “*Bone histology and growth trajectory of the prosauropod dinosaur Massospondylus carinatus Owen.*” *Modern Geology* 18:319–29
- Christiansen, P. (1998) “*Strength indicator values of theropod long bones, with comments on limb proportions and cursorial potential.*” *Gaia* 15, 241–255.
- Christiansen P, Farina RA (2004) “*Mass prediction in theropod dinosaurs.*” *Hist Biol* 16:85–92.
- Cooper LN, Lee AH, Taper ML, Horner JR. (2008) “*Relative growth rates of predator and prey dinosaurs reflect effects of predation.*” *Proc. R. Soc. B* 275:2609–15
- Coria, R. A.; Currie, P. J. (2006). "A new carcharodontosaurid (Dinosauria, Theropoda) from the Upper Cretaceous of Argentina". *Geodiversitas*. 28 (1): 71–118.
- Coria, R. A.; Salgado, L. (1995). "A new giant carnivorous dinosaur from the Cretaceous of Patagonia". *Nature*. 377 (6546): 224–226.
- Cormack D. (1987) “*Ham’s Histology.*” New York, 732 pp.

Cubo J, Le Roy N, Martinez-Maza C, Montes L. 2012. “*Paleohistological estimation of bone growth rate in extinct archosaurs.*” *Paleobiology* 38:335–49

Cullen TM, Evans DC, Ryan MJ, Currie PJ, Kobayashi Y. (2014) “*Osteohistological variation in growth marks and osteocyte lacunar density in a theropod dinosaur (Coelurosauria: Ornithomimidae).*” *BMC Evolutionary Biology* 14, 231. (doi:10.7934/p1218)

Cullen TM, Simon DJ, Benner EKC, Evans DC. (2020a) “*Morphology and osteohistology of a large-bodied caenagnathid (Theropoda: Oviraptorosauria) from the Hell Creek Formation (Montana): implications for size-based classifications and growth estimation in theropods.*” *Papers in Palaeontology*

Cullen TM, Canale JI, Apesteguía S, Smith ND, Hu D, Makovicky PJ. (2020b) “*Osteohistological analyses reveal diverse strategies of theropod dinosaur body size evolution.*” *Proc. R. Soc. B* 20202258. <http://dx.doi.org/10.1098/rspb.2020.2258>

Currey JD. 1960. “*Differences in the blood-supply of bone of different histological types*” *Quarterly Journal of Microscopical Science* 101: 351–370.

Currey JD. (1987) “*The evolution of the mechanical properties of amniote bone*” *Journal of Biomechanics* 20: 1035–1044.

Currey JD. (2003) “*The many adaptations of bone.*” *Journal of Biomechanics* 36: 1487–1495.

Curry, K.A. (1999) “*Ontogenetic histology of Apatosaurus (Dinosauria: Sauropoda): new insights on growth rates and longevity.*” *J. Vert. Paleontol.* 19, 654–665

de Ricqlès, A. 1974. “*Evolution of endothermy: histological evidence.*” *Evol. Theory* 1:51–80

de Ricqlès A. 1975. “*Recherches paléohistologiques sur les os longs des tétrapodes VII.— sur la classification, la signification fonctionnelle et l’histoire des tissus osseux des tétrapodes (première partie).*” *Annales de Paléontologie (Vertébrés)* 61: 51–129 with nine plates.

- de Ricqlès, A. (1980) “*Tissue structures of dinosaur bone: functional significance and possible relation to dinosaur physiology.*” *A Cold Look at Warm-Blooded Dinosaurs* (Thomas, R.D.K. and Olson, E.C., eds), pp. 103–139, Westview
- Enlow DH. (1969) “*The bone of reptiles*”: pp. 45–80 in A. d. A. Bellairs and T. S. Parsons (eds.), *Biology of the Reptilia*. Academic Press, New York.
- Enlow DH, Brown SO. (1957) “*A comparative histological study of fossil and recent bone tissues, Part 2.*” *Texas Journal of Science* 9: 186–214.
- Erickson, (2005) “*Assessing dinosaur growth patterns: a microscopic revolution*” *TRENDS in Ecology and Evolution*. 20(12)
- Erickson GM, Druckenmiller PS. (2011) “*Longevity and growth rate estimates for a polar dinosaur: a Pachyrhinosaurus (Dinosauria: Neoceratopsia) specimen from the North Slope of Alaska showing a complete developmental record.*” *History of Biology* 24:327–34
- Erickson, G.M. and Tumanova, T.A. (2000) “*Growth curve and life history attributes of Psittacosaurus mongoliensis (Ceratopsia: Psittacosauridae) inferred from long bone histology.*” *Zool. J. Linn. Soc.* 130, 551–566
- Erickson, G.M., Rogers, K.C., Yerby, S.A. (2001) “*Dinosaur growth patterns and rapid avian growth rates.*” *Nature* 412, 429–433
- Erickson, G.M., Makovicky, P.J., Currie, P.J., Norell, M.A., Yerby, S.A., Brochu, C.A. (2004) “*Gigantism and comparative life-history parameters of tyrannosaurid dinosaurs.*” *Nature*. 430, 772–775
- Erickson GM, Currie PJ, Inouye BD, Winn AA. 2006. “*Tyrannosaur life tables: the first look at non-avian dinosaur population biology*” *Science* 313:213–17

- Erickson GM, Curry Rogers K, Varricchio DJ, Norell MA, Xu X. (2007) “*Growth patterns in brooding dinosaurs reveals the timing of sexual maturity in non-avian dinosaurs and genesis of the avian condition.*” *Biology Letters* 3:558–61
- Erickson GM (2014) “*On Dinosaur Growth*” *Annu. Rev. Earth Planet. Sci.* 2014. 42:675–97
- Fowler DW, Woodward HN, Freedman EA, Larson PL, Horner JR. (2011) “*Reanalysis of ‘Raptorex kriegsteini’: a juvenile tyrannosaurid dinosaur from Mongolia.*” *PLoS ONE* 6:e21376
- Francillon-Vieillot, H., de Buffrénil, V., Castanet, J., Géraudie, J., Meunier, F.J., Sire, J.Y., Zylberberg, L. and de Ricqlès, A., (1990) “*Microstructure and mineralization of vertebrate skeletal tissues.*” In *Biom mineralization: Patterns and Evolutionary Trends* (Carter, J.G., ed.), pp. 471–530, Van Nostrand Reinhold
- Henderson, D.M. (1999) “*Estimating the masses and centers of mass of extinct animals by 3-D mathematical slicing*” *Paleobiology* 25, 88–106.
- Horner JR, de Ricqlès A, Padian K. (1999) “*Variation in dinosaur skeletochronology indicators: implications for age assessment and physiology.*” *Paleobiology* 25:295–304
- Horner, J.R., de Ricqlès, A.J., Padian, K. (2000) “*Long bone histology of the hadrosaurid dinosaur Maiasaura peeblesorum: growth dynamics and physiology based on an ontogenetic series of skeletal elements.*” *J. Vert. Paleontol.* 20, 115–129
- Horner JR, Padian K, de Ricqlès A (2001) “*Comparative osteohistology of some embryonic and perinatal archosaurs: developmental and behavioral implications for dinosaurs*” *Paleobiology* 27: 39–58.
- Horner, J.R. and Padian, K. (2004) “*Age and growth dynamics of Tyrannosaurus rex.*” *Proc. R. Soc. London B Biol. Sci.* 271, 1875–1880

- Hubner, T. R. (2012) “*Bone histology in *Dysalotosaurus lettowvorbecki* (Ornithischia: Iguanodontia)—variation, growth, and implications*” PLoS ONE 7:e29958.
- Hurlburt, G. (1999) “*Comparison of body mass estimation techniques using recent reptiles and the pelycosaur *Edaphosaurus Boanerges**” Journal of Vertebrate Paleontology 19, 338–350.
- Huntlocker, A.K., Woodward, H.N., Hall, B.K., (2013) “*Biology of Bone*” In *Bone Histology of Fossil Tetrapods: Advancing Methods, Analysis, and Interpretation*. University of California Press
- Hutton JM, (1986) “*Age Determination of Living Nile Crocodiles from the Cortical Stratification of Bone*” Copeia, 1986(2), pp. 332-341
- Ibrahim, N., Sereno, P. C., Dal Sasso, C., Maganuco, S., Fabri, M., Martill, D. M., Zouhri, S., Myhrvold, N., Lurino, D. A. (2014). "*Semiaquatic adaptations in a giant predatory dinosaur*". Science. 345 (6204): 1613–6.
- Jin X, Varricchio DJ, Poust AW, He T. (2020) “*An oviraptorosaur adult-egg association from the Cretaceous of Jiangxi Province, China*” Journal of Vertebrate Paleontology. e1739060.
- Klein N, Sander PM. (2008) “*Ontogenetic stages in the long bone histology of sauropod dinosaurs.*” Paleobiology 34:247–63
- Köhler M, Marín-Moratalla N, Jordana X, Aanes R. (2012) “*Seasonal bone growth and physiology in endotherms shed light on dinosaur physiology.*” Nature 487:358–61
- Lee AH, O’Connor PM. (2013) “*Bone histology confirms determinate growth and small body size in the noasaurid theropod *Masiakasaurus knopfleri*.*” Journal of Vertebrate Paleontology 33:865–76

Lee, A.H., Huttenlocker, A.K., Padian, K., Woodward, H.N. (2013) “*Analysis of growth rates*” pp. 217–251 in K. Padian and E.-T. Lamm (eds.), *Bone Histology of Fossil Tetrapods: Advancing Methods, Analysis, and Interpretation*. University of California Press, Berkeley, California.

Loewen MA, Irmis RB, Sertich JJW, Currie PJ, Sampson SD (2013) “*Tyrant Dinosaur Evolution Tracks the Rise and Fall of Late Cretaceous Oceans*” PLoS ONE 8(11): e79420.

doi:10.1371/journal.pone.0079420

Lu J, Yi L, Brusatte SL, Yang L, Li H, Chen L, (2014) “*A new clade of Asian Late Cretaceous long-snouted tyrannosaurids*” NATURE COMMUNICATIONS 5:3788 DOI:

10.1038/ncomms4788

Maleev, E., (1955a) “*Gigantic carnivorous dinosaurs of Mongolia*” Dokladi Akademii Nauk S.S.S.R., v. 104, p. 634-637.

Maleev, E., (1955b) “*New carnivorous dinosaurs from the Upper Cretaceous of Mongolia*” Dokladi Akademii Nauk S.S. S.R. ,v. 104,p. 779-782.

Alexander RM, Jayes AS, Maloiy GMO, Wathuta EM, (1979) “*Allometry of the limb bones of mammals from shrews (Sorex) to elephant (Loxodonta)*” J Zool, 189:305-314.

Myhrvold NP (2013) “*Revisiting the Estimation of Dinosaur Growth Rates*” PLoS ONE 8(12): e81917. doi:10.1371/journal.pone.0081917

Nesbitt, SJ, Denton Jr, RK, Loewen, MA, Brusatte, S, Smith, ND, Turner, AH, Kirkland, JI,

McDonald, AT & Wolfe, DG (2019) “*A mid-Cretaceous tyrannosauroid and the origin of North American end-Cretaceous dinosaur assemblages*”, *Nature Ecology & Evolution*.

<https://doi.org/10.1038/s41559-019-0888-0>

- Packard GC, Boardman TJ, Birchard GF. (2009) “*Allometric equations for predicting body mass of dinosaurs.*” *Journal of Zoology* 279:102–10
- Padian, K., de Ricqlès, A.J., Horner, J.R. (2001) “*Dinosaurian growth rates and bird origins.*” *Nature*. 412, 405–412
- Padian K, Horner JR. (2004) “*Dinosaur physiology*”: pp. 660–671 in Weishampel DB, Dodson P, Osmólska H (eds.), *The Dinosauria: 2nd Edition*. University of California Press, Berkeley.
- Padian K, Werning S, Horner JR. (2016) “*A hypothesis of differential secondary bone formation in dinosaurs.*” *C.R. Palevol* 15, 40–48. (doi:10.1016/j.crpv.2015.03.002)
- Padian K, Stein K, (2013) “*Evolution of Growth Rates and Their Implications*” In *Bone Histology of Fossil Tetrapods: Advancing Methods, Analysis, and Interpretation*. University of California Press
- Persons SW, Currie PJ, Erickson GM, (2019) “*An Older and Exceptionally Large Adult Specimen of Tyrannosaurus rex*” *THE ANATOMICAL RECORD* 303:656–672
- Prondvai E, Godefroit P, Adriaens D, Hu D (2018) “*Intraskeletal histovariability, allometric growth patterns, and their functional implications in bird-like dinosaurs*” *Scientific Reports* 8:258 DOI:10.1038/s41598-017-18218-9
- Reid, R.E.H. (1997) “*Dinosauria physiology: the case for ‘intermediate’ dinosaurs.*” *The Complete Dinosaur* (Farlow, J.O. and Brett-Surman, M.K., eds), pp. 449–473, Indiana University Press
- Rozhdestvensky, A. (1965) “*Growth changes in Asian dinosaurs and some problems of their taxonomy*”, *paleontologicheskii Zhurnal*, p. 95-109.
- Rubin CT, Lanyon LE, (1984) “*Dynamic strain similarity in vertebrates: an alternative to allometric limb bone scaling*” *J Theoret Biol*, 107:321-327.

- Sander PM, Klein N, Buffetaut E, Cuny G, Suteethorn V, Le Loeuff J. (2004). “*Adaptive radiation in sauropod dinosaurs: bone histology indicates rapid evolution of giant body size through acceleration.*” *Org. Divers. Evol.* 4:165–73
- Sander PM, Klein N, Stein K, Wings O. (2011) “*Sauropod bone histology and its implications for sauropod biology.*” In *Biology of the Sauropod Dinosaurs: Understanding the Life of Giants*, ed. N Klein, K Remes, CT Gee, PM Sander, pp. 276–302. Bloomington/Indianapolis: Indiana Univ. Press
- Seebacher, F. (2001) “*A new method to calculate allometric length mass relationships of dinosaurs*” *Journal of Vertebrate Paleontology* 21, 51–60.
- Sereno PC, Tan L, Brusatte SL, Kriegstein HJ, Zhao X, Cloward K, (2009) “*Tyrannosaurid Skeletal Design First Evolved at Small Body Size*” *Science* 326:5951 418-422
- Tarlo, L.B., and Mercer, J. R., (1968) Sixteenth Symp. Vert. Palaeont. Comp. Anat. (Reading)
- Tsuihiji T, Watabe M, Tsogtbaatar K, Tsubamoto T, Barsbold R, Suzuki S, Lee AH, Ridgely RC, Kawahara Y, Witmer LW, (2011) “*Cranial osteology of a juvenile specimen of Tarbosaurus bataar from the Nemegt Formation (Upper Cretaceous) of Bugin Tsav, Mongolia*” *J. Vertebr. Paleontol.* 31, 497–517.
- Tucker AD. 1997. “*Validation of skeletochronology to determine age of freshwater crocodiles (Crocodylus johnstoni).*” *Australian Journal of Marine and Freshwater Research* 48: 343–351.
- Varricchio DV. (1993) “*Bone microstructure of the Upper Cretaceous theropod dinosaur Troodon formosus.*” *Journal of Vertebrate Paleontology* 13:99–104
- Werning S. (2012) “*The ontogenetic osteohistology of Tenontosaurus tilletti.*” *PLoS ONE* 7:e33539

Woodward HN, (2005) “*Bone Histology Of The Sauropod Dinosaur Alamosaurus Sanjuanensis From The Javelina Formation, Big Bend National Park, Texas*” Texas Tech University

Woodward HN, Lehman TM. (2009) “*Bone histology and microanatomy of Alamosaurus sanjuanensis (Sauropoda: Titanosauria) from the Maastrichtian of Big Bend National Park, Texas*” J. Vertebr. Paleontol. 29:807–21

Woodward, H.N., Padian, K., Lee A.H., (2013) “*Skeletochronology*” In *Bone Histology of Fossil Tetrapods: Advancing Methods, Analysis, and Interpretation*. University of California Press

Woodward HN, Fowler EAF, Farlow JO, Horner JR, (2015) “*Maiasaura, a model organism for extinct vertebrate population biology: a large sample statistical assessment of growth dynamics and survivorship*” Paleobiology, 41(4), pp. 503–527

Woodward HN, Tremaine K, Williams SA, Zanno LE, Horner JR, Myhrvold N, (2020) “*Growing up Tyrannosaurus rex: Osteohistology refutes the pygmy ‘Nanotyrannus’ and supports ontogenetic niche partitioning in juvenile Tyrannosaurus*” Sci. Adv.; 6 : eaax6250

Xu X, Clark JM, Forster CA, Norell MA, Erickson GM, et al. 2006. “*A primitive tyrannosauroid dinosaur from the Late Jurassic of China with an exaggerated cranial crest*” Nature 439:715–18

Zanno, L.E., Tucker R.E., Canoville A, Avrahami H.M., Gates, T.A., Makovicky, P.J. (2019) “*Diminutive fleet-footed tyrannosauroid narrows the 70-million-year gap in the North American fossil record*” Communications Biology 2:64 <https://doi.org/10.1038/s42003-019-0308-7>

FIGURES

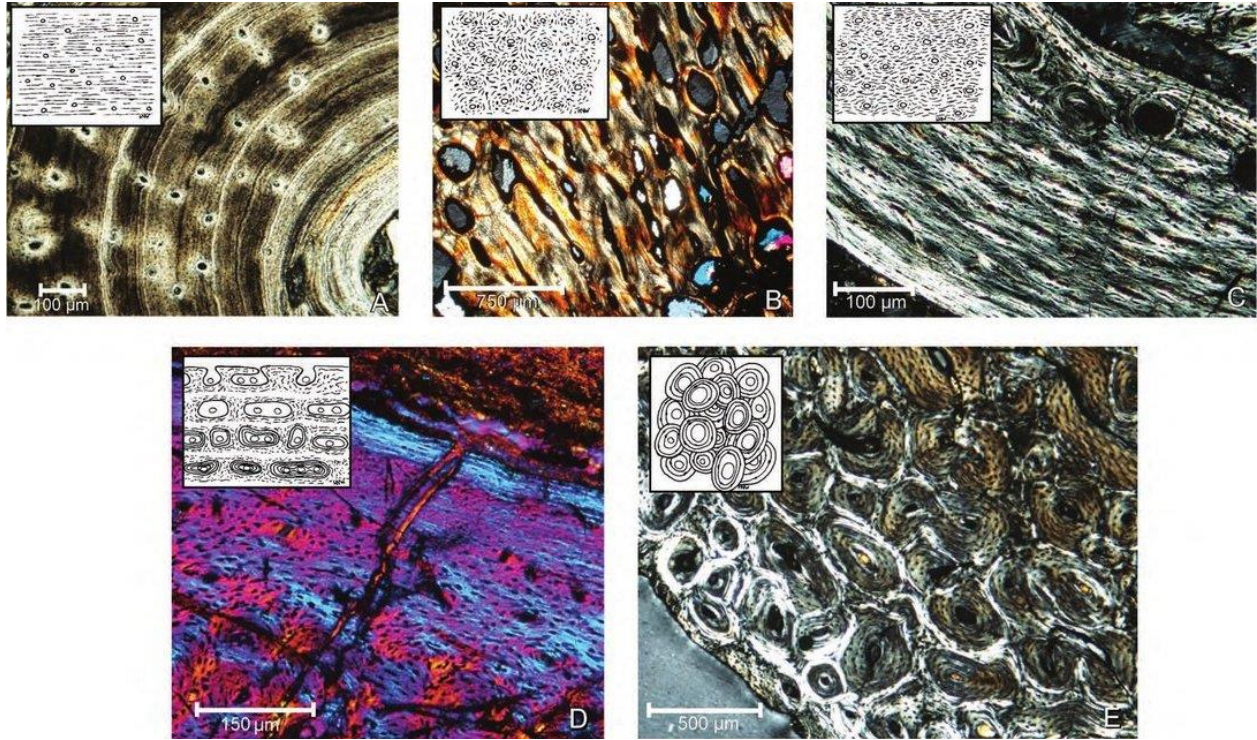


Figure 1.1. Examples of common bone tissue and complexes. Lamellar (A), Woven-fibered (B), Parallel-fibered (C), Fibrolamellar (D), and Dense Haversian Tissue (E). Modified from Huttenlocker *et al.*, (2013).

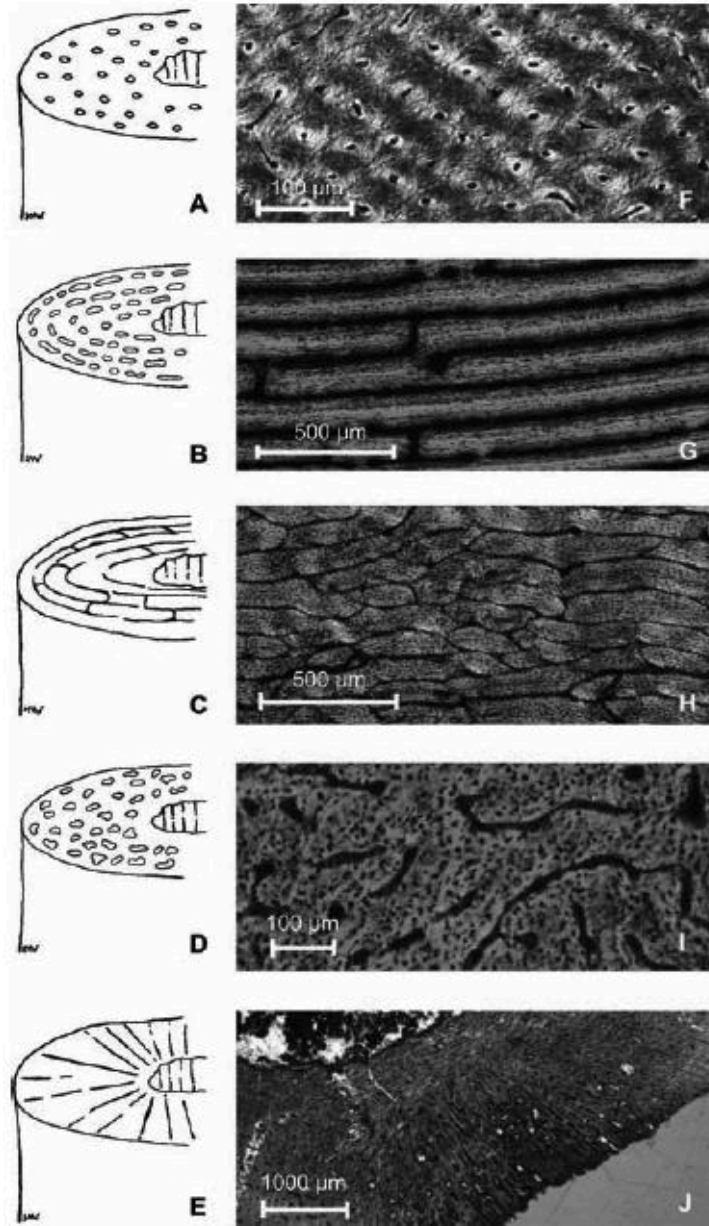


Figure 1.2. Examples of common vascularization types. Longitudinal (a,f), laminar (b,g), plexiform (c,h), reticular (d,i), and radial (e,j). Modified from Huttenlocker *et al.*, (2013).

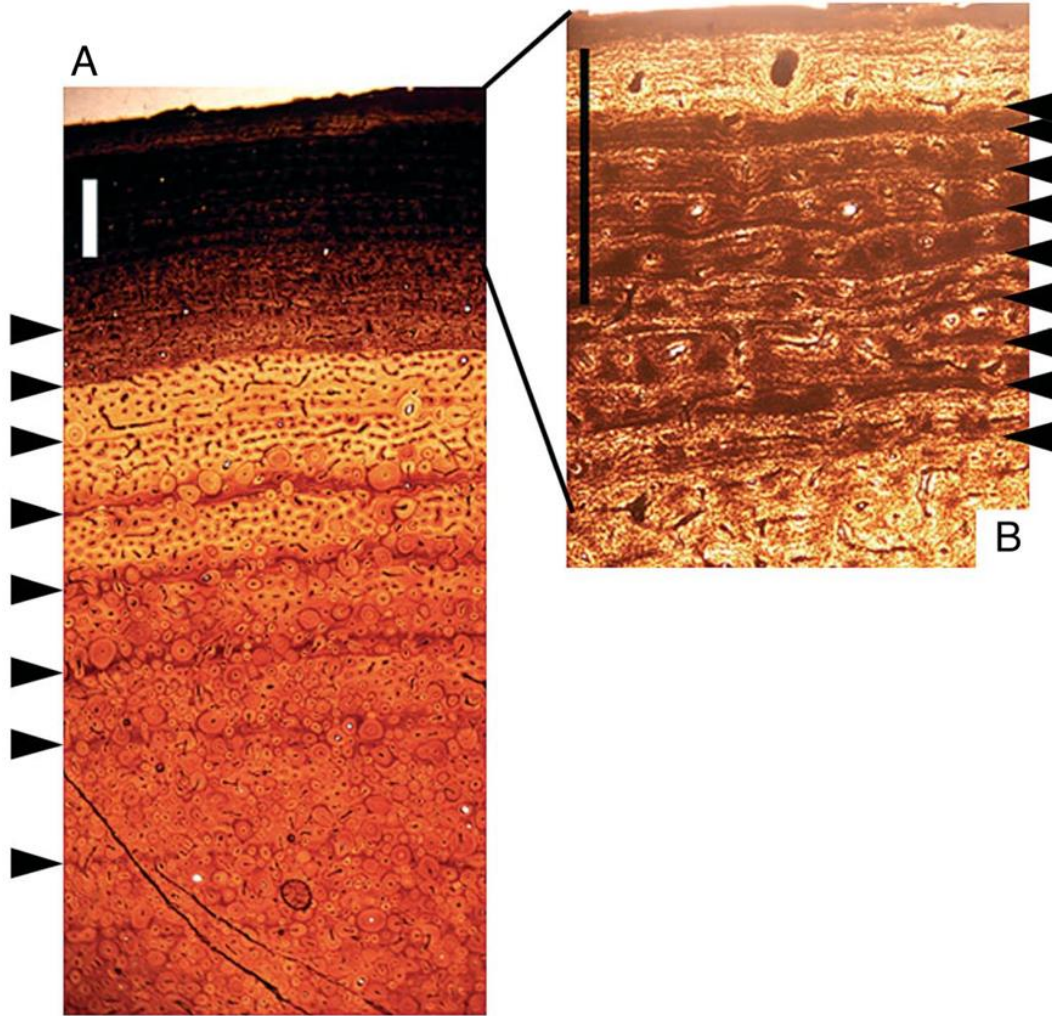


Figure 1.3. Histological section of a skeletally mature *T. rex* fibula. (A) Cortical section with LAGs marked by black arrows. (B) Close up of outer cortex highlighting an EFS. Modified from Horner & Padian (2004).

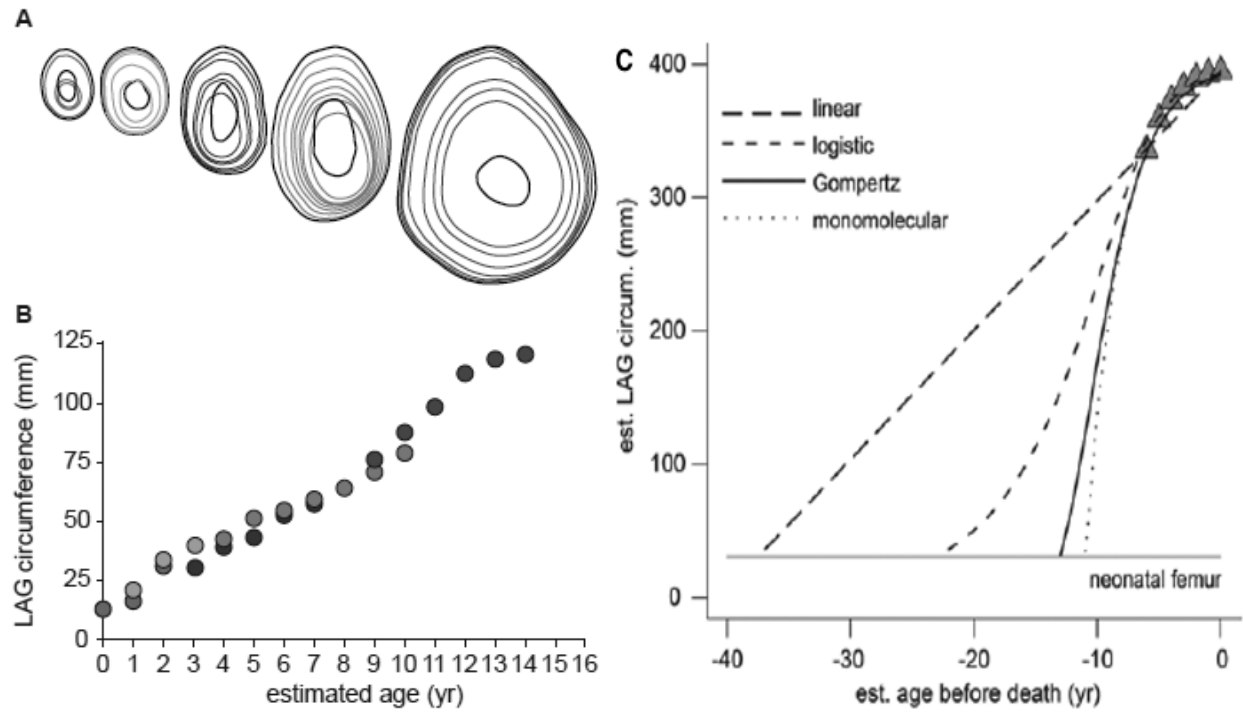


Figure 1.4. Retro-calculation of a specimen's age using the superimposition method (A,B) and the non-linear modeling method (C). Modified from Woodward *et al.*, (2013).

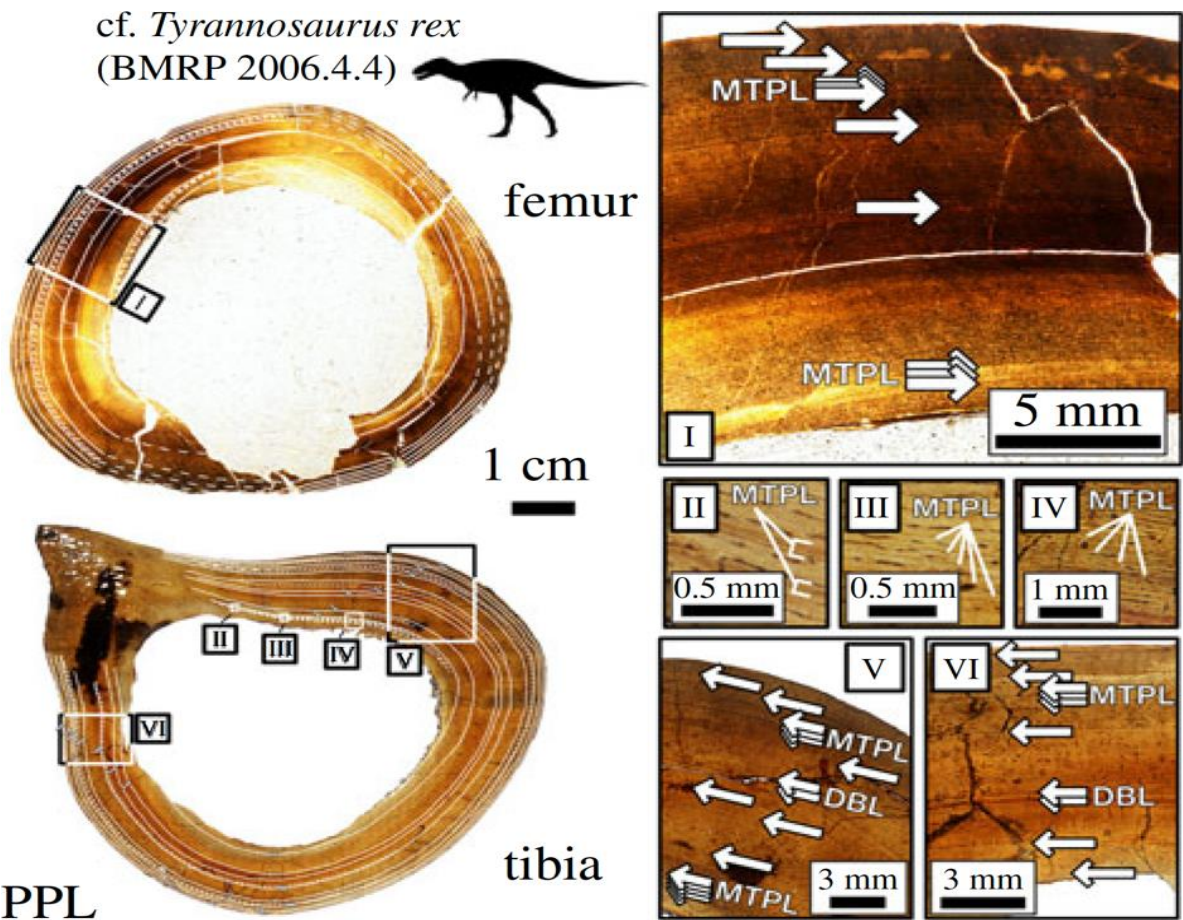


Figure 1.5. Histological section of skeletally immature *T. rex* femur and tibia. Dotted lines in sections refer to an example of a multi-LAG that does not encircle the entire circumference of the cortex and should be considered as a single growth event. Modified from Cullen *et al.*, (2020b).

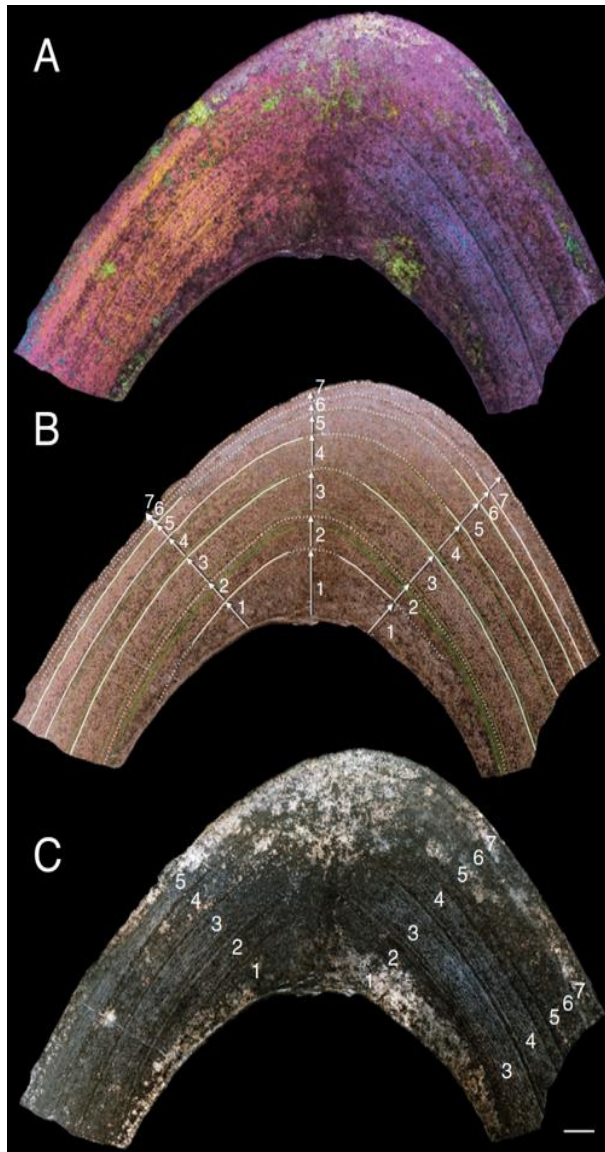


Figure 1.6. Histological section of *Moros intrepidus* femur in polarized light with lambda filter (A), natural light with numbered LAG circumferences (B), and polarized light (C). Modified from Zanno *et al.*, (2019).

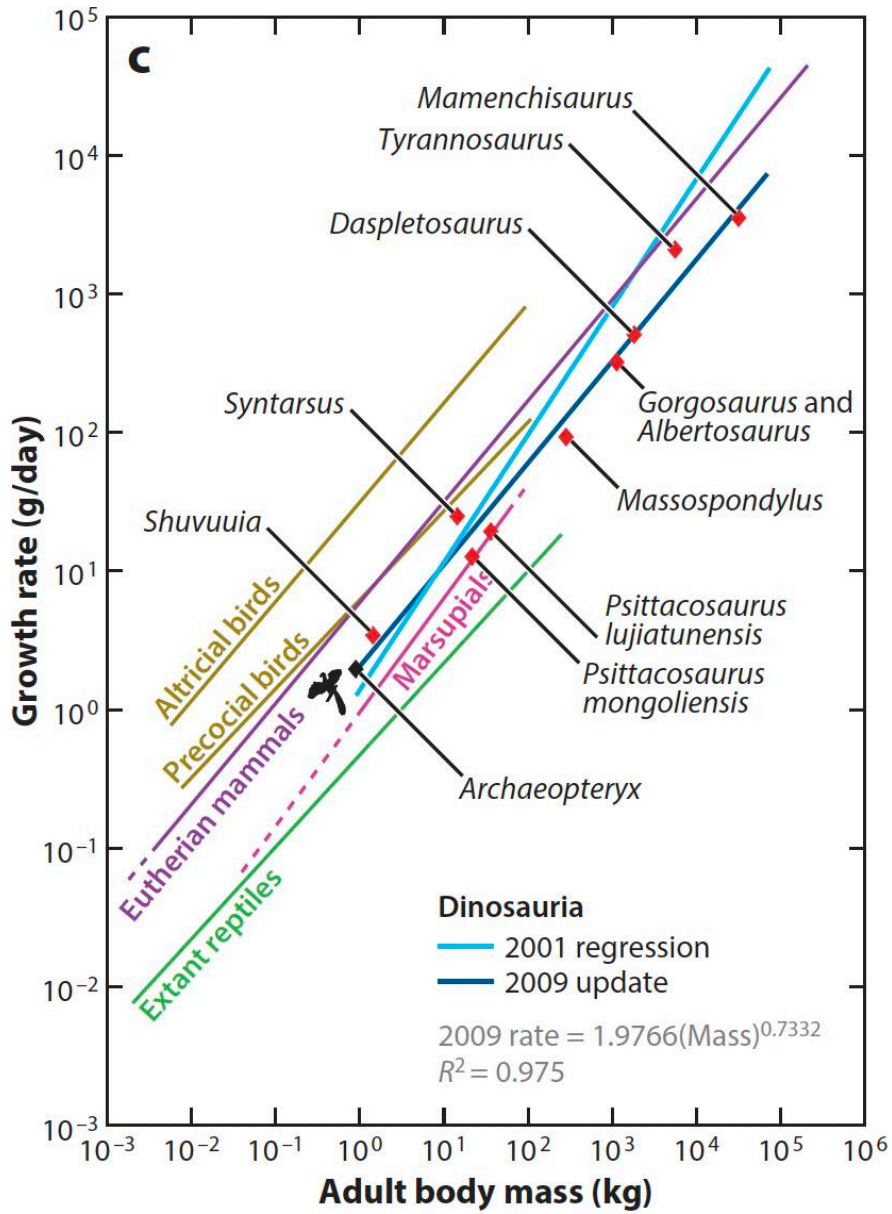


Figure 1.7. Linear regression showing the relationship between growth rate and body mass at skeletal maturity. Dinosaurs on average grow at rates similar to those of warm-blooded animals. Reproduced from Erickson (2014).

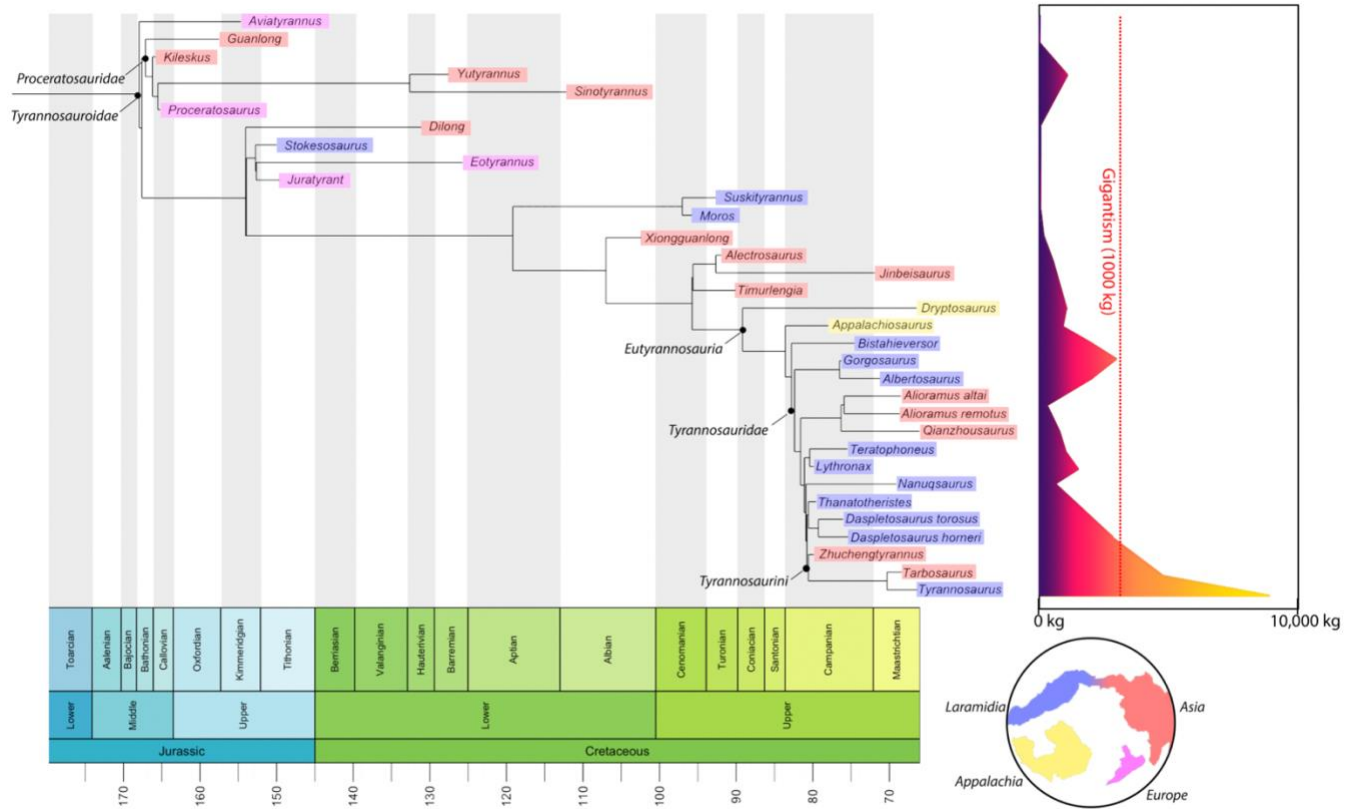


Figure 1.8. Time calibrated phylogeny of *Tyrannosauroidae* with global occurrences and phylogenetic distribution of body sizes.

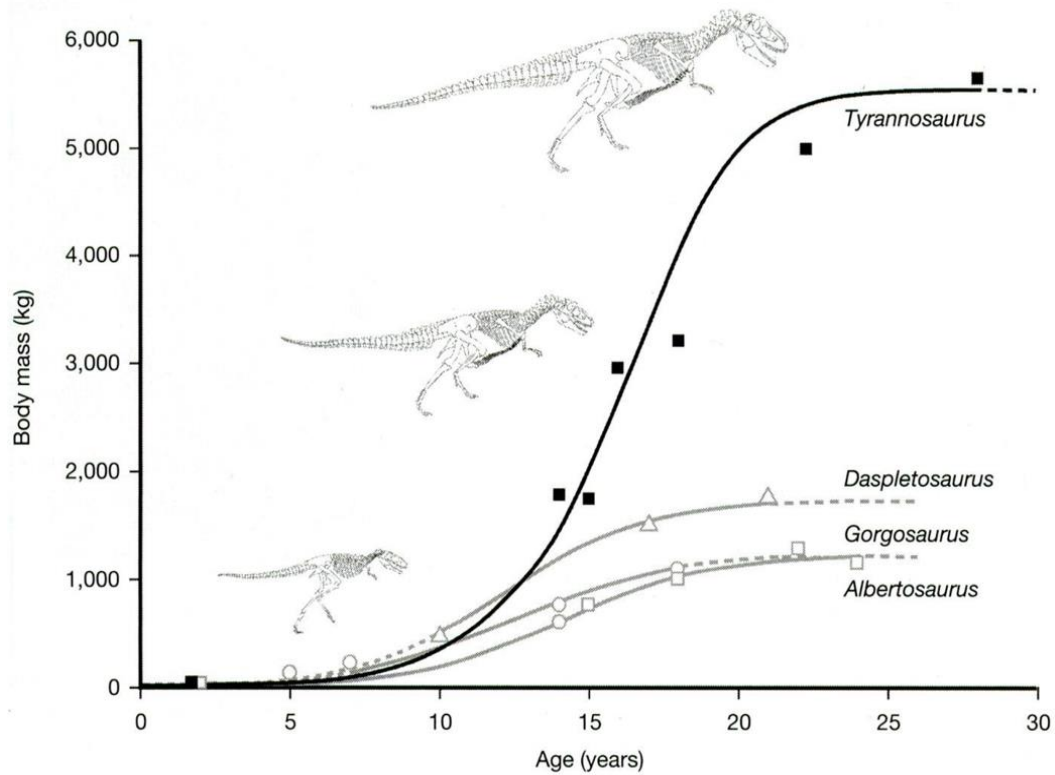


Figure 1.9. Growth curve reconstruction of North American tyrannosaurids. While mass estimates are not accurate, the general form of each species' curve in relation to one another is accurate. Reproduced from Erickson *et al.*, (2004).

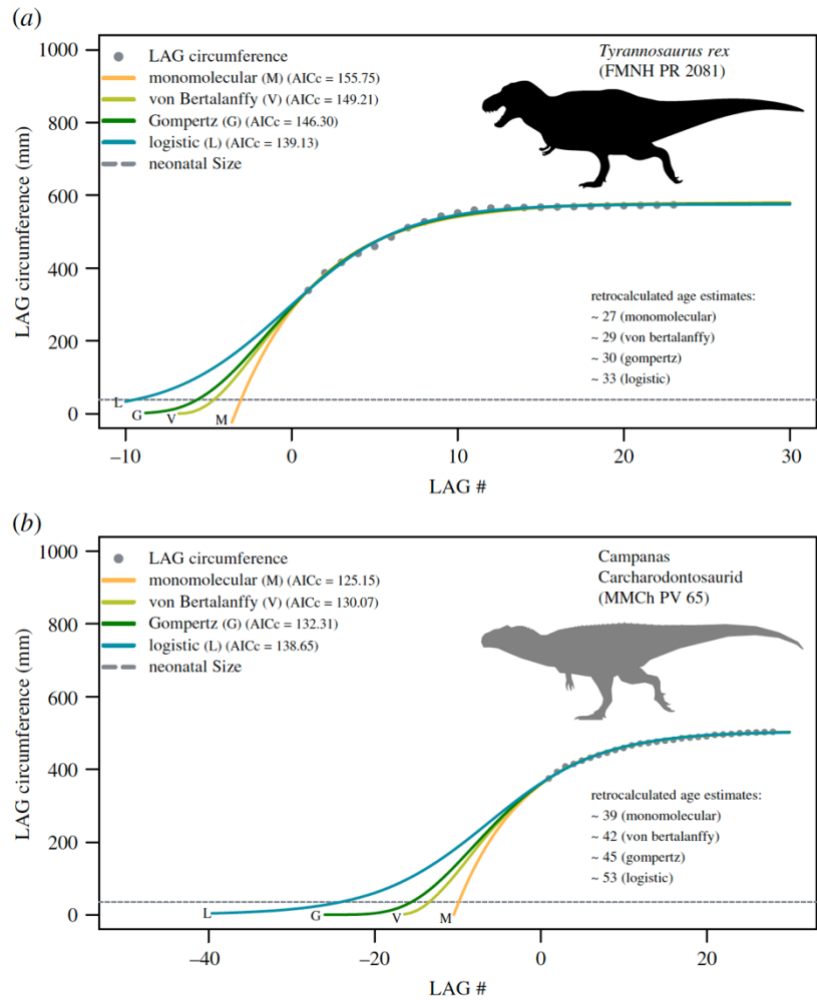


Figure 1.10. Growth curve reconstructions for skeletally mature *T. rex* using peramorphic acceleration (A) and Carcharodontosaurid using hypermorphosis (B). Reproduced from Cullen *et al.*, (2020b).

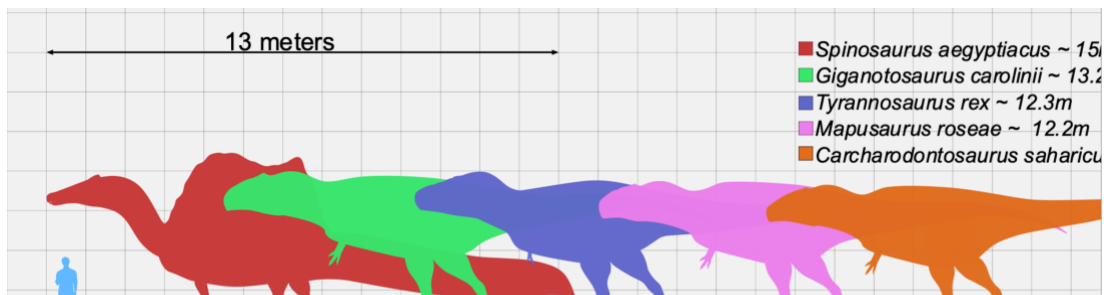


Figure 1.11. Gigantic Theropods. Note that *T. rex* is the only coelurosaur to achieve gigantic proportions. Image provided by Wikimedia User Josh1924

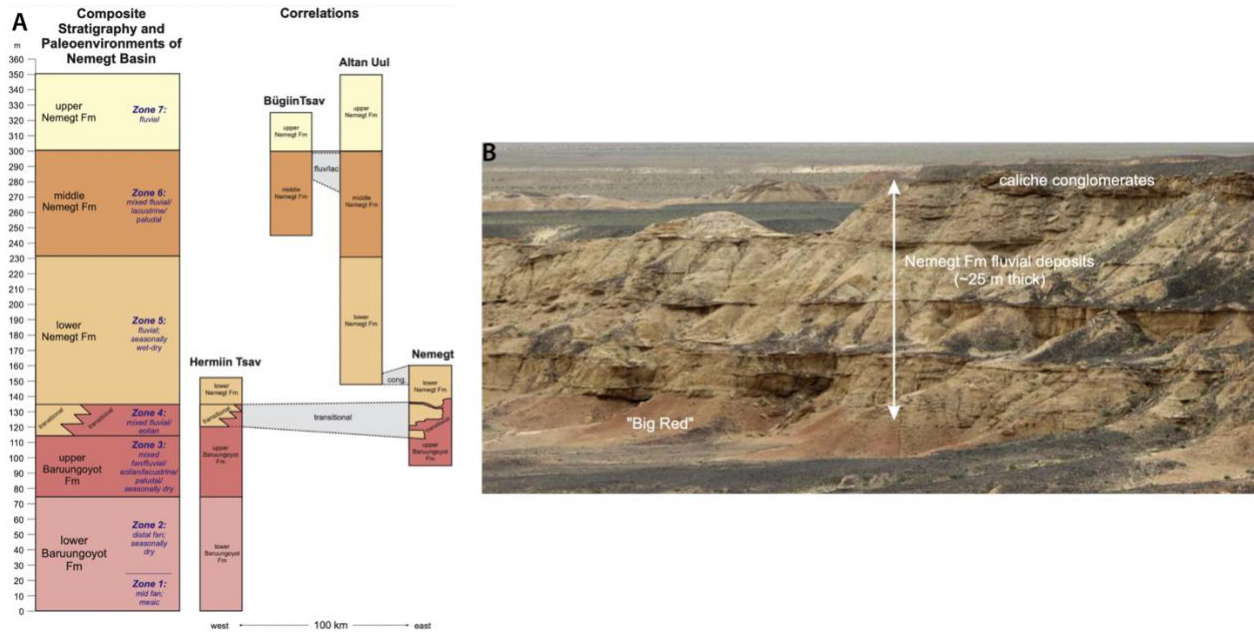


Figure 1.12. Nemegt Stratigraphic column including localities that preserve *T. bataar* fossils (A) and a typical outcrop of the formation in Mongolia (B). Reproduced from Eberth (2018).

CHAPTER 2: Materials and Methods

Specimens

Twelve specimens referred to *Tarbosaurus bataar* were studied. Body size estimates of these individuals varied from a roughly two and a half meter long juvenile individual (MPC-D 107/7) to an over ten-meter long skeletally mature individual (MPC-D 107/2) (Fig, 2.1). The current specimen list provides a robust sample that covers a range of ontogenetic stages and body sizes (Table 2.1). Special permission was granted by the Institute of Paleontology of Mongolian Academy of Sciences (IPMAS) and the Mongolian Heritage to describe, measure, and process the femora, tibiae, and/or fibulae of these specimens. Multiple hind limb elements for each specimen were sampled to account for intraskeletal variation in histological data (Cullen *et al.*, 2020b).

MPC-D 107/2, MPC-D 100/61, and MPC-D 100/70 were molded and cast to produce a replica of the sectioned elements before destructive sampling. IPMAS will keep one set of casts for these specimens and another set will be accessioned at the North Carolina Museum of Natural Sciences (NCMNS).

Histological Methods

Technicians at the IPMAS cut 1-3 cm transverse sections as close as possible to the mid-diaphysis from each long bone used in this study. An additional cut was taken from the fibula of MPC-D 100/64 that was more proximally located to compare the histological differences. These sections were embedded in epoxy resin to keep them stabilized during destructive sampling and then shipped to the NCMNS. The side of these blocks that displayed the inner cortex were

polished using Buehler MetaServ 250 Grinder Polisher starting at 200 grit and incrementally decreasing grit intensity to 1200 grit. Once these blocks had been polished, the polished face was attached to a 3x2 petrographic slide using a clear epoxy resin (EPO-TEK 301). Tibia and femur specimens too big to fit on a 3x2 slide were cut to fit the largest possible section of the cortex. Excess cortical bone was removed from the petrographic slide via 1.5 mm blade saw and other side was polished until the inner cortex was visible under a microscope. Specimens were described using a Nikon Eclipse Ci POL microscope and their specific features were photographed using a Nikon DS-Fi2 camera attachment. Large composite pictures of slides were taken using a Keyence VHX-S550E and VHX-500 Digital Microscope.

Descriptions

Histological terminology used to describe the cortical tissue, vascular morphology, and CGMs follows that of Francillon-Vieillot *et al.* (1990). Growth marks identified by a distinct line that is darker, has the slowest growing tissue, and has no vascularity were considered LAGs. Growth marks identified by a semi-distinct thin line with reduced vascularity and slower growing tissue were considered annuli. All LAGs and annuli were counted and measured regardless of their spacing for descriptions and analyses.

CGM Measurements

CGMs were measured using ImageJ from images produced from Keyence VHX-S550E Digital Microscope. When the entire cortex was preserved, the circumference of each CGM was measured directly. For specimens in which the cortex could not fit on the 3x2 slide, CGM circumferences were calculated using Ramanujan's (1914) formula:

$$(1) C = \pi \left[3(a + b) \sqrt{(a + 3b)(3a + b)} \right]$$

Where C is the circumference, a is the major radii, and b is the minor radii. To ensure these calculated circumferences were accurate estimations, resulting circumference estimates of MPC-D 107/7 and MPC-D 100/66 limb bones were compared to actual circumferences and no significant difference was observed. Spacing between CGMs were also measured to identify patterns of increases or decreases in annual growth.

Mass Estimates

Body mass estimates will be calculated using these measurements and the following equations (*sensu* Campione *et al.*, 2014; Erickson & Tumanova, 2000):

$$(2) \log BM_{\text{adult}} = 2.754 \times \log(C_{\text{femur adult}}) - 0.683$$

$$(3) \text{Percent of Adult Size} = (C^3_{\text{femur developing}} / C^3_{\text{femur adult}}) \times 100$$

$$(4) BM_{\text{developing}} = (C^3_{\text{femur developing}} / C^3_{\text{femur adult}}) * BM_{\text{adult}}$$

where BM is the body mass estimate of the specimen. MPC-D 107/2 will be used as the “adult” reference point (Tsuihiji *et al.*, 2011) and all other specimens will be considered as developing in these equations. These calculations can be made within the MASSTIMATE package in R provided by Campione *et al.* (2014). Measuring the circumference of each LAG will give a body size estimate at the end of each growth interval prior to its death.

Growth Curve Reconstruction

Growth curves will be reconstructed using the methodology of Lee & O'Connor (2013b); for every limb element, the entire growth record from each individual will be fit with the following non-linear parametric curve derived from Cooper *et al.* (2008):

$$(5) C_{t+1} = C_t + G$$

$$(6) C_{t+1} = A \left[1 + \exp(-K) \left[\left(\frac{C_t}{A} \right)^{1-m} - 1 \right] \right]^{\frac{1}{1-m}}$$

$$(7) RGR = K/m$$

where C_t is the LAG circumference at time t , C_{t+1} is the LAG circumference at time $t + 1$, G is the absolute growth rate, A is the asymptotic circumference, K is the mean growth rate, RGR is the growth rate relative to m , and m controls the model type by changing the inflection point of the shape parameter. The models used in this study are monomolecular ($m=0$), von Bertalanffy ($m=2/3$), Gompertz ($m=1.001$), Logistic ($m=2$), extreme value function ($m=4$), innominate Richards model ($m=8.4$), and a linear model ($m=N/A$) (Fig. 2.2). Each individual will be fit with these models and then an average model will be created from these. AIC values will be calculated for each model average and the model with the lowest AIC will be chosen as the optimal model. This optimal model will be used to estimate ages and neonatal sizes (A_0) for each individual within the model. R scripts for this methodology can be found in Lee & O'Connor (2013). These model reconstructions will be done with original limb bone circumference data as well as estimated body masses based on each limb bone to produce a total

of six models. MPC-D 100/63 was excluded from the growth curve reconstructions since less than three CGMs were found (the minimum number required to complete the analysis).

Because counting CGM couplets and annuli in addition to LAGs will change available growth data and thereby affects age estimates, I subsampled the entire growth record across all individuals and limb elements twice to account for these discrepancies. The first subsample averaged the circumference of the two CGMs defining the couplet to treat this as a single growth event. The second subsample only measured complete cessations of growth and therefore all annuli were removed and growth zones that were captured within LAGs were retained. These subsampled data were run through the same models as before using the R scripts provided. Standard residual error was calculated for original and subsampled models to determine which model was better fit to the data.

Institutional Abbreviations

Burpee Museum of Natural History, Rockford, Illinois, U.S.A. (**BMRP**); Field Museum of Natural History, Chicago, Illinois, U.S.A. (**FMNH**); Institute of Paleontology of Mongolian Academy of Sciences, Ulaanbaatar, Mongolia (**IPMAS**); Long Hao Institute of Geology and Paleontology, Hohhot, Nei Mongol, China (**LH PV18**); Mongolian Paleontological Center, Ulaanbaatar, Mongolia (**MPC**); North Carolina Museum of Natural Sciences, Raleigh, North Carolina, U.S.A. (**NCMNS**); Paleontological Institute, Russian Academy of Sciences, Moscow, Russia (**PIN**).

Other Abbreviations

Cyclical Growth Mark (**CGM**); Lines of Arrested Development (**LAG**); Relative Growth Rate (**RGR**)

REFERENCES

- Campione N.E., Evans, D.C., Brown, C.M., Carrano, M.T. (2014) “*Body mass estimation in non-avian bipeds using a theoretical conversion to quadruped stylopodial proportions*” *Methods in Ecology and Evolution*, 5, 913–923
- Cooper LN, Lee AH, Taper ML, Horner JR. (2008) “*Relative growth rates of predator and prey dinosaurs reflect effects of predation.*” *Proc. R. Soc. B* 275:2609–15
- Cullen TM, Canale JI, Apesteguía S, Smith ND, Hu D, Makovicky PJ. (2020b) “*Osteohistological analyses reveal diverse strategies of theropod dinosaur body size evolution.*” *Proc. R. Soc. B* 20202258. <http://dx.doi.org/10.1098/rspb.2020.2258>
- Erickson, G.M. and Tumanova, T.A. (2000) “*Growth curve and life history attributes of Psittacosaurus mongoliensis (Ceratopsia: Psittacosauridae) inferred from long bone histology.*” *Zool. J. Linn. Soc.* 130, 551–566
- Francillon-Vieillot, H., de Buffrénil, V., Castanet, J., Géraudie, J., Meunier, F.J., Sire, J.Y., Zylberberg, L. and de Ricqlès, A., (1990) “*Microstructure and mineralization of vertebrate skeletal tissues.*” In *Biom mineralization: Patterns and Evolutionary Trends* (Carter, J.G., ed.), pp. 471–530, Van Nostrand Reinhold
- Lee AH, O’Connor PM. (2013) “*Bone histology confirms determinate growth and small body size in the noasaurid theropod Masiakasaurus knopfleri.*” *Journal of Vertebrate Paleontology* 33:865–76
- Ramanujan, S. (1914) “*Modular equations and approximations to pi. Q. J.*” *Math.* 45, 350–372

Tsuihiji T, Watabe M, Tsogtbaatar K, Tsubamoto T, Barsbold R, Suzuki S, Lee AH, Ridgely RC, Kawahara Y, Witmer LW, (2011) “*Cranial osteology of a juvenile specimen of Tarbosaurus bataar from the Nemegt Formation (Upper Cretaceous) of Bugin Tsav, Mongolia*” *J. Vertebr. Paleontol.* 31, 497–517.

FIGURES

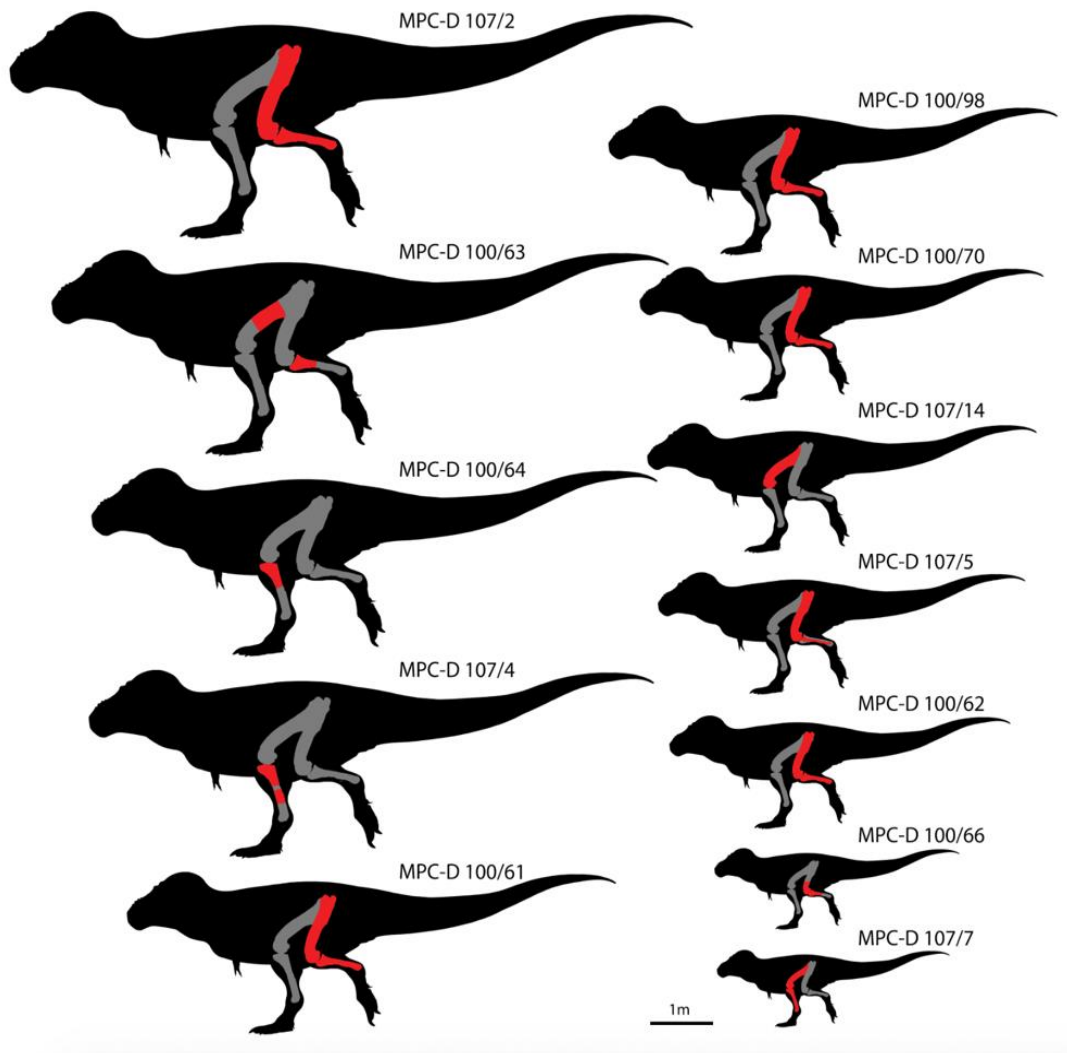


Figure 2.1. *Tarbosaurus bataar* individuals used in this study. Bones highlighted in red were histologically sampled.

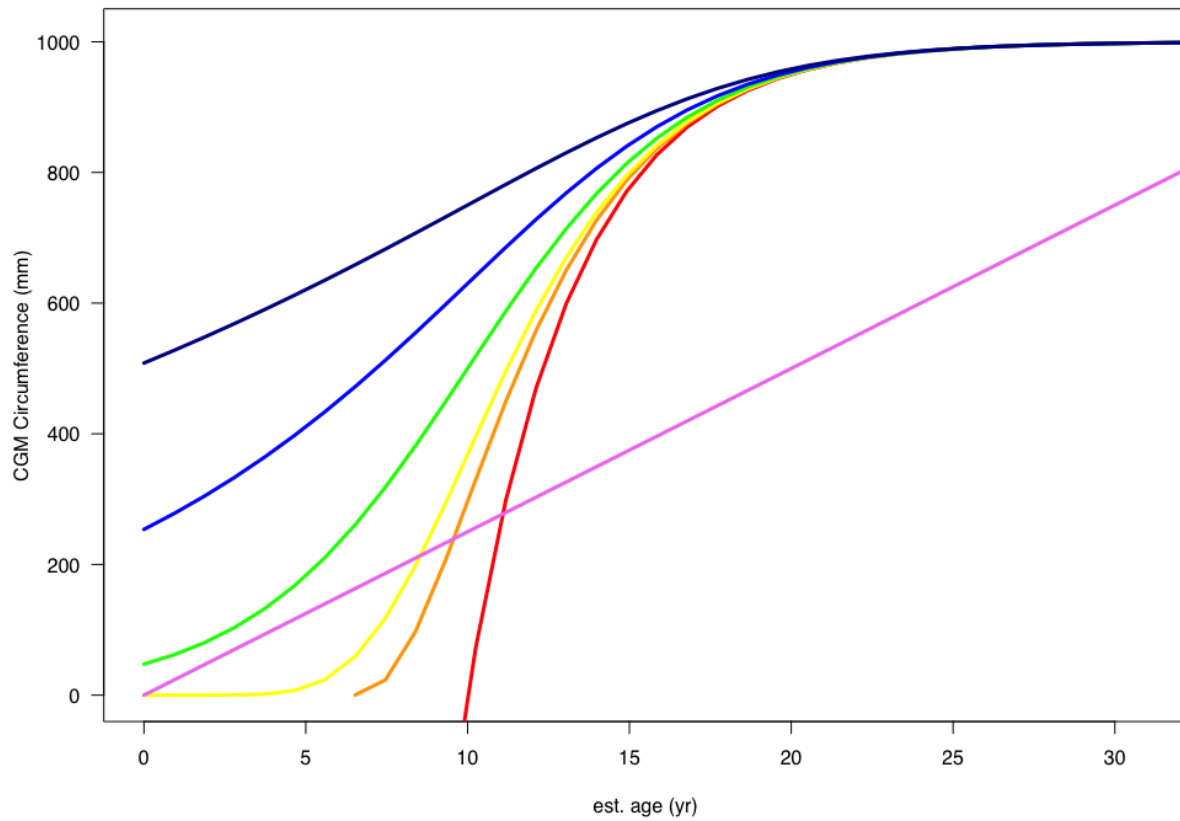


Figure 2.2. Graphical representation of different model shapes. Non-linear curves hold asymptotic size, growth rate, and inflection point constant, but change m value. Red is monomolecular, orange is von bertalanffy, yellow is gompertz, green is, blue is EVF, dark blue is Richards, and violet is linear.

TABLES

Table 2.1. General Specimen Information

Specimen	Femur Length	Femur Circumference	Tibia Length	Tibia Circumference	Fibula Length	Fibula Circumference	Locality	Year Collected
MPC-D 107/7	307.5	92.788	337	84.519		23.266	Bugin Tsav	2006
MPC-D 100/66	425.595	132.048		128.038		61.523	Altan Uul	1970
MPC-D 107/5	650	213.566				61.745	Nemegt	2000
MPC-D 100/62	620	208.89	650	217.697		72.96	Bugin Tsav	1966
MPC-D 107/14	746	205.585					Hermin Tsav	1997
MPC-D 100/70	760	267.548	740	214.839		124.692	Bugin Tsav	
MPC-D 100/98	794	230.259	742	180.97	671	80.66	Bugin Tsav	
MPC-D 100/61	852.5	284.356	710	255.765		106.766	Bugin Tsav	1964
MPC-D 107/4				350.268			Bugin Tsav	
MPC-D 100/64	1000		940	411.037		151.431	Nemegt	1964
MPC-D 100/63	1020	420.871	980	382.201			Nemegt	1965
MPC-D 107/2	1075	465.829	1000	410.263	855	155.777	Bugin Tsav	1984

Chapter 3: Results

Histological Descriptions

MPC-D 107/7

Similar to what Tsuchiji *et al.* (2011) reported, MPC-D 107/7 displays woven bone tissue across all elements that contain thick, rounded osteocyte lacunae (Fig. 3.1; 3.2; 3.3). Vascularity is high among all elements with vascular morphology being more similar between the femur and tibia than in the fibula. The femur invariably displays fibrolamellar tissue with plexiform vascularity (Fig. 3.1). There are very few secondary osteons present that are restricted to a vertical section near a muscle attachment site. The tibia displays the same fibrolamellar tissue and vascular morphology as the femur (Fig. 3.2). This element also exhibits even less secondary remodeling from secondary osteons than the femur. The fibula preserves longitudinal vascularity that is high in density near the endosteal cortex and decreases in density and size towards the periosteal surface (Fig. 3.3). Secondary remodeling is very apparent as the lateral portion of the cortex is replaced with a Dense Haversian system.

The femoral cortex displays five CGMs in the following order from the periosteal surface to the endosteal surface: An annulus that transitions between a LAG, a double-LAG, a double-annuli, an annulus, and a LAG (Fig. 3.4; Table 3.1). The tibia displays a nearly identical growth record with the only exception being that the outermost annulus/LAG fades out for part of the circumference (Table 3.2). Additionally, the innermost annuli are more prominent in the tibia than in the femur likely the result of intraskeletal growth variability. The fibula displays a similar growth record as well, however, the annuli do not encircle the entire bone (Table 3.3). Taken separately, these elements would suggest variable age estimates based on the partiality of certain

CGMs, with the femur suggesting an older estimate and the fibula suggesting a younger estimate. When examined with respect to each other, it is clear that there are five distinct growth periods. These CGM counts are higher than what was originally reported by Tsuchiji *et al.*, (2011) by about two years. Even though MPC-D 107/7 is older, the observed microstructure morphology still suggests a rapidly growing individual but with a more prolonged rapid growing phase.

MPC-D 100/66

MPC-D 100/66 displays fibrolamellar bone tissue throughout the entirety of each element (Fig. 3.5; 3.6; 3.7). Both the femur and the tibia display plexiform vascularity while the fibula displays primarily longitudinal with small amounts of reticular vascularity (Fig. 3.5; 3.6). All elements exhibit high vascularity throughout and highly disorganized woven tissue near the medullary cavity as a result of these specimens being sampled farther from the diaphysis (Enlow, 1963); samples closer to the proximal or distal ends of long bones have been shown to preserve more rapid growing tissue (Enlow, 1963). Because of this, secondary remodeling is very apparent throughout all elements; Secondary osteons are constrained to mostly the endosteal half of the cortex in the femur and the fibular crest within the tibia. The fibula displays prominent remodeling in which roughly half the cortex is covered in Dense Haversian Tissue (Fig. 3.7).

The femoral cortex displays five CGMs in the following order from the periosteal surface to the endosteal surface: One LAG, two annuli, and one LAG (Fig. 3.8; Table 3.1). The tibia on the other hand preserves five very faint annuli, three of which are only visible under cross-polarized light (Fig. 3.8; Table 3.2). The fibula preserves five CGMs as well, however the outermost CGM is an annulus, followed by two LAGs and two annuli (Fig. 3.8; Table 3.3).

MPC-D 100/62

MPC-D 100/62 displays fibrolamellar tissue, high vascularity, and large round osteocyte lacunae within all elements that suggests rapid growth (Fig. 3.9; 3.10; 3.11). Similarly, to previous skeletally immature specimens, the femora and tibiae display plexiform vascularity while the fibula displays longitudinal and reticular vascularity (Fig. 3.9; 3.10; 3.11). Remodeling is very minor among the femur and tibia; secondary osteons are sparsely present in both elements and are contained within the endosteal third of the cortex (Fig. 3.9; 3.10).

The femur preserves nine LAGs; however, the tibia preserves 12 CGMs and the fibula preserves six, both with a mix of annuli and LAGs (Fig. 3.12; Table 3.1; 3.2; 3.3). CGMs two and three on the femur and tibia and CGMs eight and nine of the tibia are very tightly spaced. These couplets do not fit the progressive increase in zonal spacing towards to periosteum.

A thin band of highly disorganized woven tissue dense with osteocyte lacunae lies within the inner most millimeter of the femoral endosteal cortex (Fig. 3.9). Additionally, between CGMs six and seven, there is a layer of highly disorganized woven bone dense with large osteocyte lacunae (Fig. 3.12).

MPC-D 107/5

The periosteal surface of MPC-D 107/5 is highly weathered across both specimens; this weathering has partially destroyed two of the outermost CGMs in the fibula but does not appear to destroy any CGMs in the femur. The cortex displays fibrolamellar tissue, high vascularity,

and large round osteocyte lacunae within all elements that suggests rapid growth (Fig. 3.13; 3.14). Both the femur and the fibula display predominately longitudinal vascularity (Fig. 3.13; 3.14). Secondary remodeling is extensive in the fibula, with most of the cortex being covered in Dense Haversian tissue except for the medial side (Fig. 3.14). In contrast, the femur preserves very little remodeling and only contains a single well contained vertical section of secondary osteons that is associated with a muscle attachment zone (Fig. 3.13).

The femur preserves 10 LAGs while the fibula preserves seven CGMs varying between LAGs and annuli (Fig. 3.15; Table 3.1; 3.3). Two couplets were identified within the femur at LAGs two and three as well as LAGs four and five. However, The LAGs beneath these do combine within the cortex and constitute LAG six and seven to be double-LAGs.

MPC-D 107/14

MPC-D 107/14 displays fibrolamellar tissue, high amounts of plexiform vascularity, and large round osteocyte lacunae throughout most of the cortex (Fig. 3.16). Towards the major axis, there appears to be a shift from plexiform to longitudinal and then back to plexiform that indicates differing growth dynamics. Additionally, thinner osteocyte lacunae are observed near the periosteal surface and the innermost cortex has small amounts of Haversian tissue, with secondary osteons being scattered through roughly the inner third of the cortex. These factors suggest that this individual, while still considered to be rapidly growing, has slower growth than other individuals of similar size.

The femoral cortex displays five CGMs in the following order from the periosteal surface to the endosteal surface: three LAGs, one double-LAG, one LAG, and an annulus (Fig. 3.17; Table 3.1).

MPC-D 100/70

MPC-D 100/70 predominately preserves fibrolamellar tissue, high vascularity, and large rounded osteocyte lacunae suggesting a rapidly growing individual (Fig. 3.18; 3.19; 3.20). Near the lateral margin of the fibula, the tissue is predominately coarse compact cancellous bone, which suggests even more rapid growth (3.20). However, this is likely due to this sample being taken closer to the distal end of the femur and thus distorting the growth qualities. The femur and tibia preserve mostly plexiform vascularity with small amounts of longitudinal vascularity, while the fibula preserves predominately longitudinal vascularity with minor reticular vascularity (Fig. 3.18; 3.19; 3.20). Secondary osteons are scattered throughout the femur and tibia, but no Dense Haversian Tissue is preserved suggesting that very little remodeling has taken place. The fibula preserves Dense Haversian Tissue on the lateral half of the cortex and a small medullary cavity, leaving roughly half of the cortex remodeled (Fig. 3.20).

The femur preserves nine CGMs, the tibia preserves eleven, and the fibula preserves eight, all varying between LAGs and annuli (Fig. 3.21; Table 3.1; 3.2; 3.3). Within the femur, LAGs two through four are all tightly spaced yet do not combine and are therefore considered a triplet (Table 3.1).

The femur preserves a pathology within the medullary cavity that measures roughly 10 mm wide and 3 mm long (Fig. 22). The abnormal bone preserves highly disorganized woven bone tissue with a high density of large round osteocyte lacunae. The orientation of the tissue is not organized in a circumferential direction like the cortex tissue but is instead highly disorganized in structure. This evidence suggests that this abnormal portion of bone did not break off from the main cortex but is in fact a separate structure. Additionally, this pathology contains a single annulus in the middle and the perimeter of the bone is surrounded by endosteal lamellar bone; both features suggest that this feature was a chronic pathology lasting under two years.

MPC-D 100/98

MPC-D 100/98 preserves fibrolamellar tissue, high vascularity, and large round osteocyte lacunae suggesting that this individual was rapidly growing (Fig. 3.23; 3.24; 3.25). Both the femur and the tibia preserve predominately plexiform vascularity; however, the femur preserves regional changes to longitudinal and occasional radial vascularity (Fig. 3.23; 3.24). The medial region of the femur preserves more disorganized woven tissue near the medullary cavity, suggesting growth may not have been uniform in some regions of the bone. The fibula preserves equal parts longitudinal and reticular vascularity (Fig. 3.25). Secondary osteons are scattered throughout the inner cortex of the tibia and femur, yet the fibula displays prominent remodeling with Dense Haversian tissue obscuring the lateral half of the cortex. The medullary cavity of the tibia is loosely consolidated, and fibers of bone appear to be peeling off from the cortex. Due to a lack of secondary growth around these loose fibers, I determined that this bone destruction is caused by taphonomic erosion rather than pathology.

The femur preserves 14 CGMs, the tibia preserves 15 CGMs, and the fibula preserves 16 CGMs (Fig. 3.26; Table 3.1; 3.2; 3.3). More annuli are found within the fibula while more LAGs are found within the femur. CGMs eight and nine within the femur along with CGMs four and five as well as nine and ten within the tibia can be identified as couplets (Table 3.1; 3.2).

MPC-D 100/61

MPC-D 100/61 predominately preserves fibrolamellar tissue with highly organized, high vascularity, and large round osteocyte lacunae across the femur and tibia (Fig. 3.27; 3.28). In addition to plexiform vascularity, the femur preserves minor radial vascularity. The femur appears to preserve a higher density of osteocyte lacunae near the periosteal surface (Fig. 3.27). This coincides with a minor transition towards less vascularity. The tibia preserves mostly plexiform vascularity; however, vascularity decreases near the periosteal surface as well and leads to regional laminar vascularity (Fig. 3.28). The outermost two millimeters of cortex appears to transition from woven tissue to parallel-fibered tissue and osteocyte lacunae thickness begins to reduce. These factors suggest that growth may have slowed down within the last couple of years for this individual. The fibula preserves longitudinal and reticular vascularity. The cortex is almost entirely covered in dense haversian tissue, leaving only the medial region intact (Fig. 3.29).

The femur preserves nine CGMs, the tibia preserves 11 CGMs, and the fibula preserves eight CGMs (Fig. 3.30; Table 3.1; 3.2; 3.3). The tibia and femur preserve two couplets, while the fibula preserves one couplet (Table 3.1; 3.2). Between the inner most couplet of the tibia, the

zonal tissue drastically transitions to highly disorganized woven bone that ends before the next zone (Fig. 3.28). This may suggest a short growth spurt contained during this year.

MPC-D 107/4

The tibia of MPC-D 107/4 preserves fibrolamellar tissue, high amounts of plexiform vascularity, and large round osteocyte lacunae suggesting that this individual was rapidly growing (Fig. 3.31). The periosteal surface preserves a thin band of densely packed and rounded osteocyte lacunae. Only four CGMs are preserved within the cortex, all of which are LAGs. CGMs two and three are tightly packed together and are a couplet (Fig. 3.32; Table 3.2).

MPC-D 100/64

The tibia of MPC-D 100/64 preserves predominately fibrolamellar tissue, high amounts of plexiform vascularity, and large round osteocyte lacunae (Fig. 3.33). However, the outer two to three millimeters of the cortex transitions to parallel-fibered tissue, less vascularity, laminar and longitudinal vascular morphology, and thinner osteocyte lacunae which suggests a shift towards slower growth. The outer half millimeter of the cortex loses all vascularity and osteocyte lacunae become much thinner, which is consistent with the morphology of an EFS. The diaphysis sample of the fibula is almost entirely covered in dense haversian tissue, leaving only a few millimeters preserved at the medial periosteal cortex (Fig. 3.34). This small amount of the cortex displays woven bone tissue, thick round osteocyte lacunae, and small amounts of longitudinal vascularity (Fig. 3.34). Unlike the tibia, there appears to be no sign of an EFS at the periosteal surface. However, due to the prevalence of dense haversian tissue and reduction of vascularity, this suggests that this sample is near skeletal maturity. When the proximal sample of the fibula is

examined, the cortex preserves woven tissue, high amounts of longitudinal and reticular vascularity, and thick rounded osteocyte lacunae, with dense haversian tissue only obscuring roughly half of the cortex (Fig. 3.35). No EFS or drastic changes in vascularity or tissue type are observed that would indicate skeletal maturity.

MPC-D 100/63

The femur MPC-D 100/63 preserves fibrolamellar bone tissue, high plexiform vascularity, and predominately large round osteocyte lacunae (Fig. 3.37). Osteocyte lacunae become thinner within the outermost millimeter of the cortex. The tibia preserves fibrolamellar tissue with laminar and longitudinal vascularity and osteocyte lacunae that also large and round (Fig. 3.38). Regional patches of highly disorganized woven bone with dense amounts of rounded osteocyte lacunae appear throughout the cortex of both bones and obscure the tissue (Fig. 3.39).

Additionally, roughly the inner half of each cortex is obscured by Dense Haversian Tissue that seem to follow microfractures patterns and growth lines rather than emanating from the endosteum (Fig. 3.39). Secondary remodeling patterns in the middle of the cortex is common in stress fractures (Rothschild & Martin 1993; Rothschild 1988). Stress fractures, or fatigue fractures to be more specific, occur as a result of continuous loading on bones; these stress loadings are under the force requirements needed to completely break a bone but lead to gradual mechanical failure within the bone (Rothschild & Martin 1993; Rothschild 1988). Another form of stress fractures, known as insufficiency fracture, are the caused by a lack of bone remodeling due to osteoporosis and are common in older individuals (Daffner & Pavlov, 1992). Even though MPC-D 100/63 is a larger individual, and most likely older, the fractures observed here align more with fatigue fractures since these fractures appear to be remodeled and healed, thereby

refuting the presence of osteoporosis. Fatigue fractures are common among non-weight bearing tyrannosaur elements (e.g., ribs, furcula, manual elements, and fibula) and especially in *Tarbosaurus* manual elements due to prey restraint (Rothschild *et al.*, 2001; Rothschild & Tanke, 2005; Lipkin & Carpenter, 2008; Bell, 2010). However, an example has yet to have been observed within any weight-bearing limb bone element until now.

Because of the fragmentary nature of the bone, anisotropic qualities of the tissue, and prevalence of secondary remodeling, no CGMs could be identified in either section.

MPC-D 107/2

The femur of MPC-D 107/2 preserves predominately fibrolamellar tissue, high amounts of plexiform vascularity, and large round osteocyte lacunae (Fig. 3.40). The outermost two millimeters of the cortex exhibit a drastic transition to parallel-fibered tissue, less vascularity that changes to more longitudinal and laminar morphology, and osteocyte lacunae that become thinner. Additionally, the femur preserves an EFS at the periosteal surface which indicates that this bone achieved skeletal maturity (Fig. 3.40). Surprisingly, no Dense Haversian Tissue is found within the femur and secondary osteons are scattered through only the inner third of the cortex. The tibia also preserves predominately fibrolamellar tissue, high amounts of plexiform vascularity, and large round osteocyte lacunae (Fig. 3.41). This bone also exhibits a sudden transition to parallel-fibered tissue, longitudinal and laminar vascularity, and thinner osteocyte lacunae (Fig. 3.41). The periosteal surface does preserve an EFS as well signifying that this bone reached skeletal maturity. Similarly, the tibia preserves very little remodeling and much fewer secondary osteons scattered throughout the inner cortex. The fibula is almost entirely engulfed in

dense haversian tissue, leaving only the outermost medial cortex unobscured (Fig. 3.42). Within this region of the cortex, a transition from woven bone to parallel-fibered bone to finally lamellar bone tissue is preserved. This coincides with a rapid decrease in longitudinal vascularity towards the periosteum. Osteocyte lacunae are still large and round throughout this transition in bone tissue and vascularity. The fibula also preserves an EFS, meaning that MPC-D 107/2 most likely achieved comprehensive skeletal maturity.

Including CGMs preserved in the EFS, the femur preserves 24 CGMs, the tibia preserves 14, and the fibula preserves 20 (Fig. 3.43; Table 3.1; 3.2; 3.3). Within the EFS, CGM counts differ between bones; the femur preserves ten CGMs, the tibia preserves nine, and the fibula preserves 11. Only the femur is observed to have couplets, triplets, and quadruplets. The LAGs preserved in the EFS are grouped into four different clusters. The two outermost clusters are each a triplet of LAGs, which is then followed by a single LAG, and finally another triplet of LAGs before reaching the main cortex.

Annual Variation in CGM Spacing

Spacing between CGMs is highly variable throughout all individuals and across all sampled elements (Fig. 3.44; 3.45; 3.46). Even the two smallest specimens, MPC-D 107/7 and MPC-D 100/66, do not display a consistent trend of successive increase in spacing. At larger body sizes, spacing becomes increasingly variable. Additionally, the only specimen known to have reached skeletal maturity, MPC-D 107/2, displays variable CGM spacing within the EFS. Elements among the same individual preserve different patterns of CGM spacing. Thus, no two bones across the entire sample preserve the exact same pattern of growth when all CGMs are

considered (Fig. 3.47). This makes it difficult to correlate growth zones and years across most of the individuals (Fig. 3.47).

Couplets represent growth periods 10% or less of the previous growth period and are common across both weight bearing bones yet do not appear to be present in the fibula. Couplets only appear in specimens larger than MPC-D 100/66, therefore growth is significantly more variable beyond this size threshold (Table 3.1; 3.2). Couplet presence is variable among the bones of the same individual; Specimens, like MPC-D 100/61, can display couplets across both weight-bearing bones in relatively the same order while some specimens, like MPC-D 107/2, will display couplets in only a single bone (Table 3.1; 3.2).

When couplets have been averaged into a single CGM, spacing becomes less variable across both weight-bearing elements. Increases in growth appear to be more prominent within both elements (Fig. 3.48; 3.49). While CGM growth zones and their respective years are still difficult to correlate in the four largest specimens, smaller specimens (MPC-D 107/5 and MPC-100/98 in particular) begin to correlate more closely in their growth zones (Fig. 3.50).

Growth Curve Reconstructions

Best fit growth models differed based on the limb bone proxy data used. Tibial and fibular circumference data were best fit with non-linear models (Richards and EVF, respectively); however, femoral circumference data were best modeled by linear growth (Fig. 3.51; Table 3.4). Additionally, growth model selection for the fibula changed when specimens cut away from the mid-diaphysis were excluded from the analysis (Fig. 3.52).

When CGM circumference was converted to body mass estimates, best fit models were also different depending on the limb bone proxy (Fig. 3.55; Table 3.4). As in previous models of tyrannosaurid growth (Erickson *et al.*, 2004; Myhrvold, 2013), *Tarbosaurus* contains a short period of exponentially rapid growth in mid-life. However, robust sampling of skeletally immature individuals indicates that the non-rapid growth stage is modeled to last much longer than previously anticipated. Depending on which proxy is used, onset of rapid growth can happen anywhere from as early as seven years old to as late as mid-30's (Fig. 3.55). Such a prolonged stage consequently extends the time of the species life span; estimates for reaching sexual maturity, commonly indicated at around 75% of maximum size (Lee & O'Connor, 2013; Prondvai, 2017), range from early 20's to early 40's (Table 3.4). Skeletal maturity, defined as the effective end of growth, range anywhere from 30's to 50's (Table 3.4).

Age estimates vary depending on which limb bone proxy is used and whether data was kept as long bone circumferences or converted to body mass estimates. MPC-D 107/5 is estimated to be anywhere from 4-7 years old, with 4 being the most common estimate (Table 3.7). Estimates become increasingly variable with size of the specimen; MPC-D 107/2 is estimated to be anywhere from 29-55 years old depending on which model was used (Table 3.7).

Femoral models produced the slowest RGR and, as a result, the longest life spans to reach skeletal maturity (Table 3.4). Tibial models produced the fastest RGR and therefore produced the shortest lifespans on average (Table 3.4). Fibular models were highly variable depending on whether specimens sampled away from the mid-diaphysis were included or not (Table 3.4).

Models that include sampling near the metaphysis (N=10) produced higher RGR, smaller asymptotic sizes, the earliest inflection of all models, and occasionally older ages (Fig. 3.52). Models that did not include these individuals (N=7) produced smaller RGR, larger asymptotic sizes, the latest inflection of all models, and the youngest ages (Fig. 3.51). Of all the models, femora-based models had the least standard residual error and therefore captured less variability within their models (Table 3.4). Regarding the fibulae models, discarding individuals sampled closer to the metaphysis produced the lowest standard residual error when compared to fibulae models that included this data. Sub-sampling produced similar models for each proxy. Overall, removing annuli from each data set produced higher SRE compared to models that used the original data while removing couplets produced lower SRE compared to models that used the original data (Table 3.5; 3.6).

With the exception of models that included fibula samples away from the mid-diaphysis, all models predicted onset of rapid growth taking place no sooner than 23 years and skeletal maturity being achieved no sooner than 27 years (Table 3.5; 3.6). Subsampled tibial and fibular models were similar to models derived from the full dataset and yielded estimated similar time to maturity, whereas femoral models were more varied in their model shape parameter depending on whether the full data set of femoral data was used or one of the sub-sampled data sets was used (Fig. 3.54; 3.55; 3.56; 3.57; Table 3.5; 3.6). As a result, this had significant changes on growth rates and timing (Fig. 3.58).

Variation Based on Specimen Collection Locality

Individuals from this sample come from one of four different localities from the Nemegt Formation. Each of these localities vary in chronostratigraphic position within the formation. Our results found no significant correlation between the locality an individual was found and any growth parameter across any bone regardless of subsampling. However, MPC-D 107/14 is the only individual from Hermiin Tsav and MPC-D 100/66 is the only individual from Altan Uul. One individual is not diagnostic of an entire population from a locality, therefore further sampling of individuals is required to adequately test for spatiotemporal differences in growth.

REFERENCES

- Bell PR, (2010) “*Palaeopathological changes in a population of *Albertosaurus sarcophagus* from the Upper Cretaceous Horseshoe Canyon Formation of Alberta, Canada*” *Can. J. Earth Sci.* 47: 1263–1268
- Daffner RH, Pavlov H, (1992) “*Stress Fractures: Current Concepts*” *AJR* 159:245-252
- Enlow, D. H. (1963) “*Principles of Bone Remodeling: An Account of Post-Natal Growth and Remodeling Processes in Long Bones and the Mandible*” Charles C. Thomas, Springfield
- Erickson, G.M., Makovicky, P.J., Currie, P.J., Norell, M.A., Yerby, S.A., Brochu, C.A. (2004) “*Gigantism and comparative life-history parameters of tyrannosaurid dinosaurs.*” *Nature.* 430, 772–775
- Lee AH, O’Connor PM. (2013) “*Bone histology confirms determinate growth and small body size in the noosaurid theropod *Masiakasaurus knopfleri*.*” *Journal of Vertebrate Paleontology* 33:865–76
- Lipkin C, Carpenter K, (2008) “Looking Again At The Forelimb Of Tyrannosaurus Rex” *Tyrannosaurus rex, the Tyrant King (Life of the Past)*, Indiana University Press
- Myhrvold NP (2013) “*Revisiting the Estimation of Dinosaur Growth Rates*” *PLoS ONE* 8(12): e81917. doi:10.1371/journal.pone.0081917
- Prondvai E, (2017) “*Medullary bone in fossils: function, evolution and significance in growth curve reconstructions of extinct vertebrates*” *J . EVOL. BIOL.* 30 440–460
- Rothschild, B. M. (1988) “*Stress fracture in a ceratopsian phalanx*” *Journal of Paleontology* 62: 302-304.
- Rothschild, B. M., and Martin, L. D. (1993) “*Paleopathology: Disease in the Fossil Record*” CRC Press. Boca Raton. FL.

Rothschild BM, Tanke DH, (2005) “*Theropod Paleopathology*” The Carnivorous Dinosaur. Indiana University Press. P 351-365

Rothschild B, Tanke DH, Ford DL. (2001) “*Theropod stress fractures and tendon avulsions as a clue to activity*” In Tanke DH, Carpenter K, editors. Mesozoic vertebrate life. Bloomington: Indiana University Press; pp. 331–336.

Tsuihiji T, Watabe M, Tsogtbaatar K, Tsubamoto T, Barsbold R, Suzuki S, Lee AH, Ridgely RC, Kawahara Y, Witmer LW, (2011) “*Cranial osteology of a juvenile specimen of Tarbosaurus bataar from the Nemegt Formation (Upper Cretaceous) of Bugin Tsav, Mongolia*” J. Vertebr. Paleontol. 31, 497–517.

FIGURES



Figure 3.1. Histological thin section of MPC-D 107/7 Femur under plain polarized light. Scale bar equals 1mm.



Figure 3.2. Histological thin section of MPC-D 107/7 Tibia under plain polarized light. Scale bar equals 1mm.



Figure 3.3. Histological thin section of MPC-D 107/7 Fibula under plain polarized light. Scale bar equals 1mm.

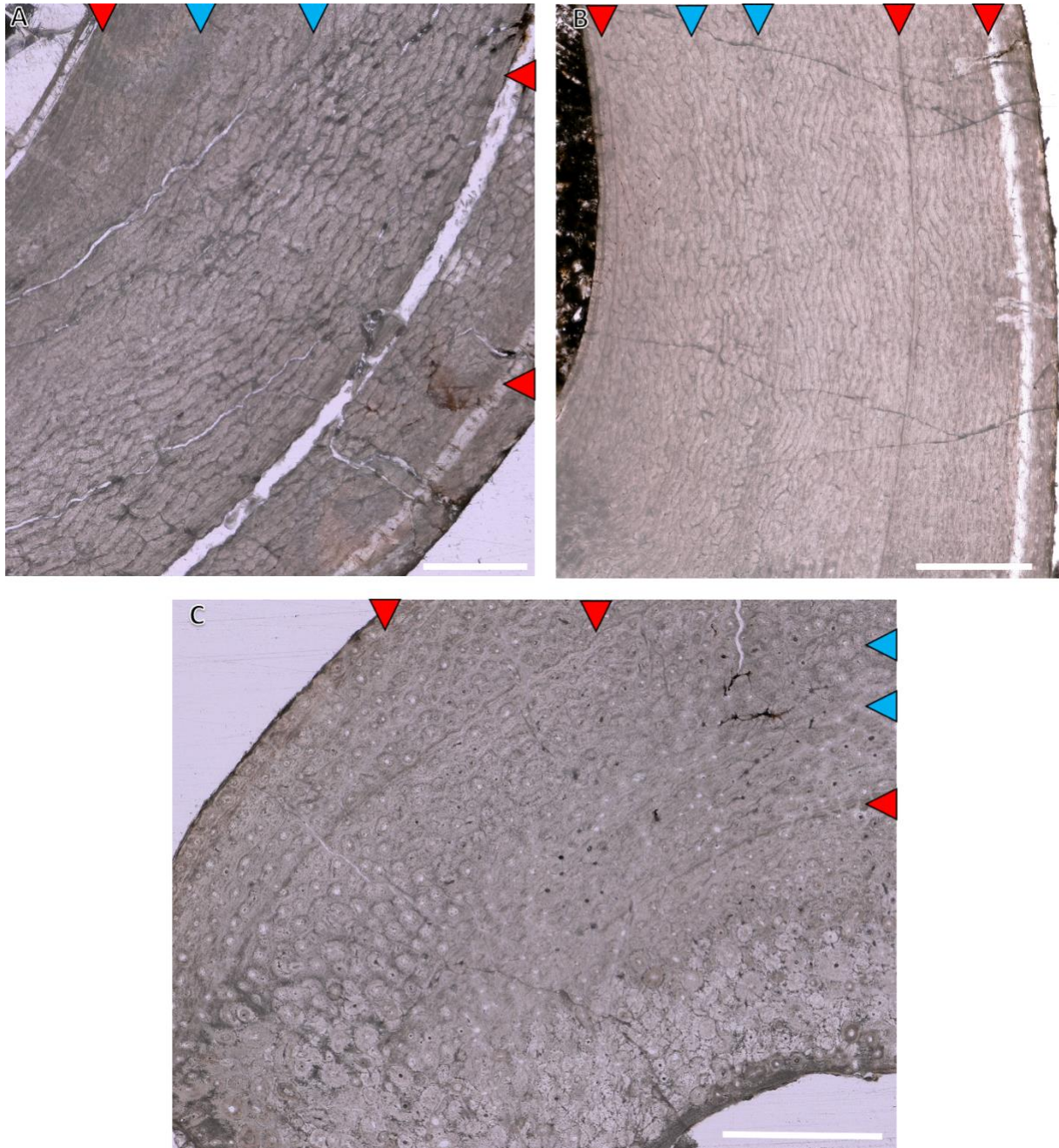


Figure 3.4. CGMs found in MPC-D 107/7 under plain polarized light. (A) Femur (B) Tibia, and (C) Fibula. Red arrows indicate LAGs and blue arrows indicate annuli. Scale bar equals 1mm.



Figure 3.5. Histological thin section of MPC-D 100/66 Femur. Scale bar equals 1mm.



Figure 3.6. Histological thin section of MPC-D 100/66 Tibia. Scale bar equals 1mm.

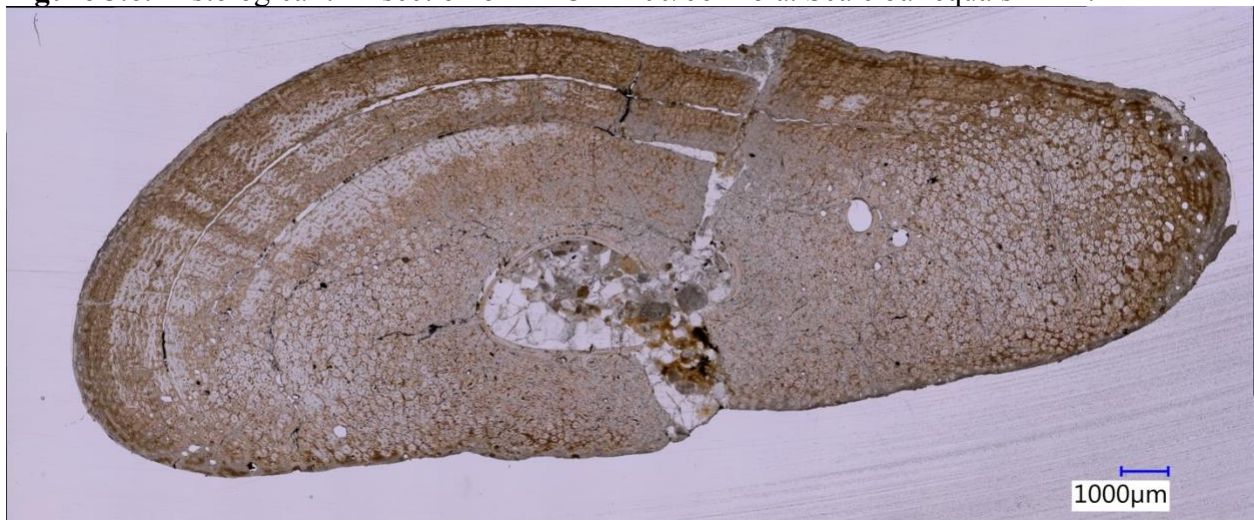


Figure 3.7. Histological thin section of MPC-D 100/66 Fibula. Scale bar equals 1mm.

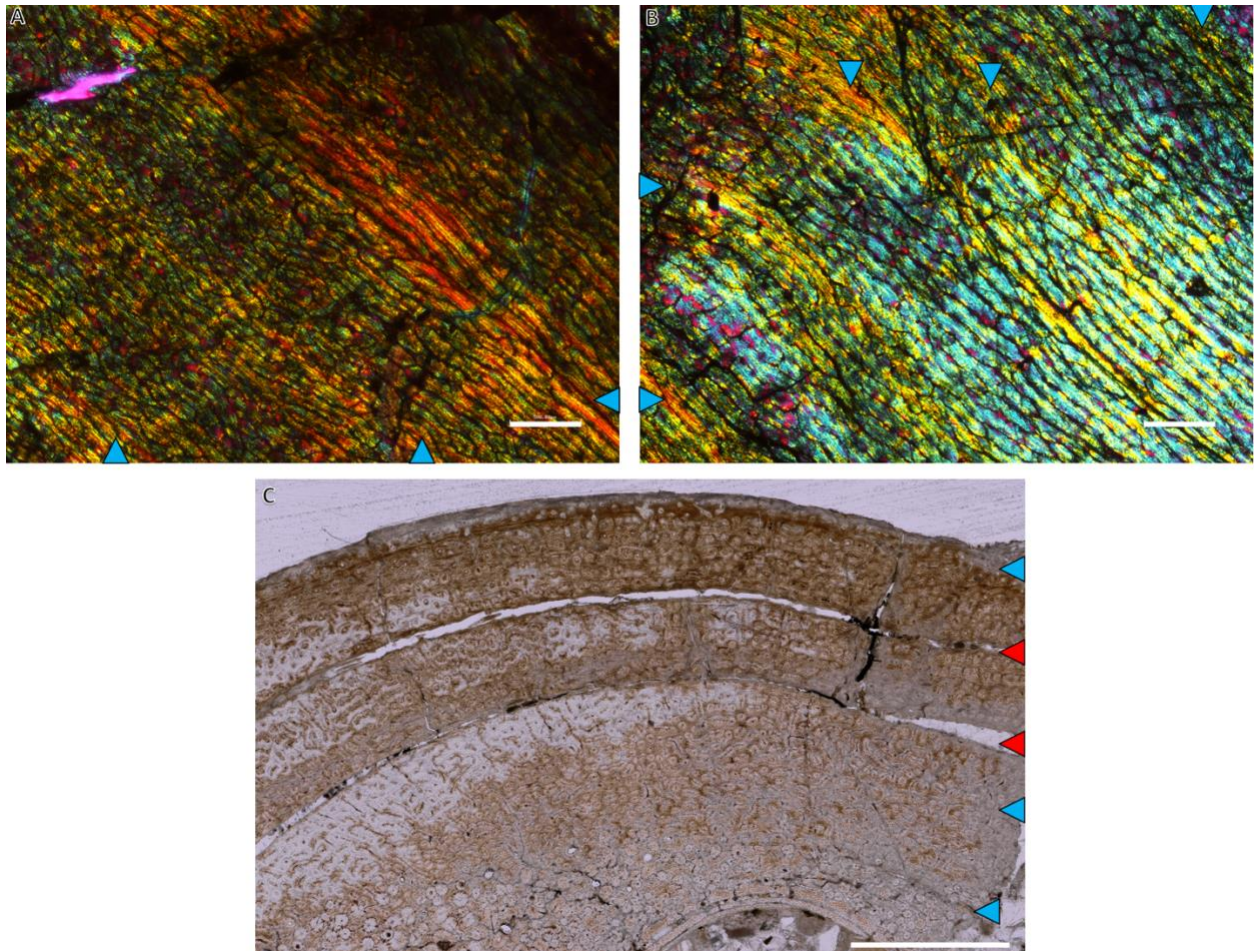


Figure 3.8. CGMs found in MPC-D 100/66 under cross-polarized light (A, B) and plain polarized light (C). (A) Femur (B) Tibia, and (C) Fibula. Red arrows indicate LAGs and blue arrows indicate annuli. Scale bar in A & B equals 0.5mm. Scale bar in C equals 1mm.



Figure 3.9. Histological thin section of MPC-D 100/62 Femur. Scale bar equals 1mm.



Figure 3.10. Histological thin section of MPC-D 100/62 Tibia. Scale bar equals 1mm.



Figure 3.11. Histological thin section of MPC-D 100/62 Fibula. Scale bar equals 1mm.

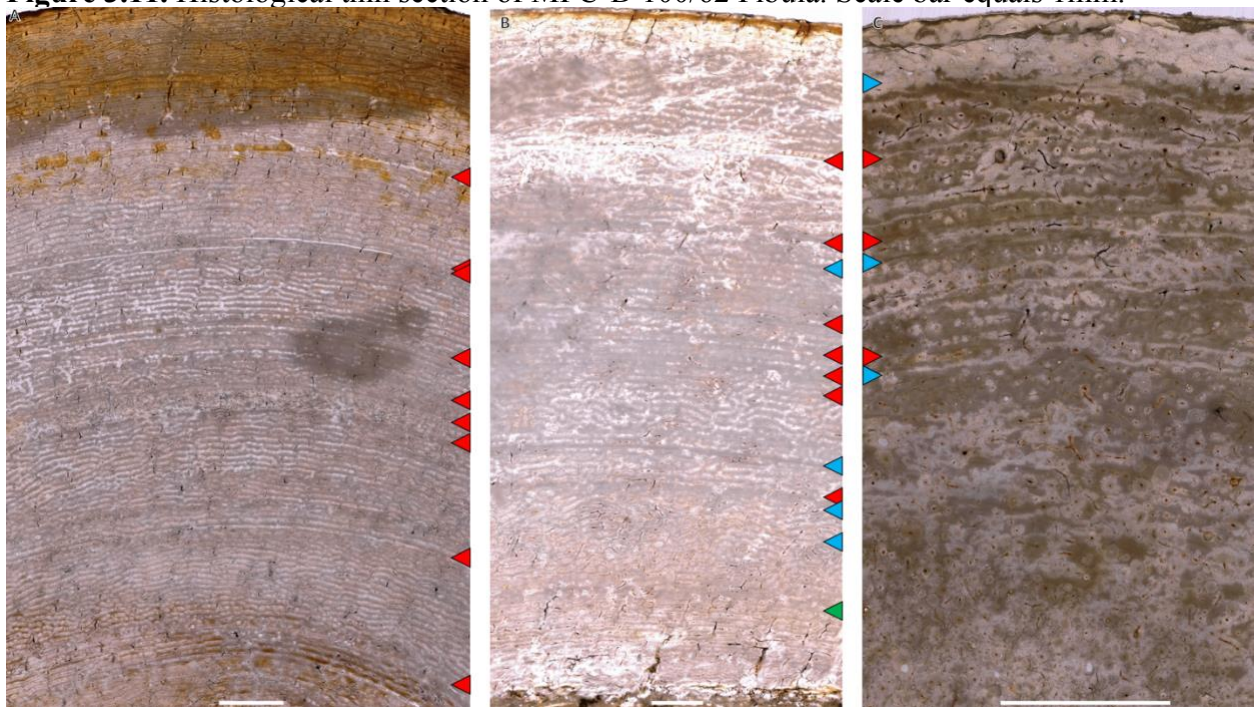


Figure 3.12. CGMs found in MPC-D 100/62 under plain polarized light. (A) Femur (B) Tibia, and (C) Fibula. Red arrows indicate LAGs, green arrows indicate multi-LAGs, and blue arrows indicate annuli. Scale bar in equals 1mm.

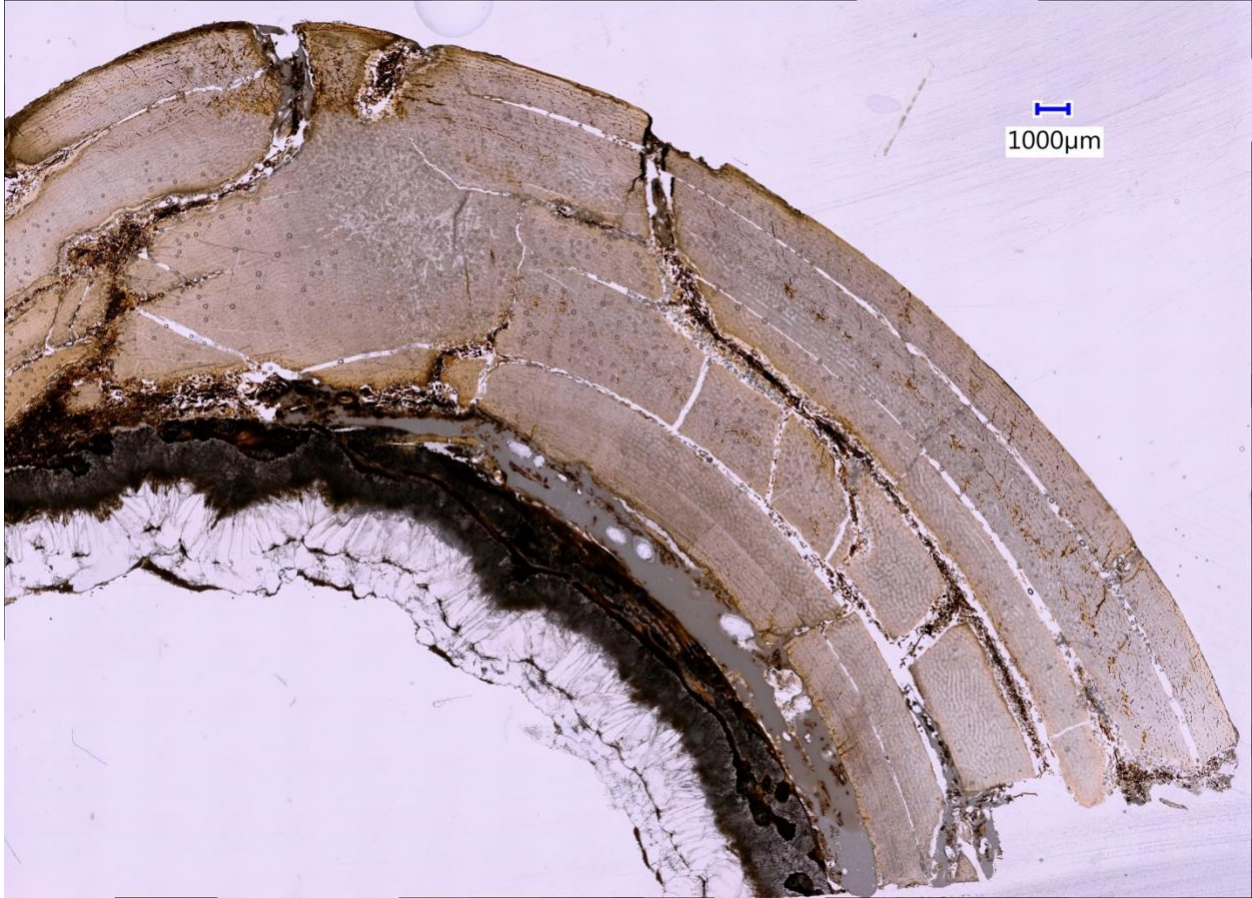


Figure 3.13. Histological thin section of MPC-D 107/5 Femur. Scale bar equals 1mm.



Figure 3.14. Histological thin section of MPC-D 107/5 Fibula. Scale bar equals 1mm.

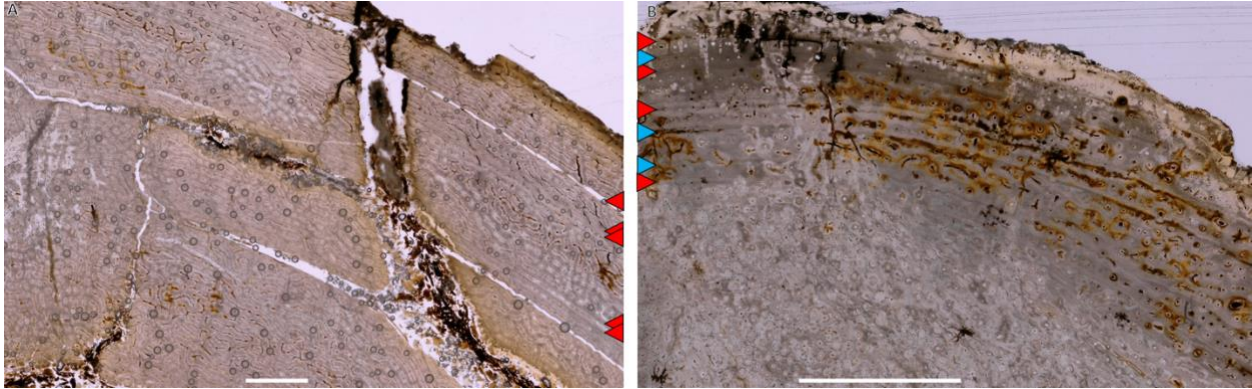


Figure 3.15. CGMs found in MPC-D 107/5 under plain polarized light. (A) Femur and (B) Fibula. Red arrows indicate LAGs and blue arrows indicate annuli. Scale bar in equals 1mm.

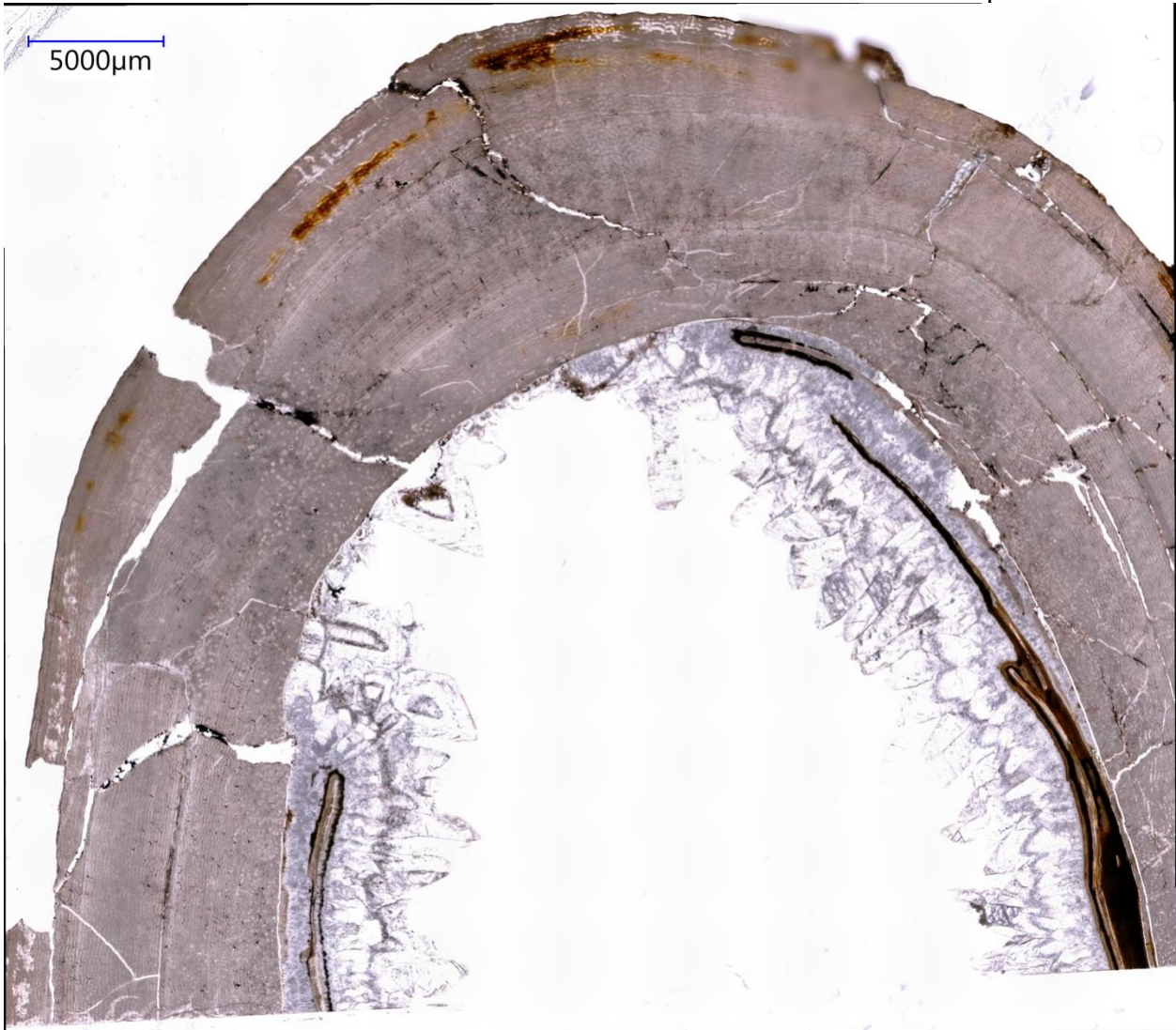


Figure 3.16. Histological thin section of MPC-D 107/14 Femur. Scale bar equals 5mm.

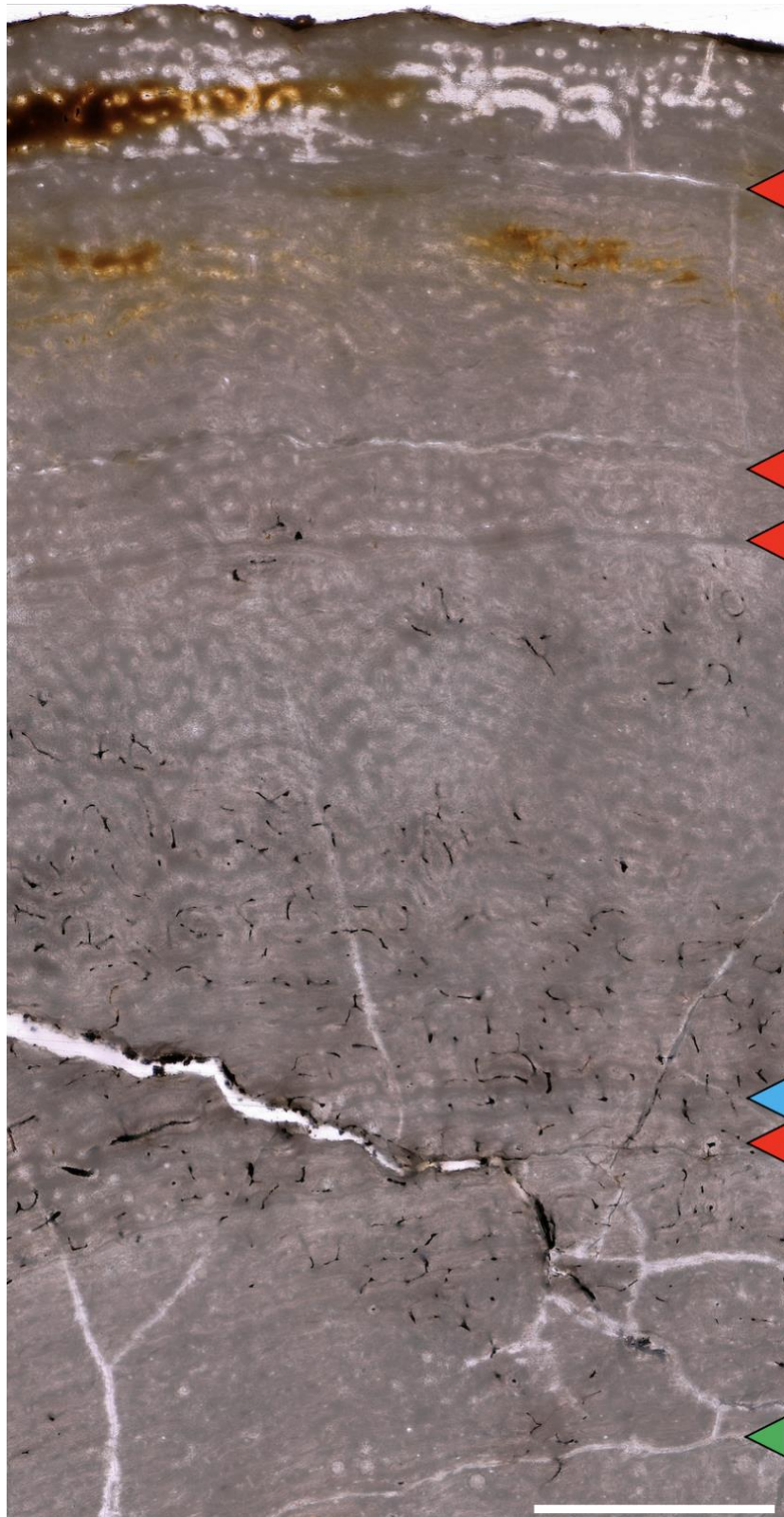
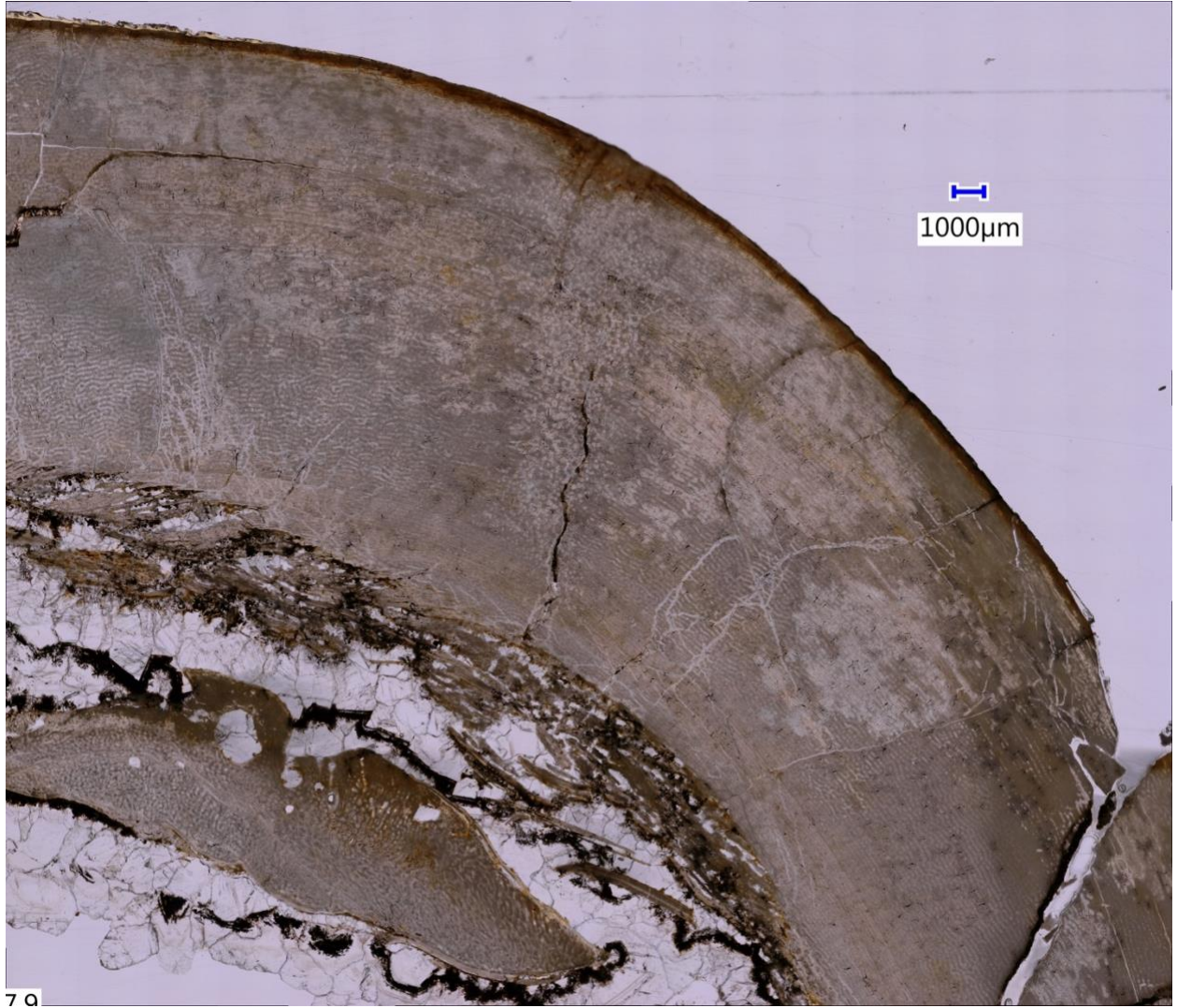


Figure 3.17. CGMs found in MPC-D 107/14 Femur under plain polarized light. Red arrows indicate LAGs, green arrows indicate multi-LAGs, and blue arrows indicate annuli. Scale bar in equals 1mm.



70

Figure 3.18. Histological thin section of MPC-D 100/70 Femur. Scale bar equals 1mm.

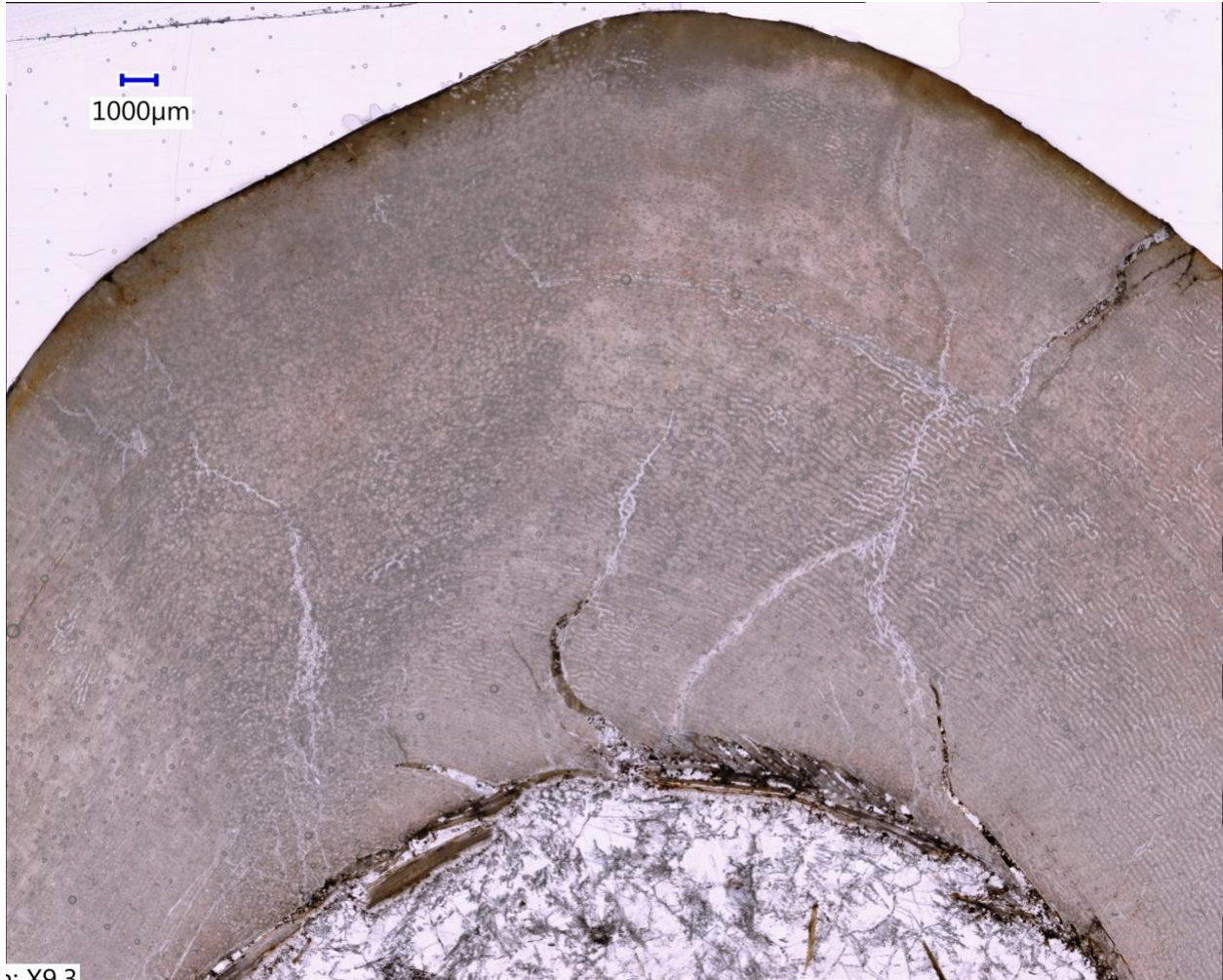


Figure 3.19. Histological thin section of MPC-D 100/70 Tibia. Scale bar equals 1mm.

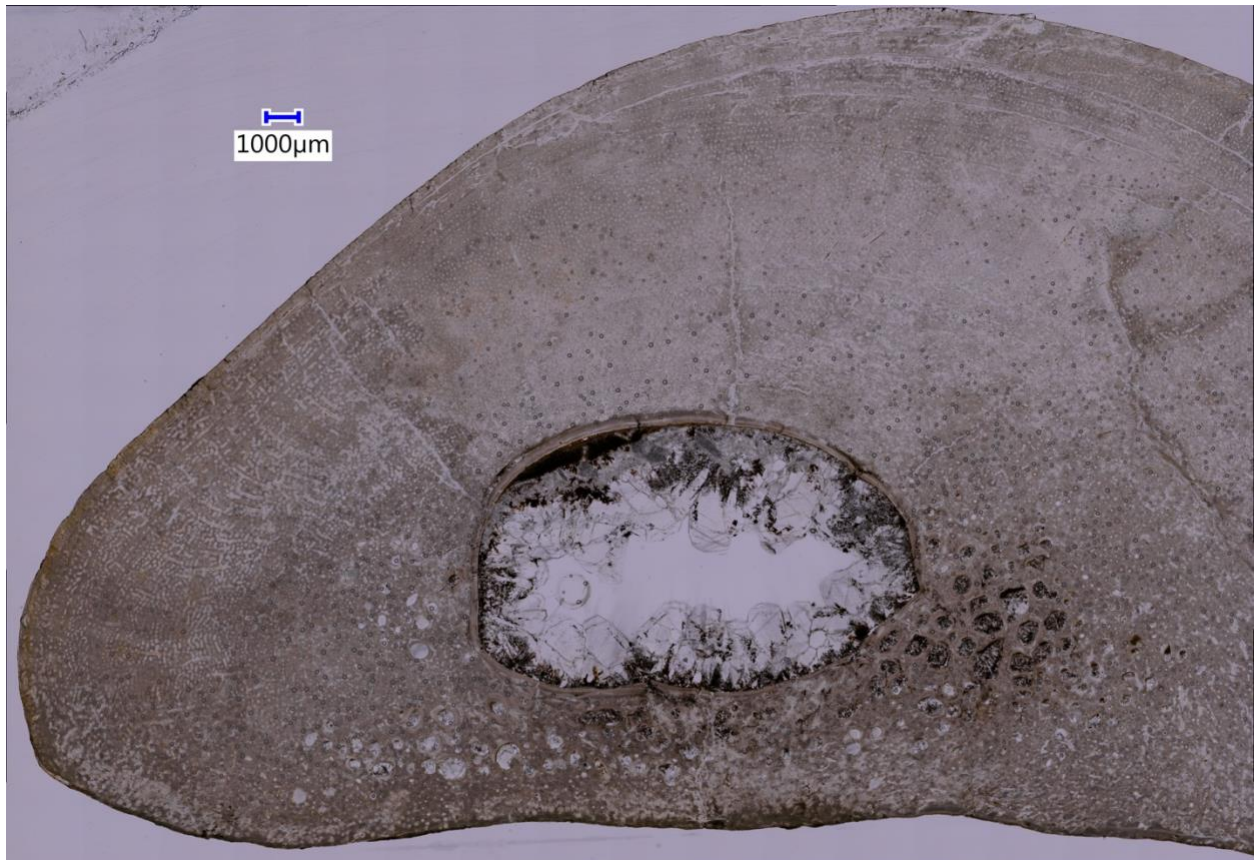


Figure 3.19. Histological thin section of MPC-D 100/70 Fibula. Scale bar equals 1mm.

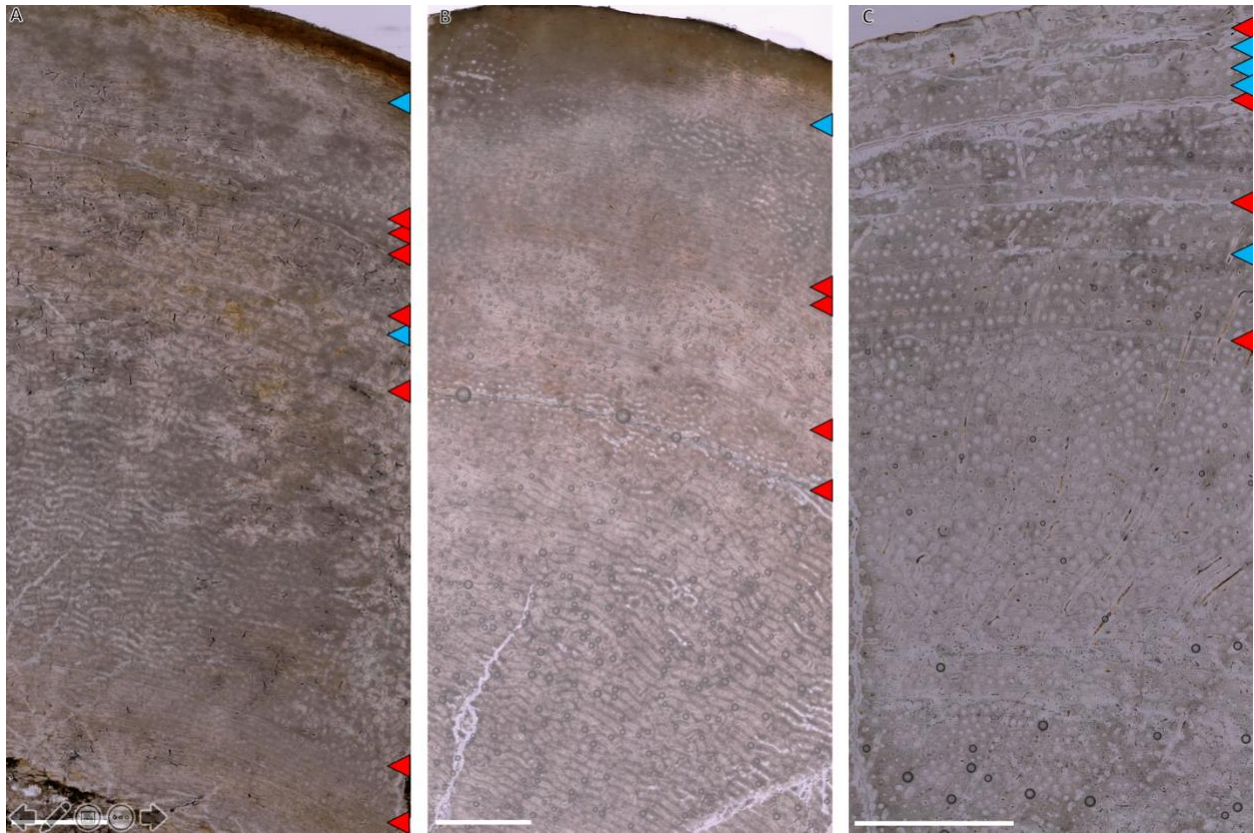
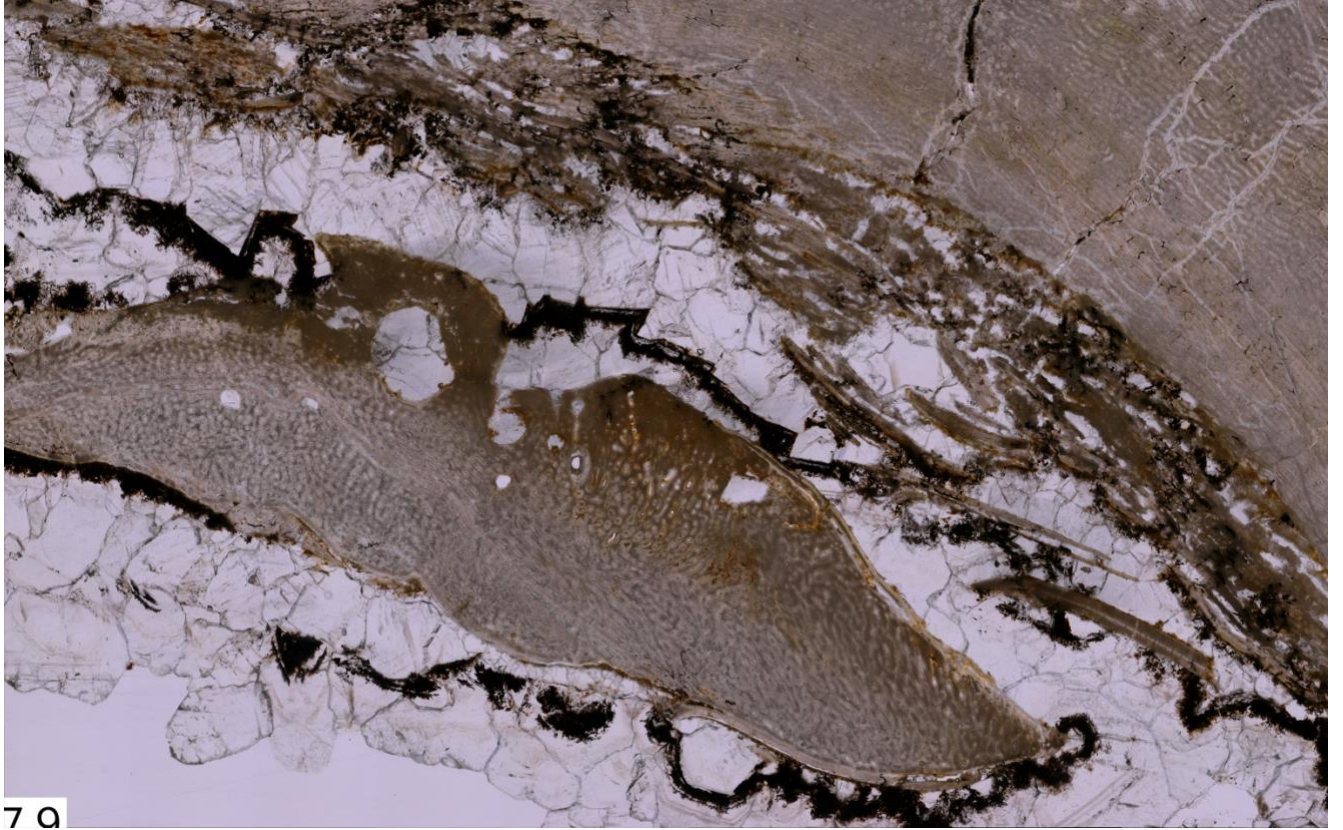


Figure 3.21. CGMs found in MPC-D 100/70 under plain polarized light. (A) Femur (B) Tibia, and (C) Fibula. Red arrows indicate LAGs and blue arrows indicate annuli. Scale bar in equals 1mm.



7 Q

Figure 3.22. Pathology found in medullary cavity of MPC-D 100/70 Femur.

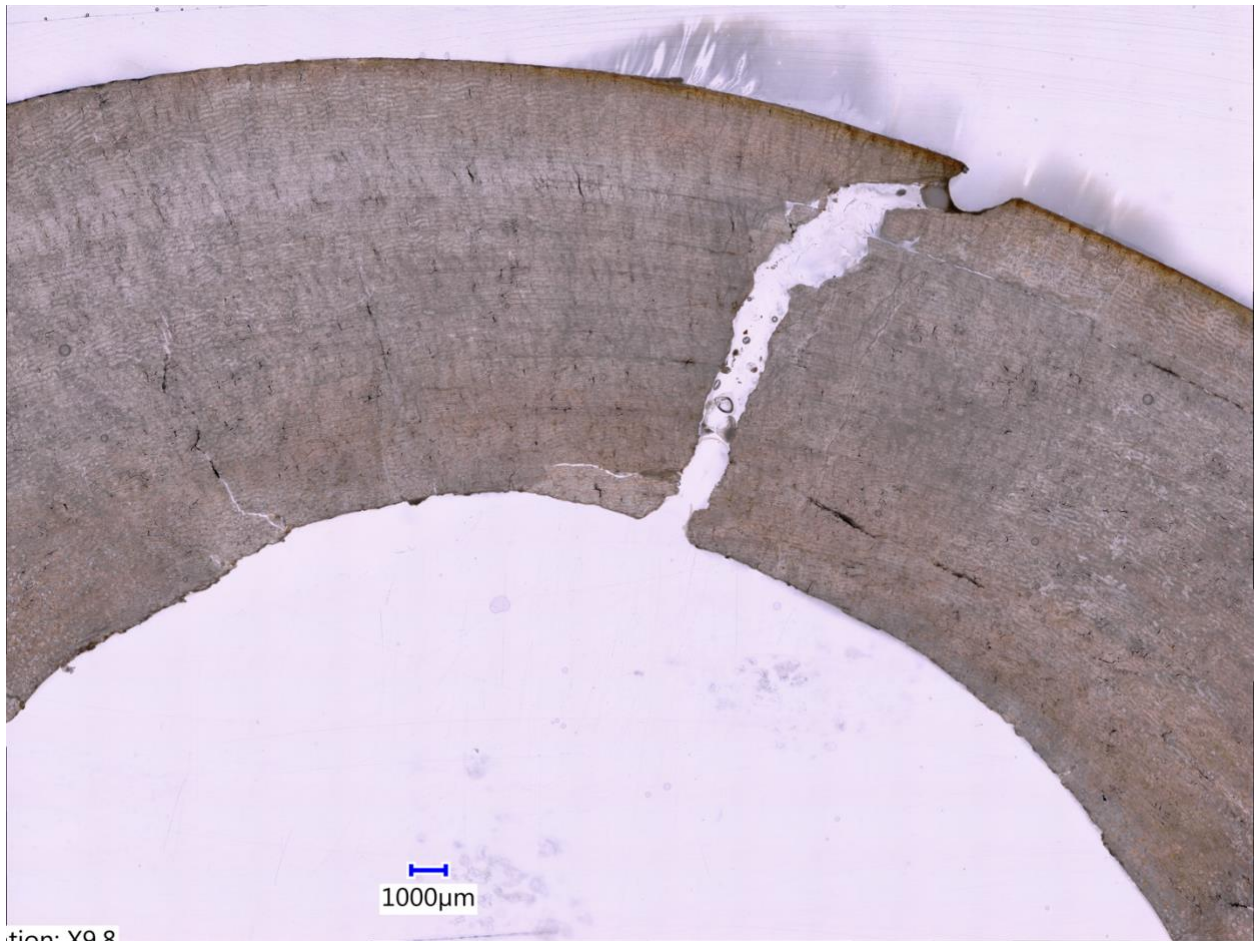


Figure 3.23. Histological thin section of MPC-D 100/98 Femur. Scale bar equals 1mm.

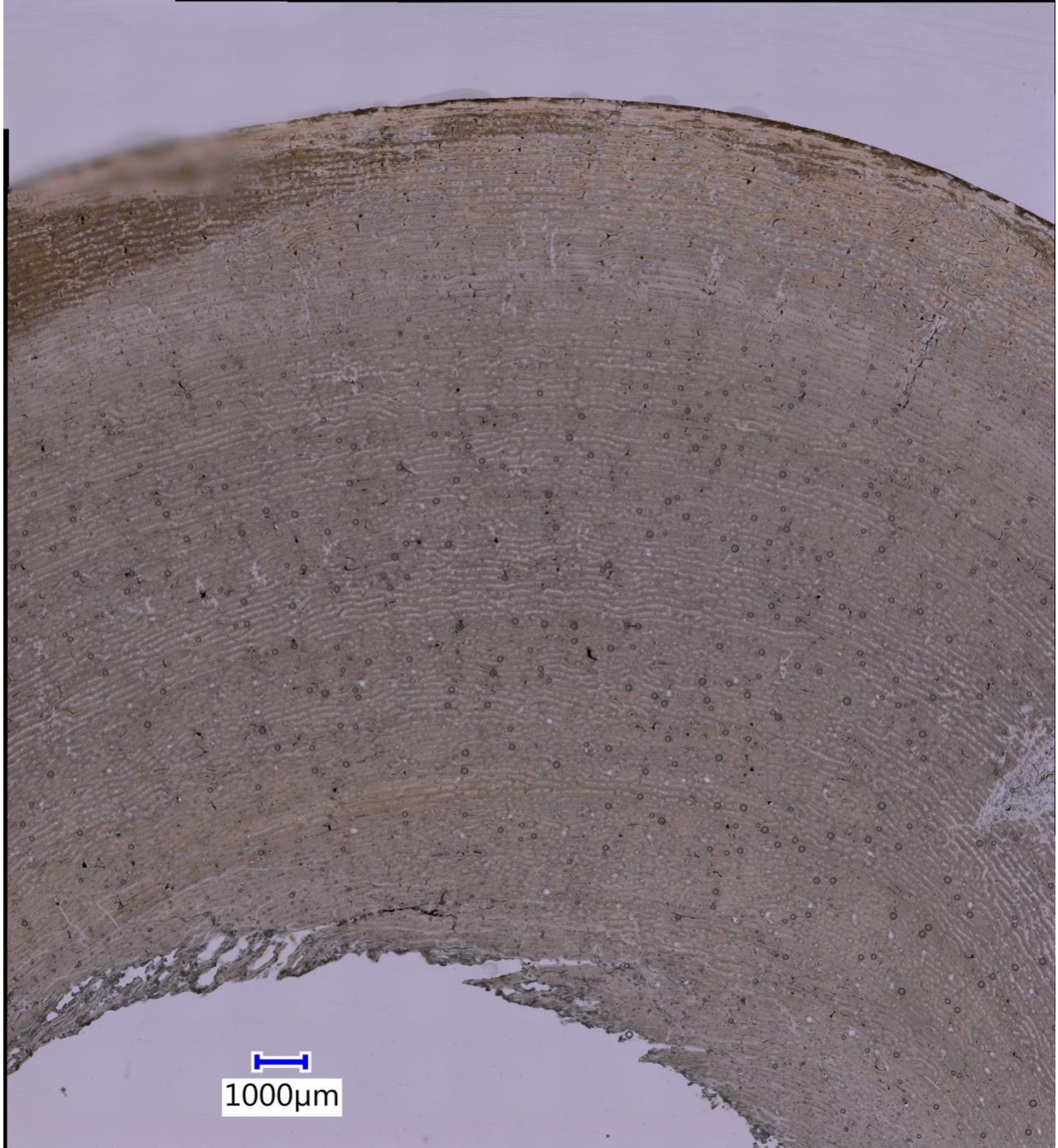


Figure 3.24. Histological thin section of MPC-D 100/98 Tibia. Scale bar equals 1mm.



Figure 3.25. Histological thin section of MPC-D 100/98 Fibula. Scale bar equals 1mm.

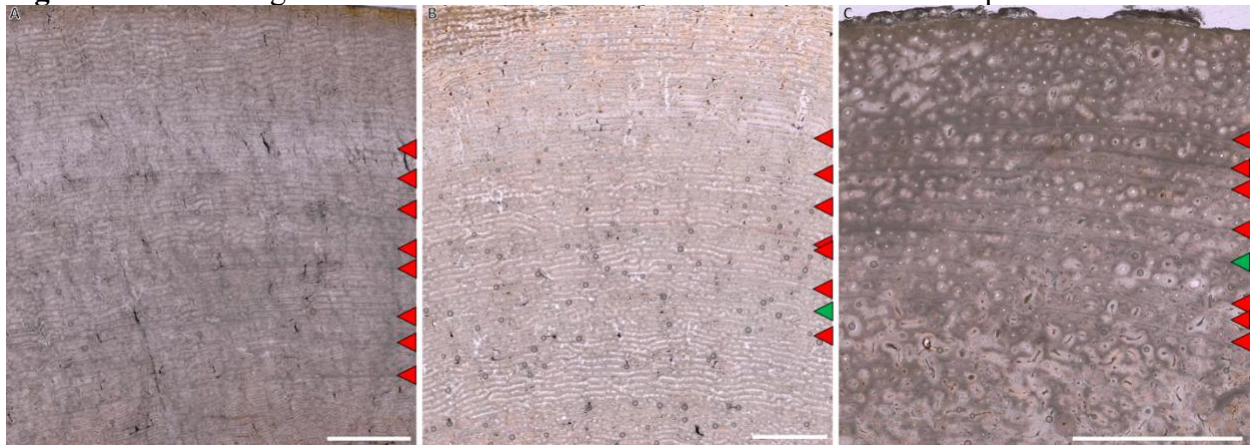


Figure 3.26. CGMs found in MPC-D 100/98 under plain polarized light. (A) Femur (B) Tibia, and (C) Fibula. Red arrows indicate LAGs and green arrows indicate multi-LAGs. Scale bar in equals 1mm.

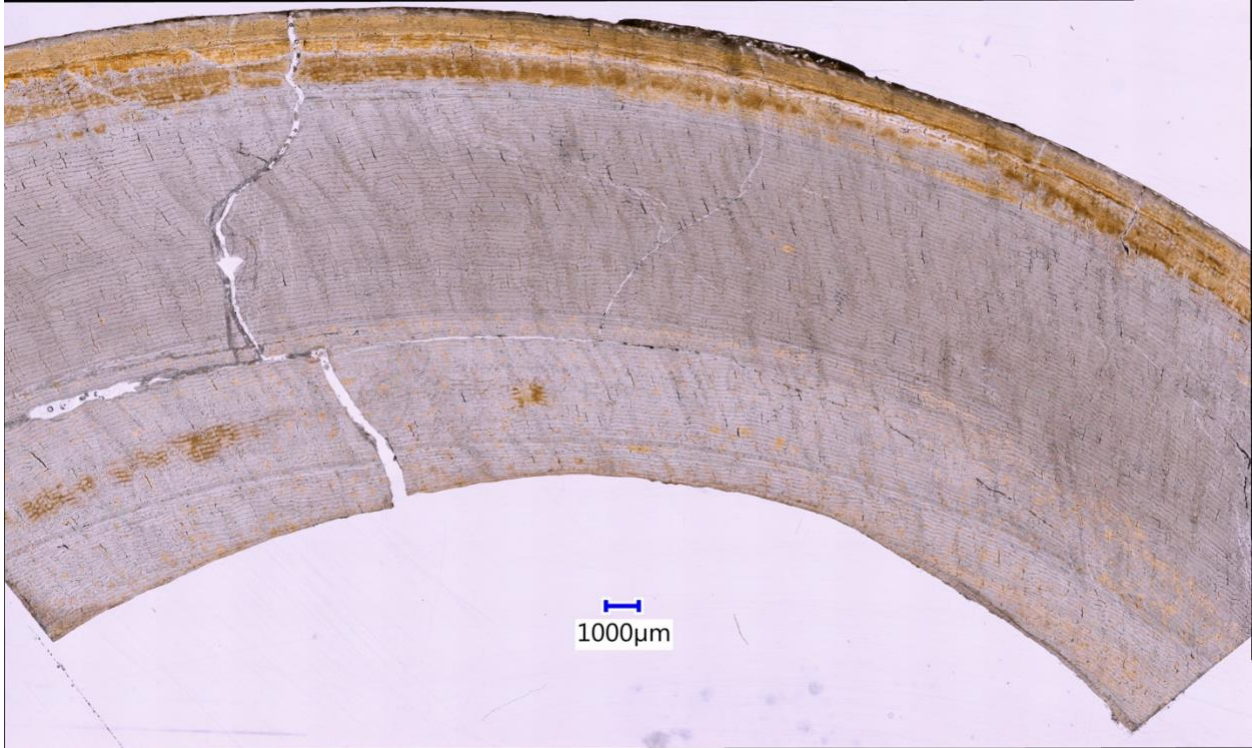


Figure 3.27. Histological thin section of MPC-D 100/61 Femur. Scale bar equals 1mm.



Figure 3.28. Histological thin section of MPC-D 100/61 Tibia. Scale bar equals 1mm.

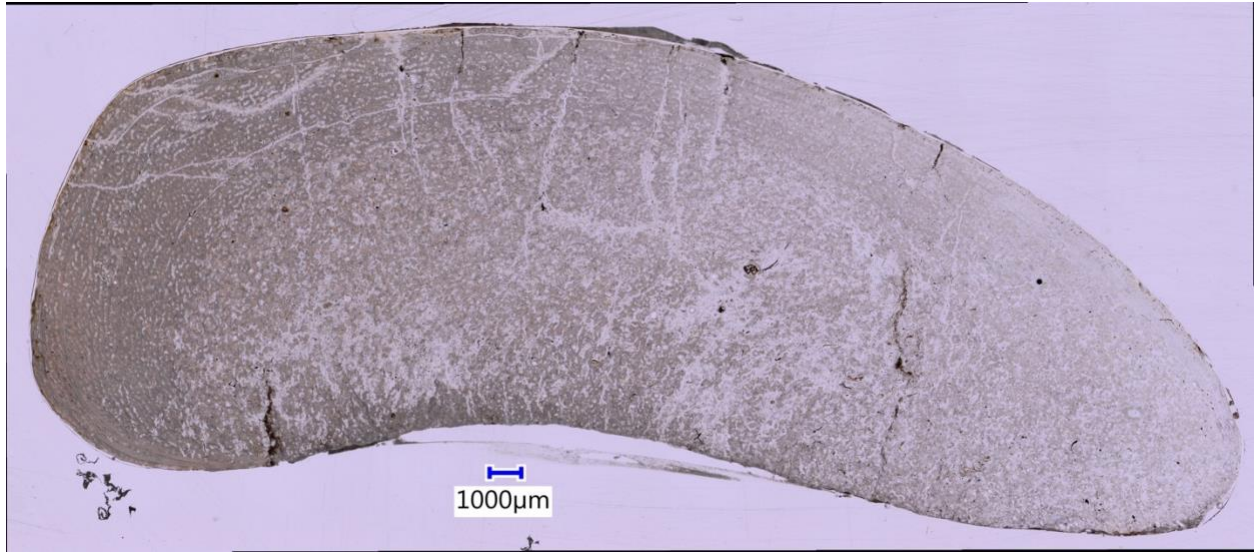


Figure 3.29. Histological thin section of MPC-D 100/61 Fibula. Scale bar equals 1mm.

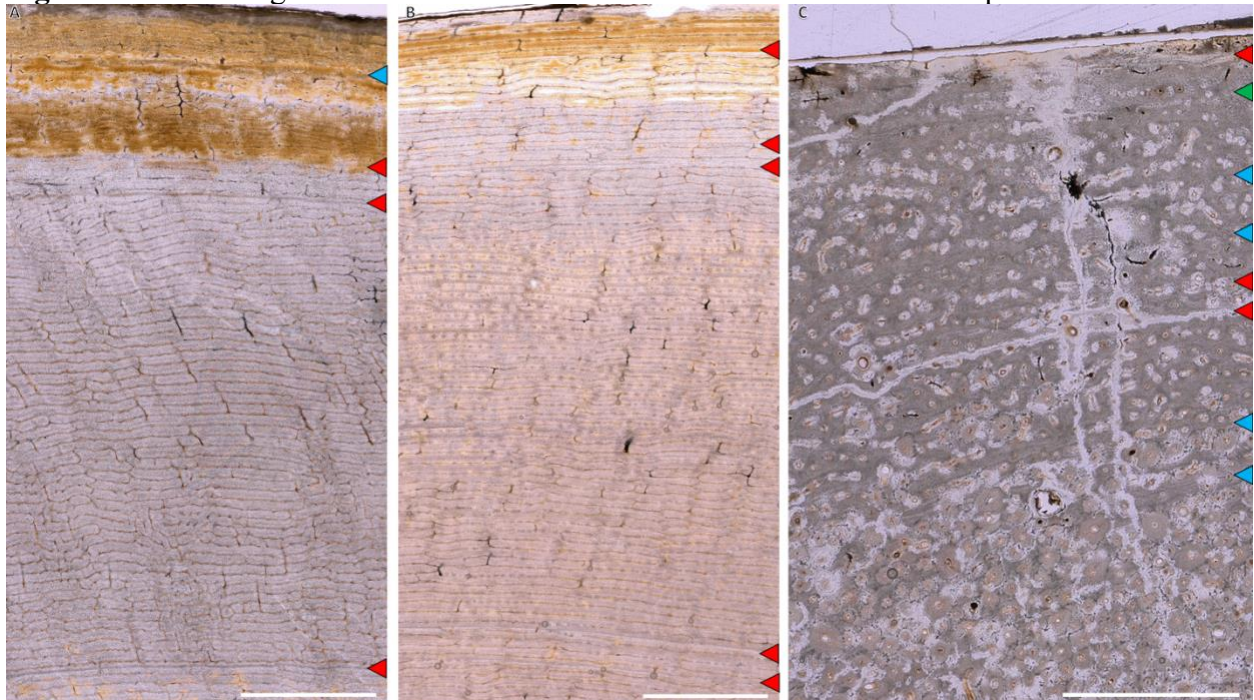


Figure 3.30. CGMs found in MPC-D 100/61 under plain polarized light. (A) Femur (B) Tibia, and (C) Fibula. Red arrows indicate LAGs, green arrows indicate multi-LAGs, and blue arrows indicate annuli. Scale bar in equals 1mm.



Figure 3.31. Histological thin section of MPC-D 107/4 Tibia. Scale bar equals 1mm.



Figure 3.32. CGMs found in MPC-D 107/4 Tibia under plain polarized light. Red arrows indicate LAGs. Scale bar in equals 1mm.



Figure 3.33. Histological thin section of MPC-D 100/64 Tibia. Scale bar equals 1mm.



Fig. V&A

Figure 3.34. Histological thin section of MPC-D 100/64 Fibula from diaphysis. Scale bar equals 1mm.

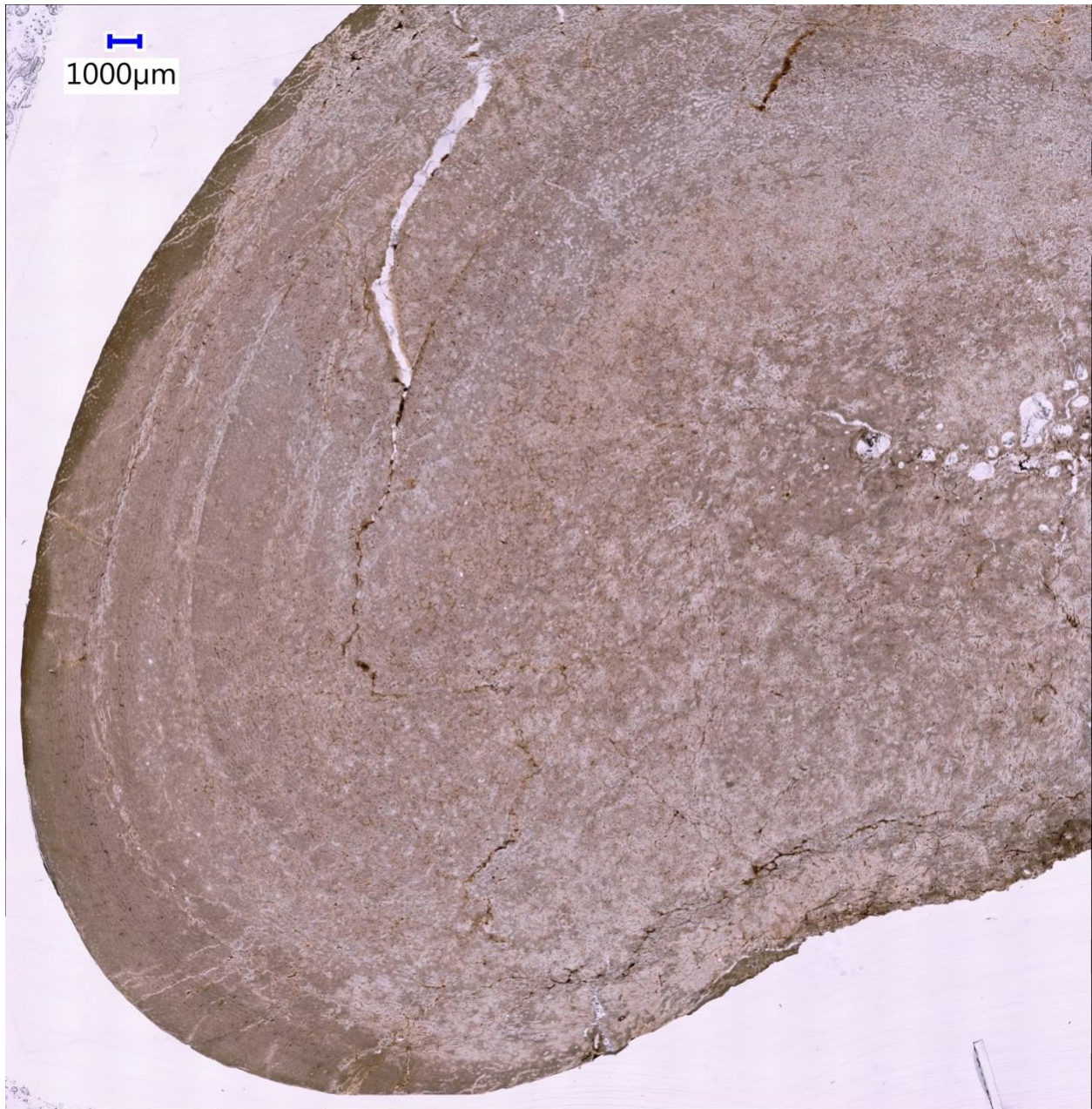


Figure 3.35. Histological thin section of MPC-D 100/64 Fibula near metaphysis. Scale bar equals 1mm.

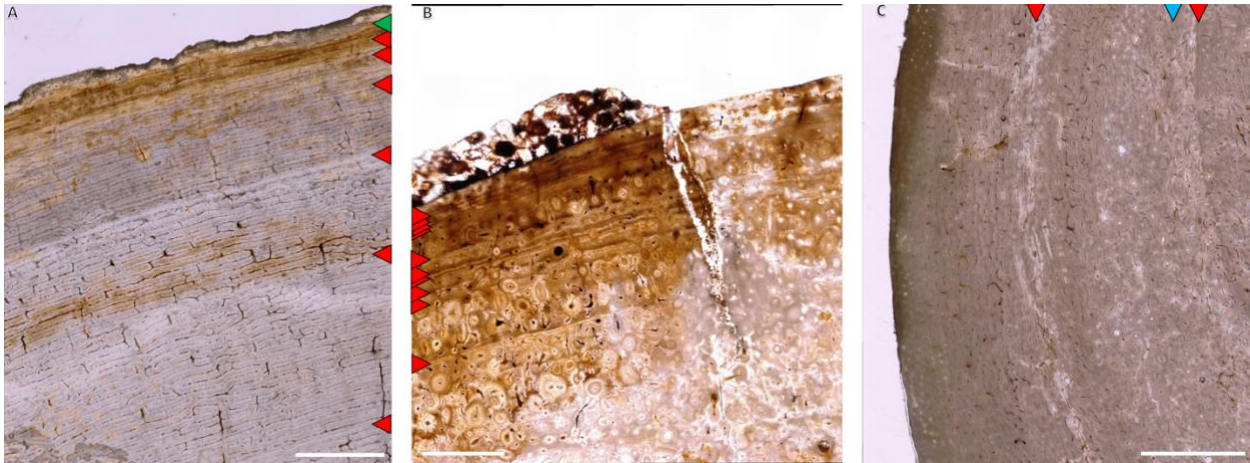


Figure 3.36. CGMs found in MPC-D 100/64 under plain polarized light. (A) Tibia (B) Fibula from the diaphysis, and (C) Fibula near metaphysis. Red arrows indicate LAGs, green arrows indicate multi-LAGs, and blue arrows indicate annuli. Scale bar in equals 1mm.



Figure 3.37. Histological thin section of MPC-D 100/63 Femur. Scale bar equals 1mm.



Figure 3.38. Histological thin section of MPC-D 100/63 Tibia. Scale bar equals 1mm.

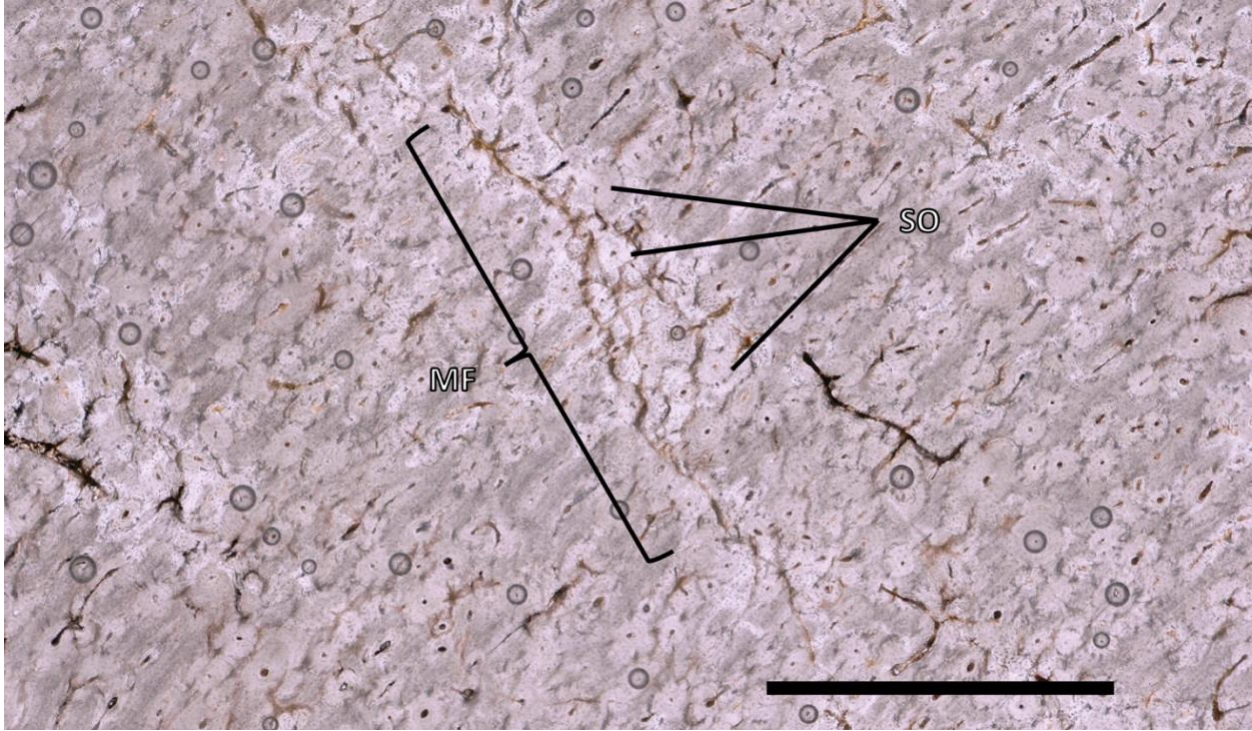


Figure 3.39. Close up of a single microfracture undergoing secondary remodeling in MPC-D 100/63 tibia. Microfractures such as this one are present throughout most of the histological section and are remodeled to the same degree. Apart from microfractures, secondary osteons are prevalent throughout the entire cortex. MF – microfracture, SO – secondary osteon. Scale bar equals 1mm.



Figure 3.40. Histological thin section of MPC-D 107/2 Femur. Scale bar equals 1mm.

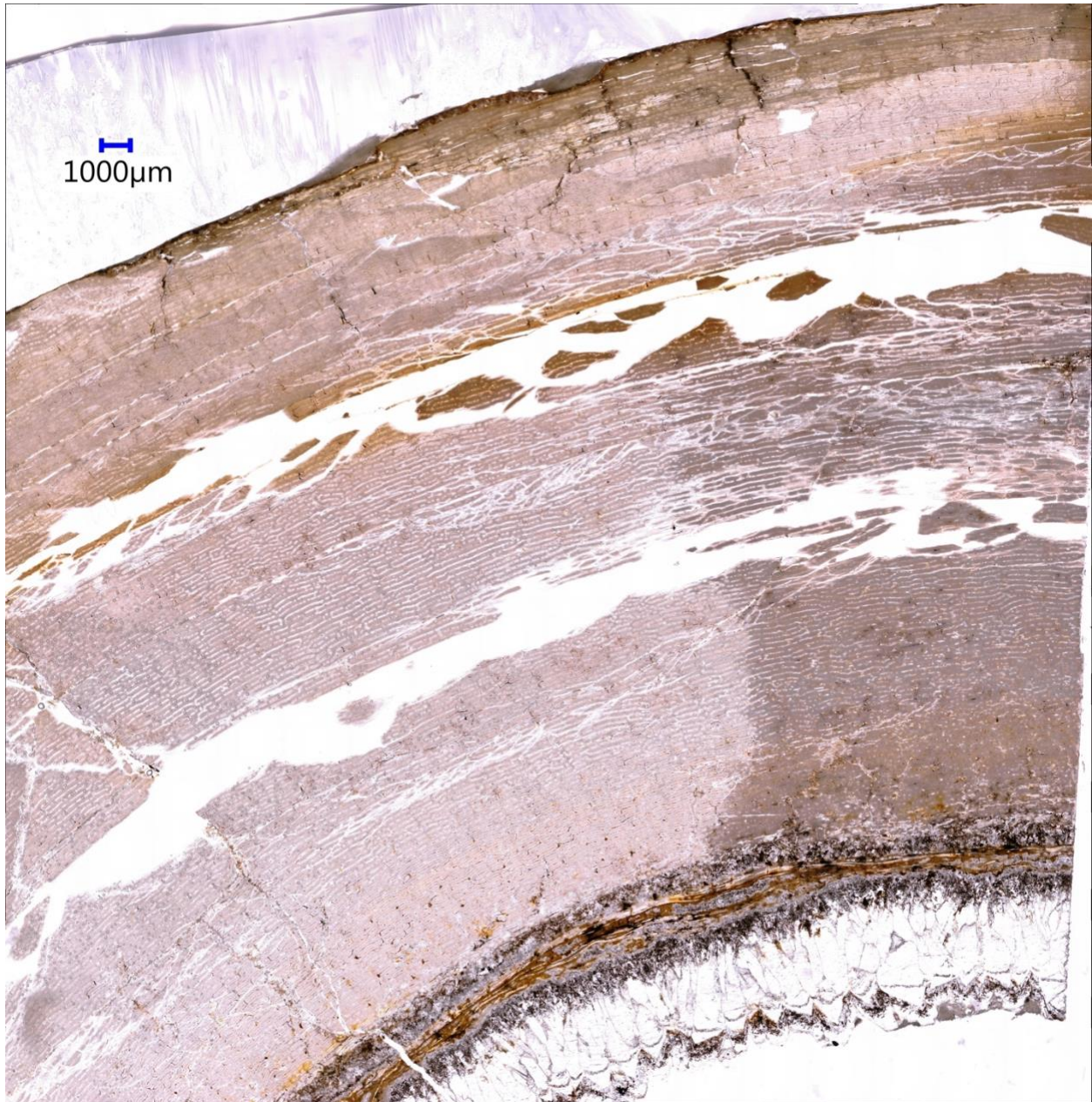


Figure 3.41. Histological thin section of MPC-D 107/2 Tibia. Scale bar equals 1mm.

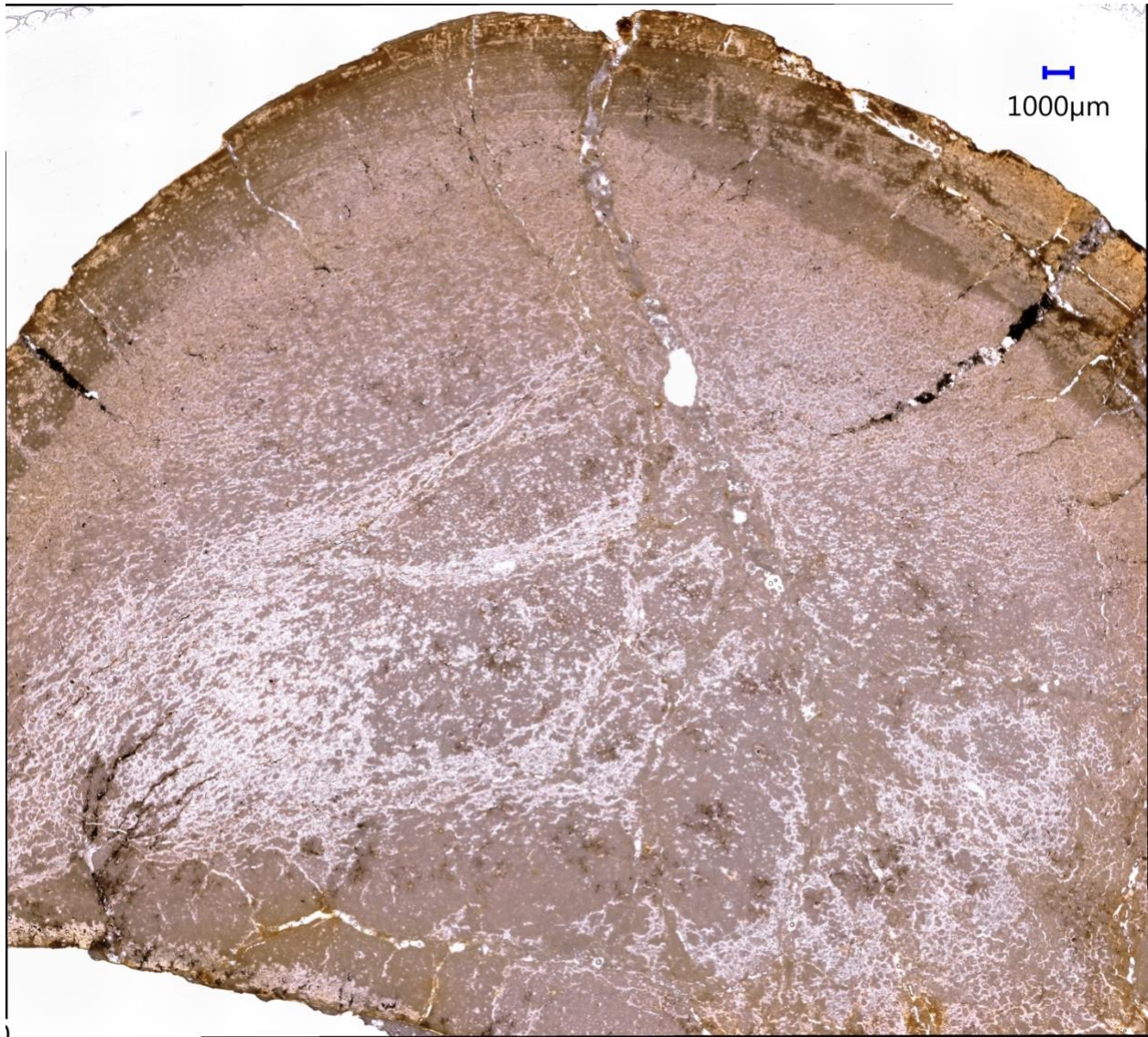


Figure 3.42. Histological thin section of MPC-D 107/2 Fibula. Scale bar equals 1mm.

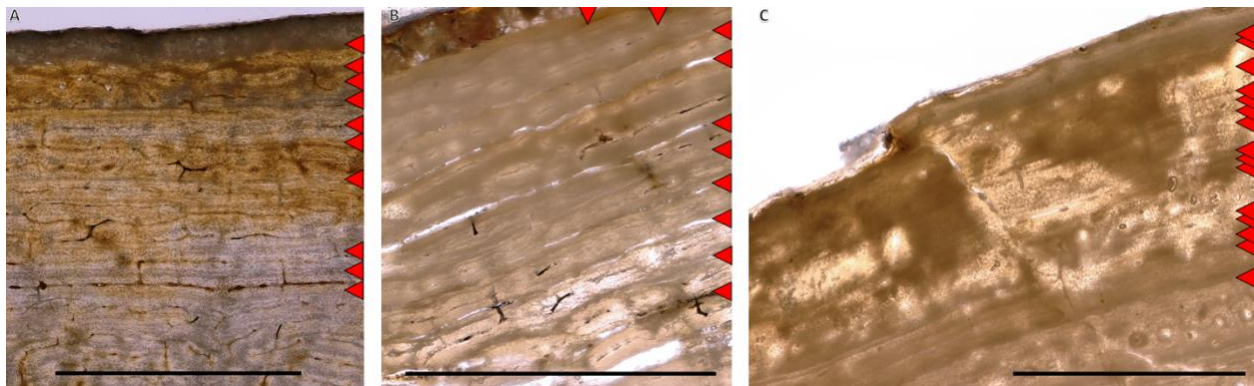


Figure 3.43. CGMs found in EFS of MPC-D 107/2 under plain polarized light. (A) Femur (B) Tibia, and (C) Fibula. Red arrows indicate LAGs. Scale bar in equals 1mm.

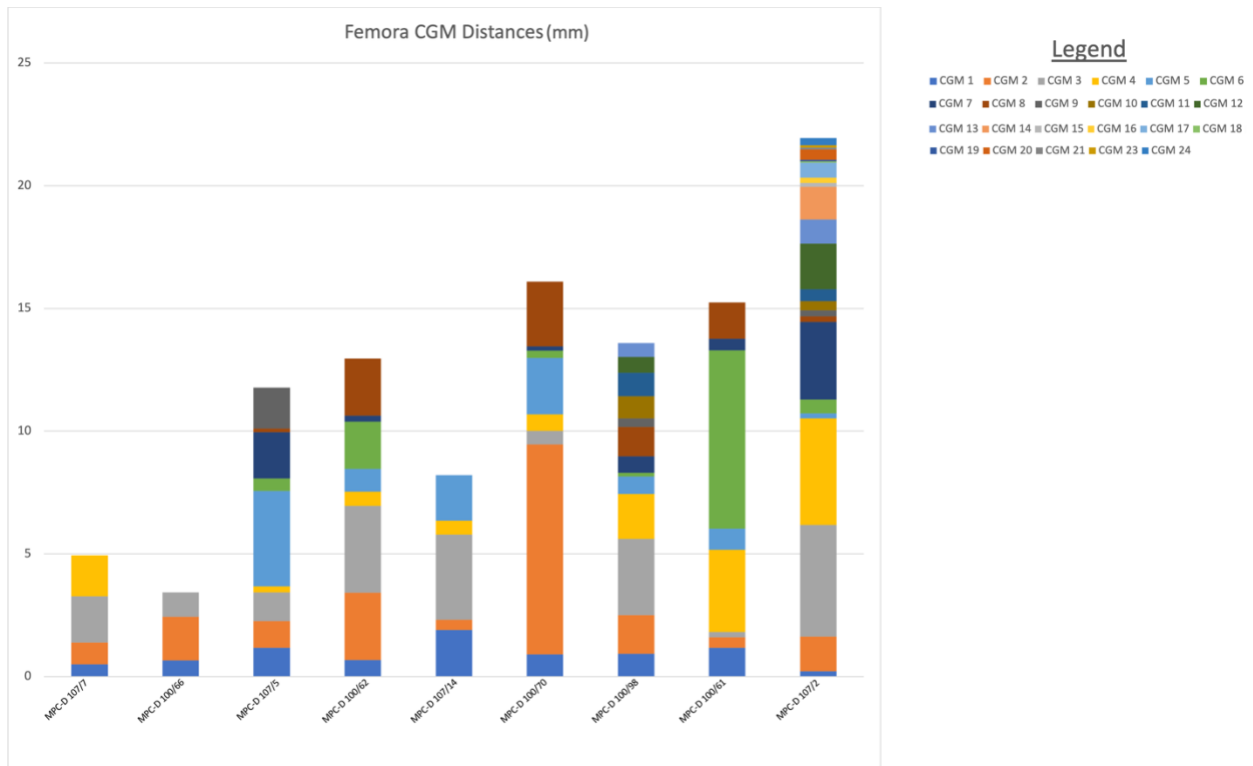


Figure 3.44. Histograms showing CGM distances throughout femora.

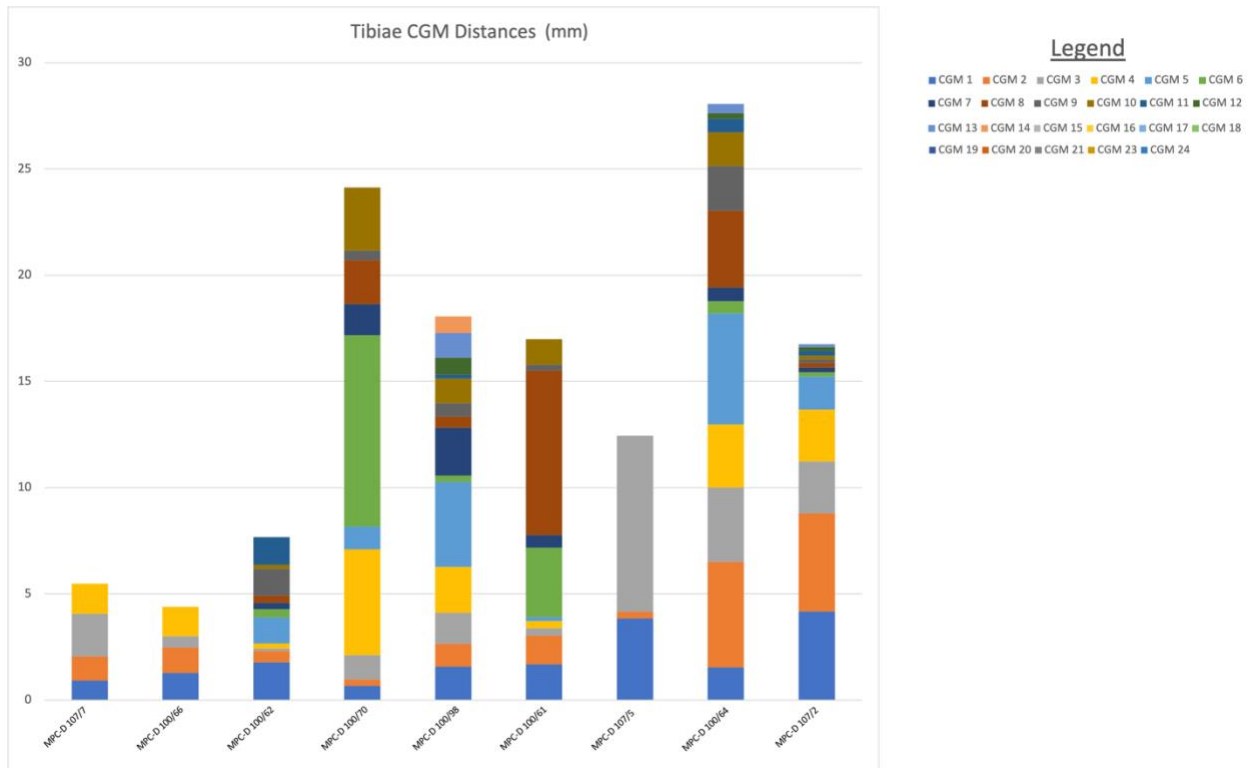


Figure 3.45. Histograms showing CGM distances throughout tibiae.

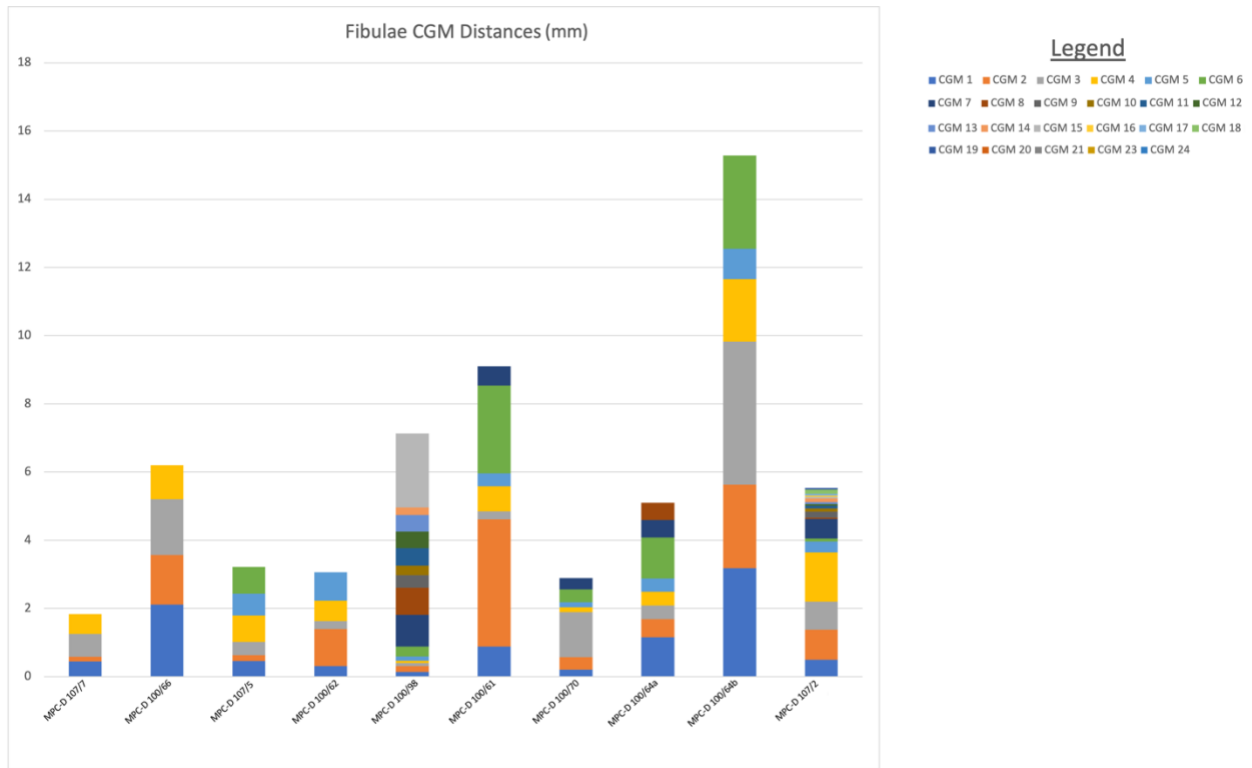


Figure 3.46. Histograms showing CGM distances throughout fibulae.

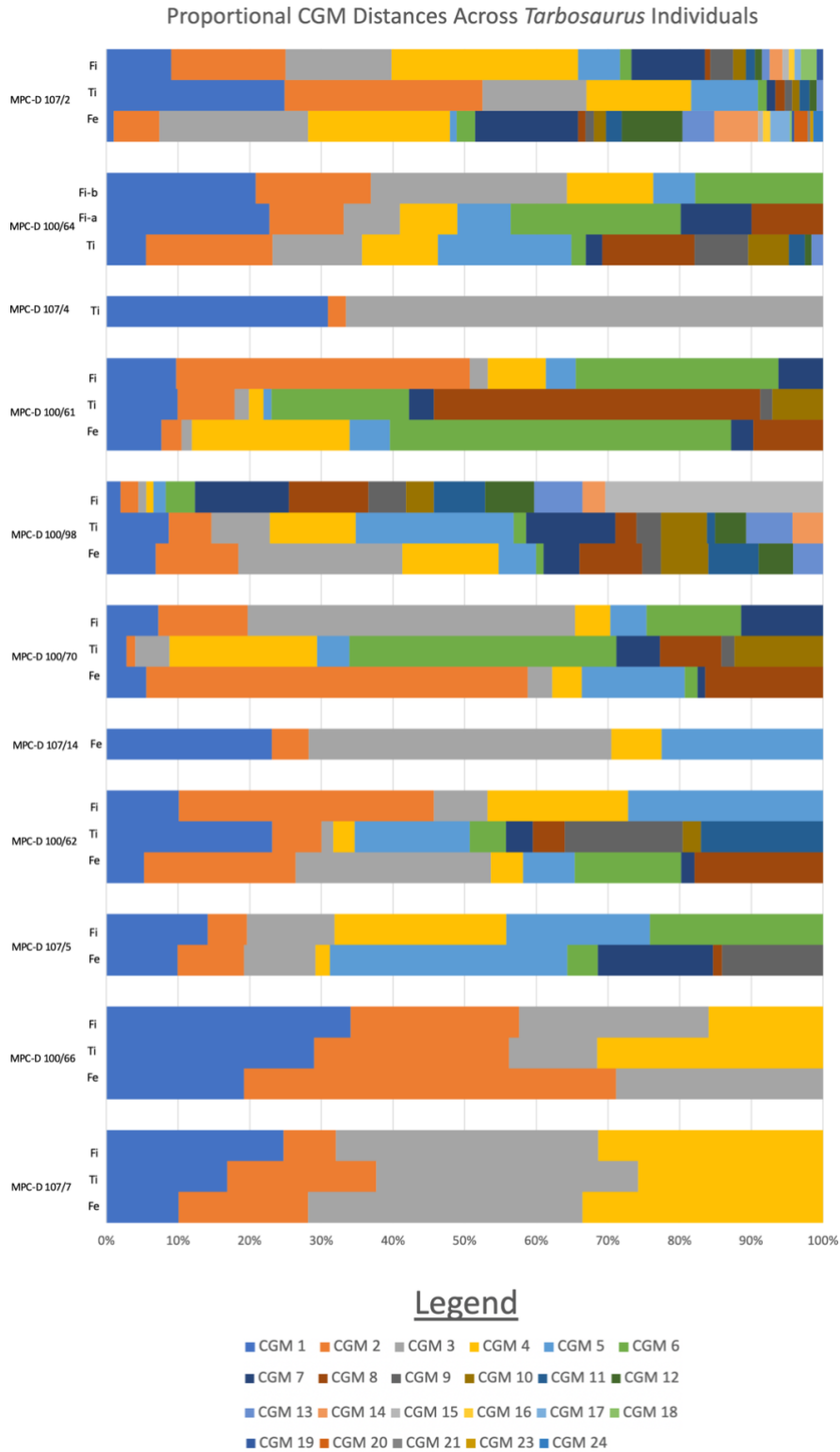


Figure 3.47. CGM distances proportional to the cortex depth within all elements. CGM distances correlate closely within the two smallest specimens, however the introduction of CGM couplets produce variable spacing across all elements.

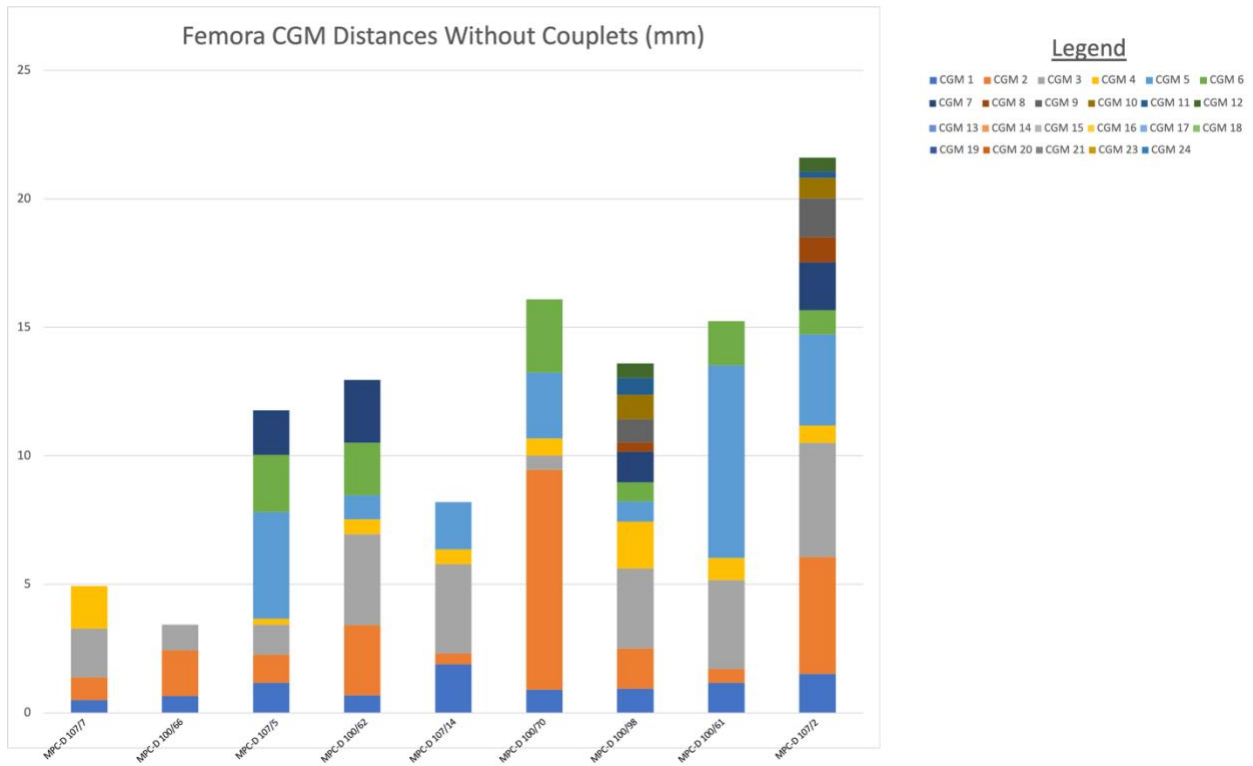


Figure 3.48. Histograms showing CGM distances throughout femora with couplet removed.

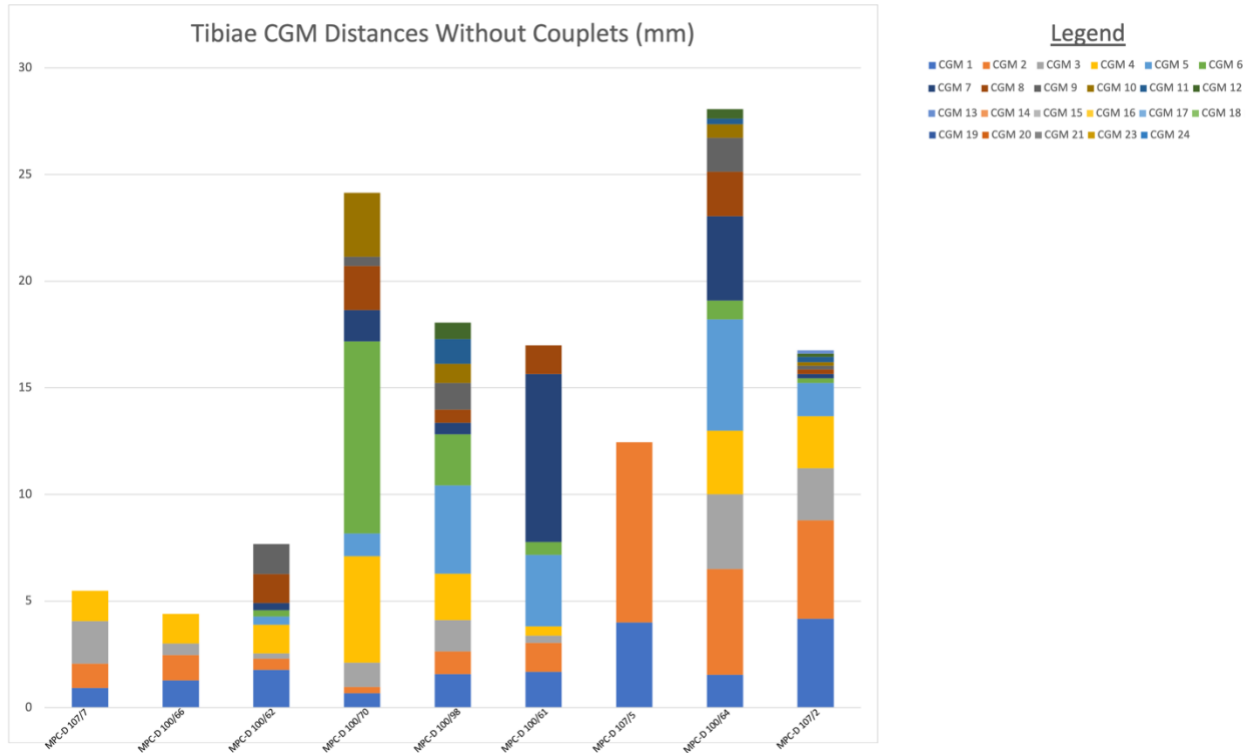


Figure 3.49. Histograms showing CGM distances throughout tibiae with couplets removed.

Proportional CGM Distances Across *Tarbosaurus*
Individuals Excluding Couplet

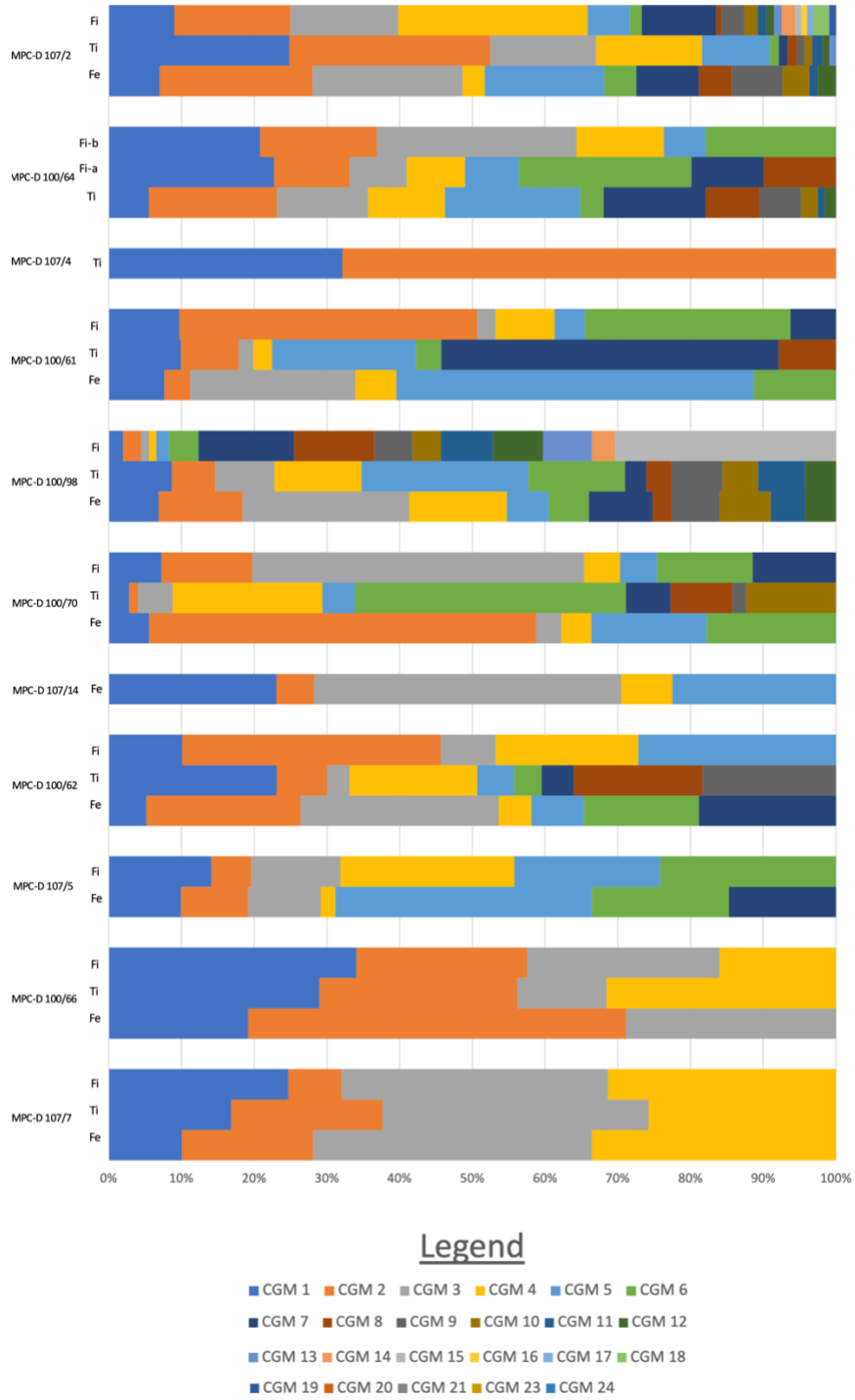


Figure 3.50. CGM distances proportional to the cortex depth within all elements with couplets removed. CGM distances correlate begin to correlate more accurately than when couplets are included in data.

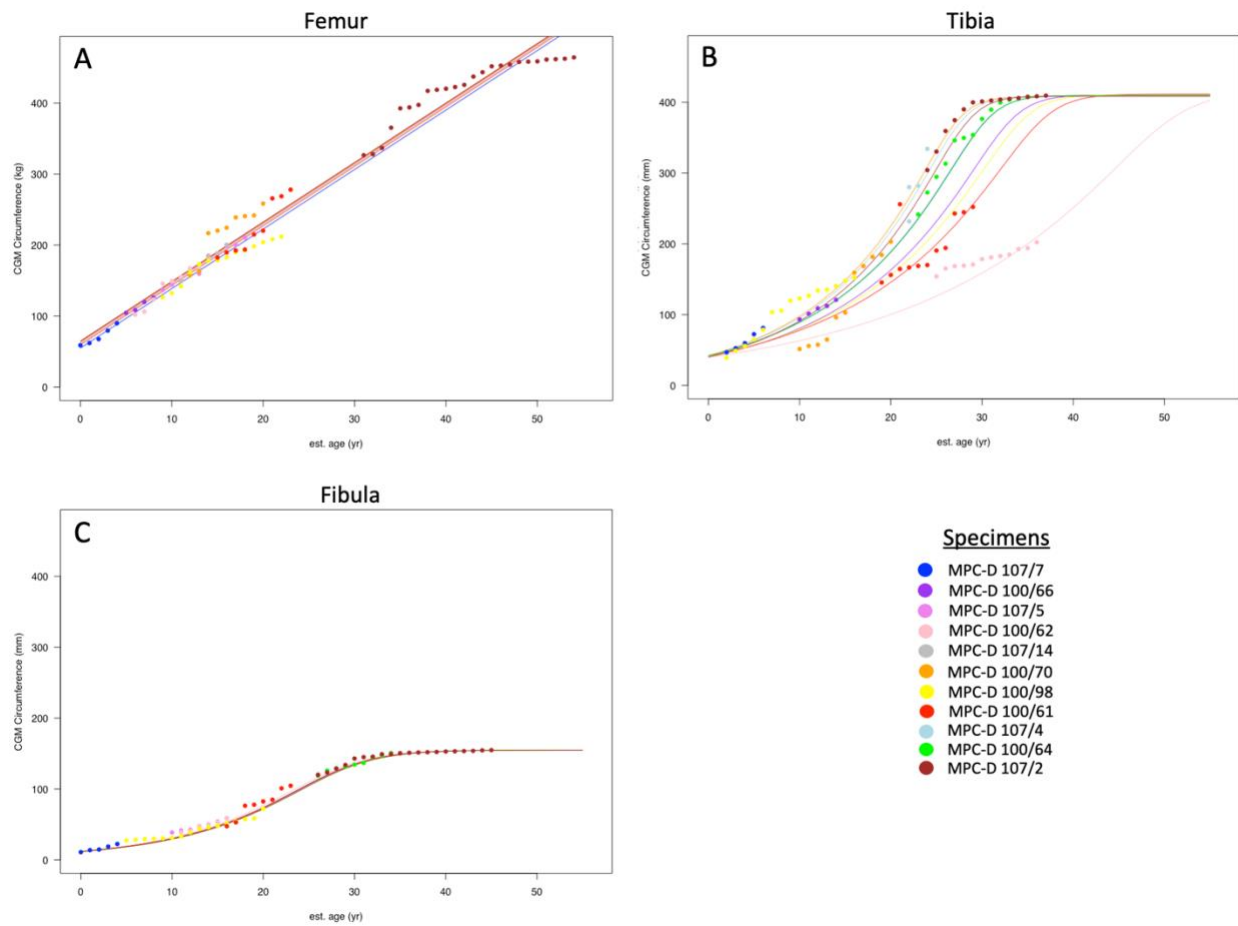


Figure 3.51. Growth model reconstructions using CGM circumferences. Femora grow using a linear model (A), tibiae grow using a Richards model (B), and fibulae grow using an EVF model (C).

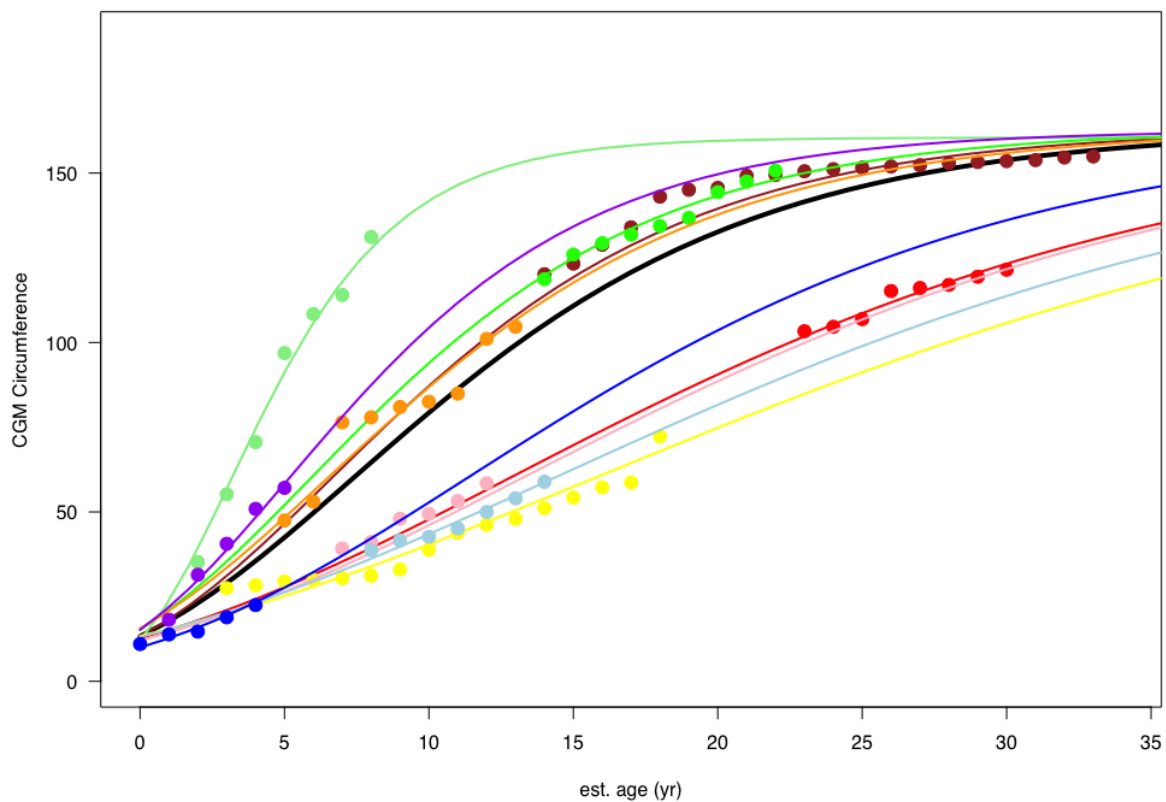


Figure 3.52. Growth model reconstruction of fibulae CGM circumferences including samples away from the mid-diaphysis. Green and light green models both correspond to MPC-D 100/64 but sampled at different locations on the fibula. Sample away from the mid-diaphysis has higher growth rate while sample closer to the mid-diaphysis has a lower growth rate.

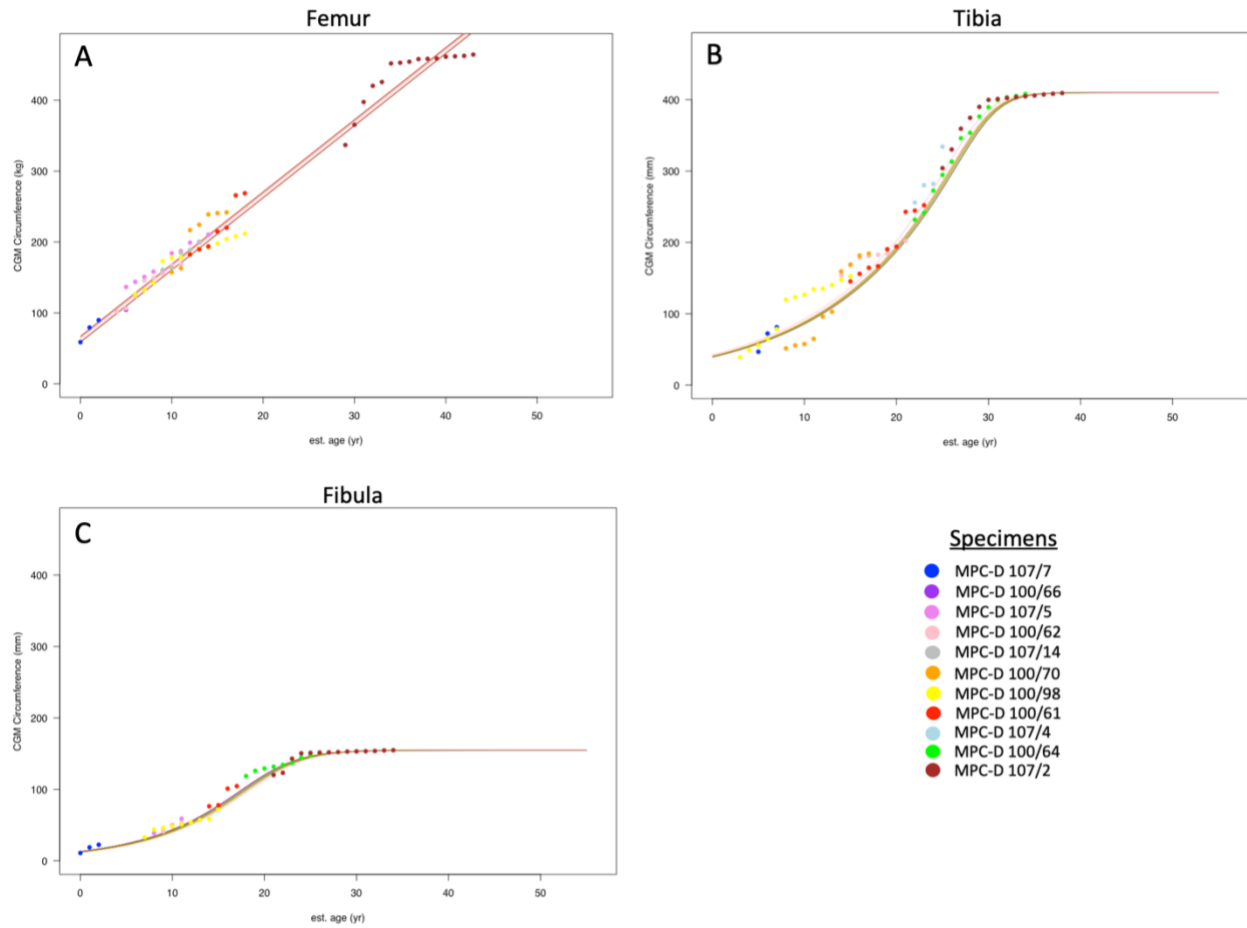


Figure 3.53. Growth model reconstructions using CGM circumferences with only LAGs modeled. Femora grow using a linear model (A), tibiae grow using a Richards model (B), and fibulae grow using an EVF model (C).

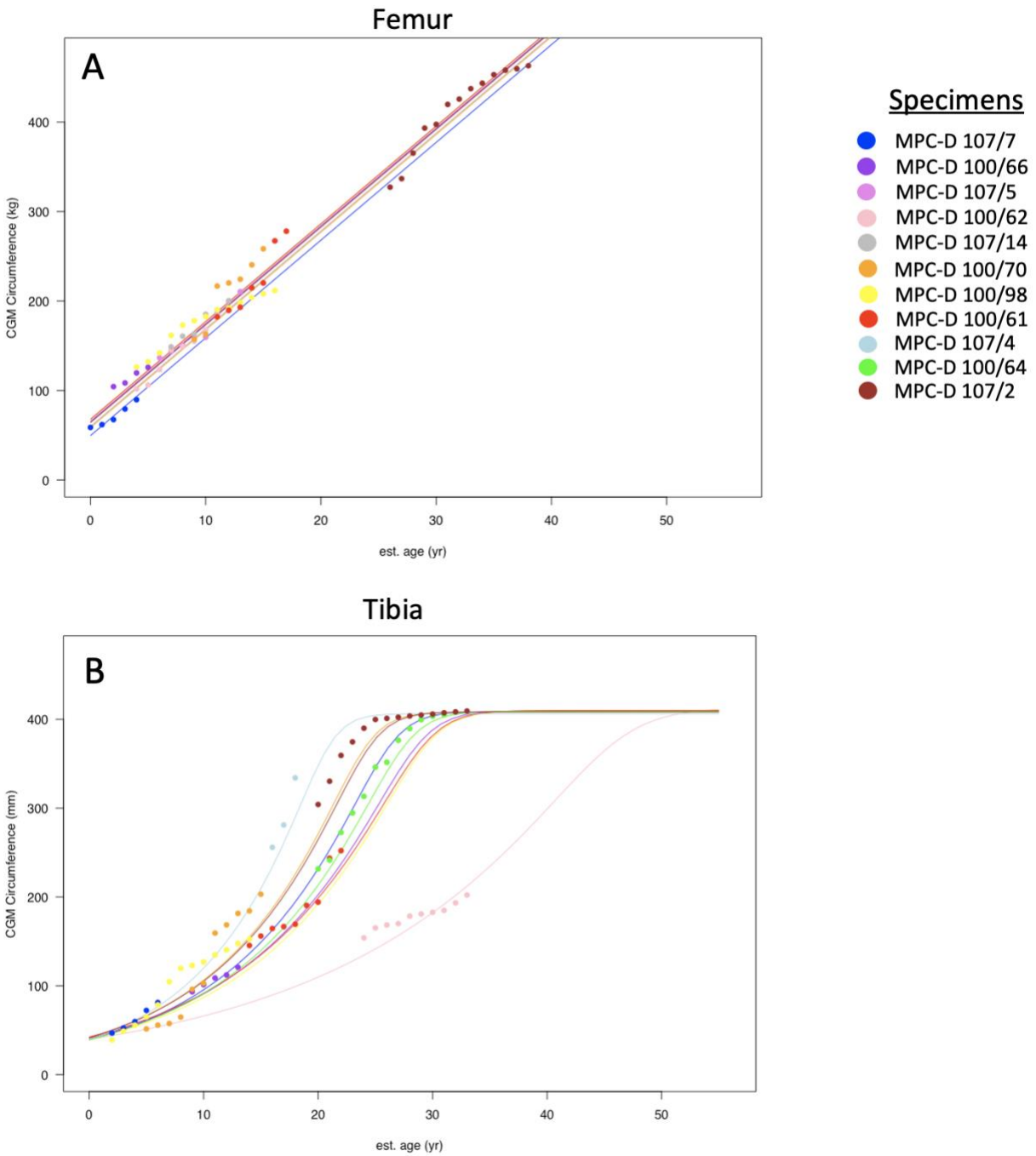


Figure 3.54. Growth model reconstructions using CGM circumferences with couplets averaged. Femora grow using a linear model (A) and tibiae grow using a Richards model (B).

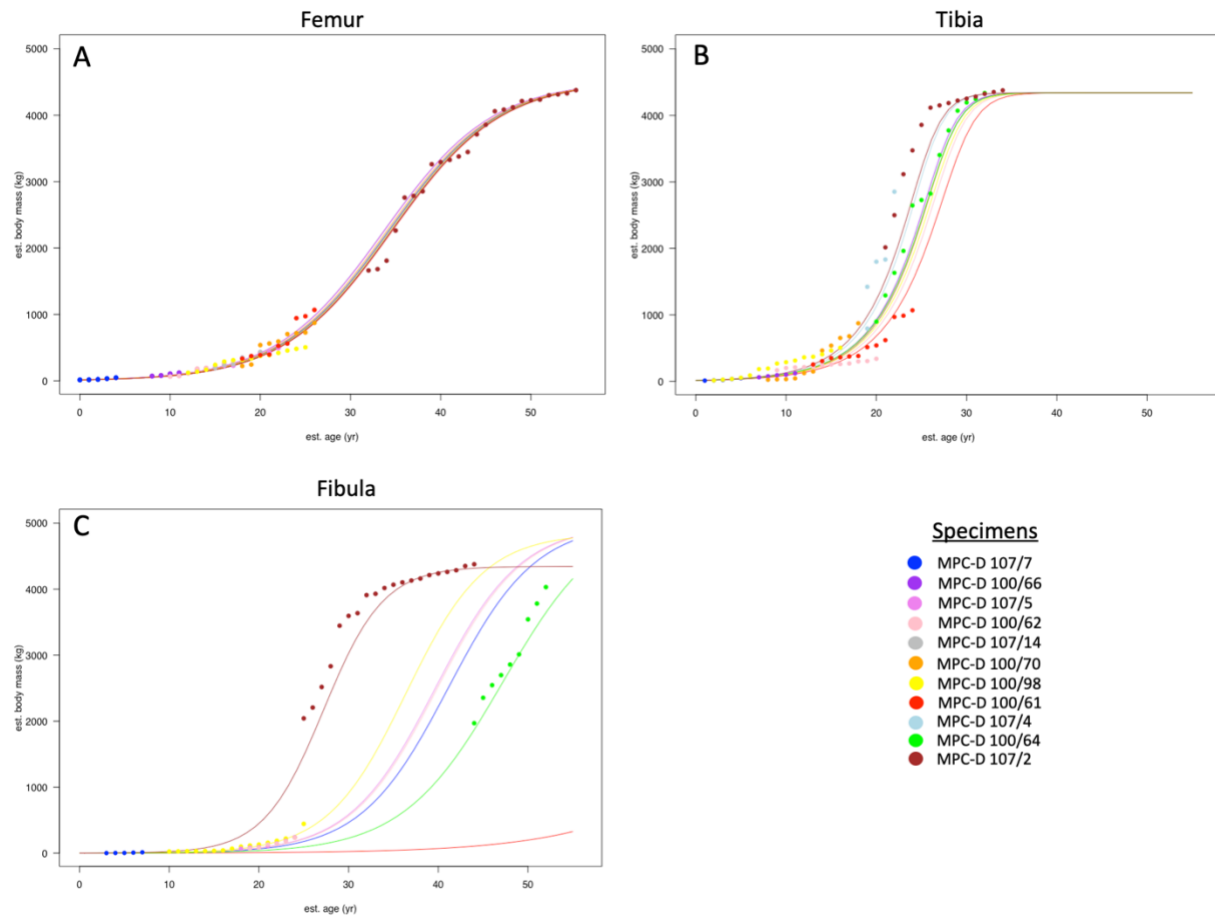


Figure 3.55. Growth model reconstructions using estimated body masses. Femora grow using a logistic model (A), tibiae grow using an EVF model (B), and fibulae grow using a logistic model (C).

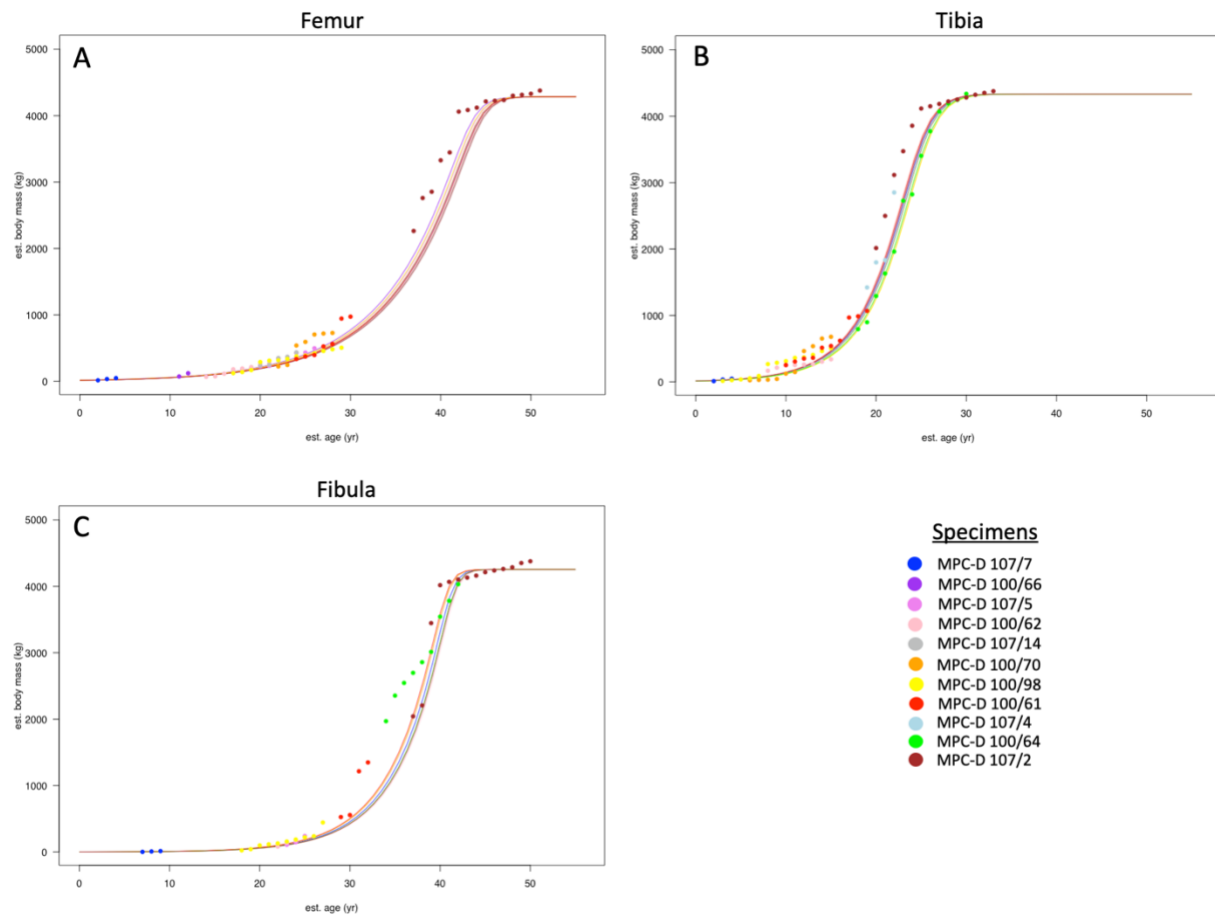


Figure 3.56. Growth model reconstructions using estimated body masses with only LAGs modeled. Femora grow using a Richards model (A), tibiae grow using an EVF model (B), and fibulae grow using an EVF model (C).

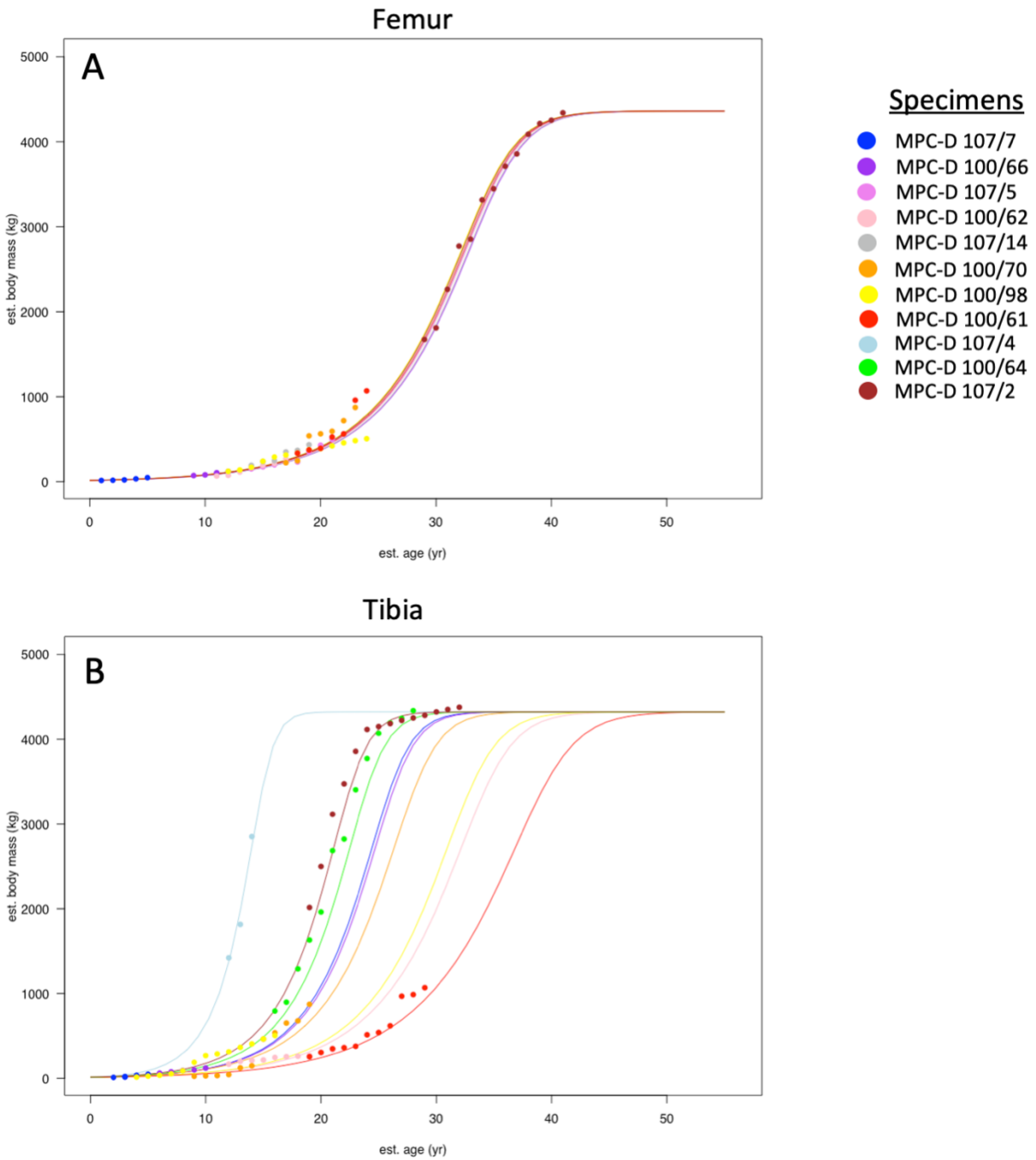


Figure 3.57. Growth model reconstructions using estimated body masses with couplets averaged. Femora grow using an EVF model (A) and tibiae grow using an EVF model (B).

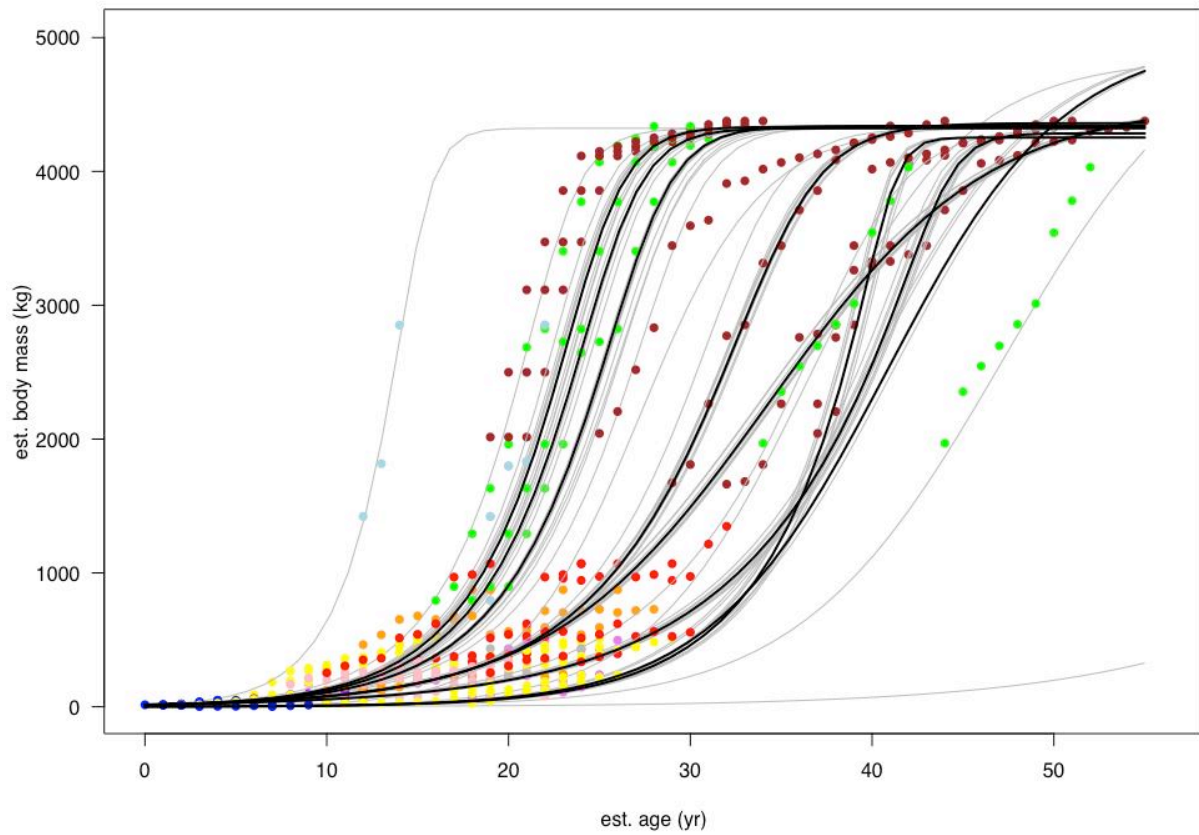


Figure 3.58. All possible body mass growth curve reconstructions based on figures 3.55 – 3.57. Grey lines are individual growth curves and black lines are model averages.

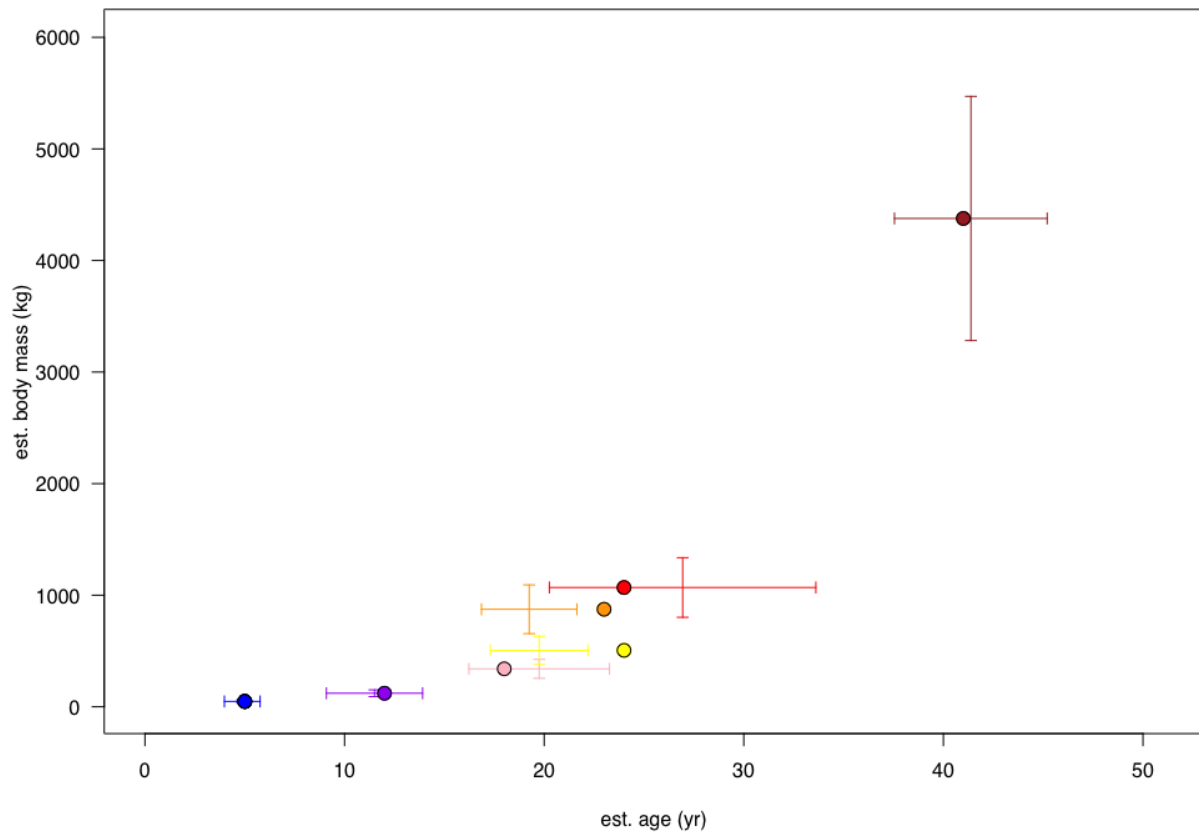


Figure 3.59. Body mass and age estimates with 95% confidence intervals. Age estimate is based on Table 3.7 "Best Estimate" and error bars are based on "Minimum" and "Maximum" 95% confidence interval estimates. Body mass error bars are $\pm 25\%$ estimated body mass (*sensu* Campione *et al.*, 2014). Only individuals with femur, tibia, and fibula are included.

TABLES

Table 3.1. Femur CGM circumferences

Specimen	Endosteal most CGM	CGM Circumference	Couplet Circumference	CGM Type
107/7	1	58.877		LAG
107/7	2	61.997		Annuli
107/7	3	67.597		Annuli
107/7	4	79.461		Double-LAG
107/7	5	89.854		LAG/Annuli
100/66	1	104.441		LAG
100/66	2	108.572		Annuli
100/66	3	119.768		Annuli
100/66	4	125.987		LAG
107/5	1	136.645		LAG
107/5	2	143.972		LAG
107/5	3	150.837		LAG
107/5	4	158.196		Double-LAG
107/5	5	159.685		Double-LAG
107/5	6	184.173	185.752	LAG
107/5	7	187.332		LAG
107/5	8	199.194	199.661	LAG
107/5	9	200.127		LAG
107/5	10	210.551		LAG
100/62	1	101.987		LAG
100/62	2	106.230		LAG
100/62	3	123.484		LAG
100/62	4	145.643		LAG
100/62	5	149.307		LAG
100/62	6	155.174		LAG
100/62	7	167.263	168.016	LAG
100/62	8	168.750		LAG
100/62	9	183.369		LAG
107/14	1	148.937		Annuli
107/14	2	160.824		LAG
107/14	3	163.484		Double-LAG
107/14	4	185.249		LAG
107/14	5	188.860		LAG
107/14	6	200.463		LAG
100/70	1	157.393		LAG

Table 3.1. Femur CGM circumferences (continued)

100/70	2	163.029		LAG
100/70	3	216.821		LAG
100/70	4	220.303		Annuli
100/70	5	224.472		LAG
100/70	6	238.968	240.540	LAG
100/70	7	240.793		LAG
100/70	8	241.861		LAG
100/70	9	258.478		Annuli
100/98	1	126.457		LAG
100/98	2	132.326		LAG
100/98	3	142.179		LAG
100/98	4	161.725		Annuli
100/98	5	173.200		LAG
100/98	6	177.651	178.104	LAG
100/98	7	178.556		LAG
100/98	8	182.818		LAG
100/98	9	190.305		LAG
100/98	10	192.530		Double-LAG
100/98	11	198.175		LAG
100/98	12	204.169		LAG
100/98	13	208.264		LAG
100/98	14	211.832		LAG
100/61	1	182.387		LAG
100/61	2	189.724		LAG
100/61	3	192.433	193.120	Annuli
100/61	4	193.806		LAG
100/61	5	214.859		LAG
100/61	6	220.239		LAG
100/61	7	265.839	267.330	LAG
100/61	8	268.821		LAG
100/61	9	278.122		Annuli
107/2	1	326.625	327.323	Annuli
107/2	2	328.022		Annuli
107/2	3	336.841		LAG
107/2	4	365.377		LAG
107/2	5	392.696	393.347	Annuli
107/2	6	393.999		Annuli
107/2	7	397.514		LAG

Table 3.1. Femur CGM circumferences (continued)

107/2	8	417.339	418.063	Annuli
107/2	9	418.787		Annuli
107/2	10	420.360	421.531	LAG
107/2	11	422.702		Annuli
107/2	12	425.729		LAG
107/2	13	437.412		Annuli
107/2	14	443.540		Annuli
107/2	15	451.912	453.042	EFS Boundary
107/2	16	452.903		EFS
107/2	17	454.310		EFS
107/2	18	458.055		EFS
107/2	19	458.474	459.602	EFS
107/2	20	458.883		EFS
107/2	21	461.448		EFS
107/2	22	461.970	463.003	EFS
107/2	23	462.603		EFS
107/2	24	464.435		EFS

Cells separated by dotted borders represent CGM couplets, triplets, quadruplets

Table 3.2. Tibia CGM circumferences

Specimen	Endosteal most CGM	CGM Circumference	Couplet Circumference	CGM Type
107/7	1	46.845		LAG
107/7	2	52.636		Annuli
107/7	3	59.802		Annuli
107/7	4	72.385		Double-LAG
107/7	5	81.257		LAG/Annuli
100/66	1	93.341		Annuli
100/66	2	101.330		Annuli
100/66	3	108.849		Annuli
100/66	4	112.236		Annuli
100/66	5	120.933		Annuli
100/62	1	154.064		Double-LAG
100/62	2	165.212		Annuli
100/62	3	168.544		Annuli
100/62	4	169.325	170.047	LAG
100/62	5	170.768		Annuli
100/62	6	178.508		LAG
100/62	7	180.951		LAG
100/62	8	182.764		LAG
100/62	9	184.913		LAG
100/62	10	192.842	193.453	Annuli
100/62	11	194.064		LAG
100/62	12	202.284		LAG
100/70	1	51.571		LAG
100/70	2	55.799		LAG
100/70	3	57.652		LAG
100/70	4	64.876		LAG
100/70	5	96.135		LAG
100/70	6	102.916		LAG
100/70	7	159.408		LAG
100/70	8	168.661		LAG/Annuli
100/70	9	181.621		LAG/Annuli
100/70	10	184.410		LAG/Annuli
100/70	11	203.139		Annuli
100/98	1	39.184		LAG
100/98	2	49.031		LAG
100/98	3	55.773		LAG

Table 3.2. Tibia CGM circumferences (continued)

100/98	4	65.021		LAG
100/98	5	78.618		LAG
100/98	6	103.652	104.613	Annuli
100/98	7	105.574		Annuli
100/98	8	119.705		LAG
100/98	9	123.036		Double-LAG
100/98	10	126.943		LAG
100/98	11	134.219	134.840	LAG
100/98	12	135.462		LAG
100/98	13	140.408		LAG/Annuli
100/98	14	147.731		LAG/Annuli
100/98	15	152.564		LAG/Annuli
100/61	1	145.485		LAG
100/61	2	156.070		LAG
100/61	3	164.556		LAG
100/61	4	166.711		LAG
100/61	5	168.866	169.461	Annuli
100/61	6	170.056		Annuli
100/61	7	190.525		LAG
100/61	8	194.261		LAG
100/61	9	242.864	243.768	LAG
100/61	10	244.672		LAG
100/61	11	252.189		LAG
107/4	1	255.995		LAG
107/4	2	280.151	281.138	LAG
107/4	3	282.124		LAG
107/4	4	334.182		LAG
100/64	1	231.787		LAG
100/64	2	241.513		LAG
100/64	3	272.647		LAG
100/64	4	294.665		LAG
100/64	5	313.314		LAG
100/64	6	346.129		LAG
100/64	7	349.677	351.706	Annuli
100/64	8	353.735		LAG
100/64	9	376.478		LAG
100/64	10	389.634		LAG
100/64	11	399.599		LAG

Table 3.2. Tibia CGM circumferences (continued)

100/64	12	403.598		LAG
100/64	13	405.276		LAG
100/64	14	408.041		Double-LAG
107/2	1	304.185		LAG
107/2	2	330.339		LAG
107/2	3	359.408		LAG
107/2	4	374.695		LAG
107/2	5	390.040		LAG
107/2	6	399.871		EFS Boundary
107/2	7	401.141		EFS
107/2	8	402.434		EFS
107/2	9	403.799		EFS
107/2	10	404.870		EFS
107/2	11	405.979		EFS
107/2	12	407.455		EFS
107/2	13	408.481		EFS
107/2	14	409.407		EFS

Cells separated by dotted borders represent CGM couplets, triplets, quadruplets

Table 3.3. Fibula CGM circumferences

Specimen	Endosteal most CGM	CGM Circumference	CGM Type
107/7	1	11.003	LAG
107/7	2	13.845	Annuli
107/7	3	14.684	Annuli
107/7	4	18.898	LAG
107/7	5	22.504	LAG
100/66	1	18.182	Annuli
100/66	2	31.443	Annuli
100/66	3	40.593	LAG
100/66	4	50.894	LAG
100/66	5	57.111	Annuli
107/5	1	38.7	LAG
107/5	2	41.554	Annuli
107/5	3	42.661	Annuli
107/5	4	45.135	LAG
107/5	5	49.975	LAG
107/5	6	54.022	Annuli
107/5	7	58.904	LAG
100/62	1	39.181	Annuli
100/62	2	41.127	LAG
100/62	3	47.975	Annuli
100/62	4	49.423	LAG
100/62	5	53.198	LAG
100/62	6	58.430	Annuli
100/98	1	27.471	Annuli
100/98	2	28.358	Annuli
100/98	3	29.468	Annuli
100/98	4	29.959	Annuli
100/98	5	30.398	Annuli
100/98	6	31.180	Annuli
100/98	7	33.009	LAG
100/98	8	38.870	Annuli
100/98	9	43.846	LAG
100/98	10	46.199	LAG
100/98	11	47.939	LAG
100/98	12	51.137	Double-LAG
100/98	13	54.209	LAG

Table 3.3. Fibula CGM circumferences (continued)

100/98	14	57.231	LAG
100/98	15	58.659	LAG
100/98	16	72.26	LAG
100/61	1	47.470	Annuli
100/61	2	53.031	Annuli
100/61	3	76.439	LAG
100/61	4	77.898	LAG
100/61	5	82.515	Annuli
100/61	6	84.898	Annuli
100/61	7	101.064	Double-LAG
100/61	8	104.625	LAG
100/70	1	103.319	LAG
100/70	2	104.637	Annuli
100/70	3	106.902	LAG
100/70	4	115.193	LAG
100/70	5	116.089	Annuli
100/70	6	117.011	Annuli
100/70	7	119.402	Annuli
100/70	8	121.479	LAG
100/64a	1	118.699	LAG
100/64a	2	125.975	LAG
100/64a	3	129.303	LAG
100/64a	4	131.818	LAG
100/64a	5	134.384	LAG
100/64a	6	136.759	LAG
100/64a	7	144.358	LAG
100/64a	8	147.531	LAG
100/64a	9	150.714	LAG
100/64b	1	35.206	LAG
100/64b	2	55.178	Annuli
100/64b	3	70.598	LAG
100/64b	4	96.884	Annuli
100/64b	5	108.410	LAG
100/64b	6	114.013	Annuli
100/64b	7	131.129	LAG
107/2	1	120.147	LAG
107/2	2	123.281	LAG
107/2	3	128.829	Annuli

Table 3.3. Fibula CGM circumferences (continued)

107/2	4	133.985	Annuli
107/2	5	143.035	Quad LAG
107/2	6	145.063	Annuli
107/2	7	145.621	Annuli
107/2	8	149.185	Annuli
107/2	9	149.436	Annuli
107/2	10	150.542	EFS Boundary
107/2	11	151.160	EFS
107/2	12	151.600	EFS
107/2	13	151.946	EFS
107/2	14	152.313	EFS
107/2	15	152.941	EFS
107/2	16	153.245	EFS
107/2	17	153.527	EFS
107/2	18	153.827	EFS
107/2	19	154.591	EFS
107/2	20	154.905	EFS

Table 3.4. Model Parameters

Femur Circumference (Model: Linear)										
SRE	9.429									
Parameter	Model Average	MPC-D 107/7	MPC-D 100/66	MPC-D 107/5	MPC-D 100/62	MPC-D 107/14	MPC-D 100/98	MPC-D 100/70	MPC-D 100/61	MPC-D 107/2
Color	Black	Blue	Purple	Violet	Pink	Grey	Yellow	Orange	Red	Brown
A	N/A	N/A	N/A	N/A	N/A	N/A	N/A	N/A	N/A	N/A
K	8.387	8.387	8.387	8.387	8.387	8.387	8.387	8.387	8.387	8.387
I	N/A	N/A	N/A	N/A	N/A	N/A	N/A	N/A	N/A	N/A
A0	60.867	54.8	60.2	59.8	60.7	61.4	58.6	63.9	63.5	64.9
Age	N/A	4	8	18	14	16	22	20	23	54
Sexual Maturity	34*	34*	34*	34*	34*	34*	34*	34*	34*	34
Skeletal Maturity	45*	45*	45*	45*	45*	45*	45*	45*	45*	45
RGR	8.387	8.387	8.387	8.387	8.387	8.387	8.387	8.387	8.387	8.387

Femur Body Mass (Model: Logistics)										
SRE	86.862									
Parameter	Model Average	MPC-D 107/7	MPC-D 100/66	MPC-D 107/5	MPC-D 100/62	MPC-D 107/14	MPC-D 100/98	MPC-D 100/70	MPC-D 100/61	MPC-D 107/2
Color	Black	Blue	Purple	Violet	Pink	Grey	Yellow	Orange	Red	Brown
A	4519.224	4519.224	4519.224	4519.224	4519.224	4519.224	4519.224	4519.224	4519.224	4519.224
K	0.166	0.166	0.166	0.166	0.166	0.166	0.166	0.166	0.166	0.166
I	34.261	34.256	33.721	33.758	34.543	34.54259	34.060	34.377	34.627	34.543
A0	15.08889	15.1	16.5	16.4	14.4	14.4	15.6	14.8	14.2	14.4
Age	N/A	4	11	22	18	20	26	25	26	55
Sexual Maturity	40.866	40.861	40.326	40.363	41.147	41.147	40.665	40.982	41.232	41.147

Table 3.4. Model Parameters (continued)

Skeletal Maturity	51.962	51.958	51.423	51.460	52.244	52.244	51.762	52.079	52.329	52.244
RGR	0.0832	0.0832	0.0832	0.0832	0.0832	0.0832	0.0832	0.0832	0.0832	0.0832

Tibia Circumference (Model: Richards)										
SRE	10.592									
Parameter	Model Average	MPC-D 107/7	MPC-D 100/66	MPC-D 100/62	MPC-D 100/98	MPC-D 100/70	MPC-D 100/61	MPC-D 107/4	MPC-D 100/64	MPC-D 107/2
Color	Black	Blue	Purple	Pink	Yellow	Orange	Red	Light Blue	Green	Brown
A	410.201	409.687	410.371	414.185	408.343	410.839	411.576	408.514	409.683	408.613
K	0.530	0.554	0.522	0.341	0.618	0.500	0.465	0.610	0.555	0.605
I	28.330	26.727	29.243	44.926	23.873	30.340	32.225	24.340	26.782	25.037
A0	41.144	42.2	39.8	39.9	42.4	40.4	41.5	41.9	42	40.2
Age	N/A	6	14	36	16	20	29	24	35	37
Sexual Maturity	28.328	26.726	29.242	44.924	23.872	30.338	32.224	24.339	26.781	25.035
Skeletal Maturity	33.564	31.731	34.558	53.066	28.361	35.891	38.195	28.887	31.785	29.619
RGR	0.0631	0.0660	0.0621	0.0406	0.0736	0.0595	0.0553	0.0726	0.0660	0.0721

Tibia Body Mass (Model: EVF)										
SRE	123.008									
Parameter	Model Average	MPC-D 107/7	MPC-D 100/66	MPC-D 100/62	MPC-D 100/98	MPC-D 100/70	MPC-D 100/61	MPC-D 107/4	MPC-D 100/64	MPC-D 107/2
Color	Black	Blue	Purple	Pink	Yellow	Orange	Red	Light Blue	Green	Brown
A	4338.640	4338.64	4338.64	4338.64	4338.64	4338.64	4338.64	4338.641	4338.64	4338.641
K	0.643	0.643	0.642	0.631	0.638	0.630	0.608	0.686	0.629	0.676
I	25.606	25.748	25.495	26.441	25.765	26.106	27.337	24.275	25.700	23.959
A0	12.478	12.1	12.8	11.6	12.5	12.5	11.8	11.7	13.7	13.6

Table 3.4. Model Parameters (continued)

Age	N/A	5	11	20	16	18	24	22	32	34
Sexual Maturity	26.826	26.968	26.715	27.683	26.992	27.349	28.626	25.418	26.945	25.118
Skeletal Maturity	30.107	30.249	29.997	31.027	30.294	30.696	32.094	28.492	30.295	28.237
RGR	0.161	0.161	0.161	0.158	0.160	0.158	0.152	0.171	0.157	0.169

Fibula Circumference (Model: EVF)								
SRE	3.437							
Parameter	Model Average	MPC-D 107/7	MPC-D 107/5	MPC-D 100/62	MPC-D 100/98	MPC-D 100/61	MPC-D 100/64a	MPC-D 107/2
Color	Black	Blue	Light Blue	Pink	Yellow	Red	Green	Brown
A	154.999	154.999	154.999	154.999	154.999	154.999	154.999	154.999
K	0.279	0.279	0.279	0.279	0.279	0.279	0.279	0.279
I	23.720	23.681	23.863	23.151	23.863	23.591	23.956	23.956
A0	11.857	11.9	11.7	12.5	11.7	12	11.6	11.6
Age	N/A	4	16	16	20	23	34	45
Sexual Maturity	26.530	26.491	26.674	25.962	26.674	26.401	26.766	26.766
Skeletal Maturity	34.094	34.056	34.238	33.526	34.238	33.966	34.330	34.330
RGR	0.0697	0.0697	0.0697	0.0697	0.0697	0.0697	0.0697	0.0697

Fibula Body Mass (Model: Logistic)								
SRE	92.896							
Parameter	Average	MPC-D 107/7	MPC-D 107/5	MPC-D 100/62	MPC-D 100/98	MPC-D 100/61	MPC-D 100/64a	MPC-D 107/2
Color	Black	Blue	Light Blue	Pink	Yellow	Red	Green	Brown
A	5007.732	5007.356	4979.044	4979.238	4842.165	5710.098	5191.192	4345.031
K	0.205	0.205	0.209	0.209	0.229	0.105	0.179	0.300
I	40.797	41.117	39.638	39.840	36.396	81.598	47.215	27.219
A0	1.156	1.08	1.24	1.19	1.17	1.06	1.1	1.25
Age	N/A	7	24	24	25	75	52	44
Sexual Maturity	46.150	46.468	44.886	45.089	41.197	92.032	53.347	30.886
Skeletal Maturity	55.143	55.458	53.704	53.908	49.264	109.562	63.649	37.0484

RGR	0.103	0.103	0.105	0.105	0.114	0.0526	0.0896	0.150
-----	-------	-------	-------	-------	-------	--------	--------	-------

Table 3.5. Couplet Subsampled Model Parameters

Femur Circumference (Model: Linear)										
SRE	9.978									
Parameter	Model Average	MPC-D 107/7	MPC-D 100/66	MPC-D 107/5	MPC-D 100/62	MPC-D 107/14	MPC-D 100/98	MPC-D 100/70	MPC-D 100/61	MPC-D 107/2
Color	Black	Blue	Purple	Violet	Pink	Grey	Yellow	Orange	Red	Brown
A	N/A	N/A	N/A	N/A	N/A	N/A	N/A	N/A	N/A	N/A
K	10.923	10.923	10.923	10.923	10.923	10.923	10.923	10.923	10.923	10.923
I	N/A	N/A	N/A	N/A	N/A	N/A	N/A	N/A	N/A	N/A
A0	62	49.7	65.5	64.4	59.7	60	58.6	67.9	67.9	64.3
Age	N/A	4	5	13	11	12	16	15	17	38
Sexual Maturity	31*	31*	31*	31*	31*	31*	31*	31*	31*	31*
Skeletal Maturity	35*	35*	35*	35*	35*	35*	35*	35*	35*	35*
RGR	10.923	10.923	10.923	10.923	10.923	10.923	10.923	10.923	10.923	10.923

Femur Body Mass (Model: EVF)										
SRE	81.261									
Parameter	Model Average	MPC-D 107/7	MPC-D 100/66	MPC-D 107/5	MPC-D 100/62	MPC-D 107/14	MPC-D 100/98	MPC-D 100/70	MPC-D 100/61	MPC-D 107/2
Color	Black	Blue	Purple	Violet	Pink	Grey	Yellow	Orange	Red	Brown
A	4360.285	4360.285	4360.285	4360.285	4360.285	4360.285	4360.285	4360.285	4360.285	4360.285
K	0.486	0.486	0.486	0.486	0.486	0.486	0.486	0.486	0.486	0.486
I	32.582	32.640	32.974	32.640	32.681	32.889	32.286	32.286	32.520	32.363
A0	15.344	15.2	14.4	15.2	15.1	14.6	16.1	16.1	15.5	15.9
Age	N/A	5	12	21	18	19	24	23	24	41
Sexual Maturity	34.193	34.251	34.585	34.251	34.292	34.499	33.896	33.896	34.131	33.973
Skeletal Maturity	38.528	38.586	38.919	38.586	38.627	38.834	38.231	38.231	38.465	38.308
RGR	0.122	0.122	0.122	0.122	0.122	0.122	0.122	0.122	0.122	0.122

Table 3.5. Couplet Subsampled Model Parameters (continued)

Tibia Circumference (Model: Richards m8.4)										
SRE	10.296									
Parameter	Model Average	MPC-D 107/7	MPC-D 100/66	MPC-D 100/62	MPC-D 100/98	MPC-D 100/70	MPC-D 100/61	MPC-D 107/4	MPC-D 100/64	MPC-D 107/2
Color	Black	Blue	Purple	Pink	Yellow	Orange	Red	Light Blue	Green	Brown
A	409.325	408.831	409.815	413.073	408.226	409.903	410.109	406.276	409.286	408.404
K	0.625	0.657	0.592	0.376	0.698	0.586	0.573	0.827	0.627	0.686
I	24.244	23.317	25.426	40.775	21.407	26.154	25.866	18.499	24.485	21.703
A0	40.356	39.3	40.9	39.8	41.4	39.4	42.3	39.2	39.2	41.7
Age	N/A	6	13	33	14	15	22	18	32	33
Sexual Maturity	24.243	23.316	25.425	40.773	21.406	26.153	25.864	18.498	24.484	21.702
Skeletal Maturity	28.686	27.537	30.113	48.163	25.384	30.888	30.712	21.853	28.909	25.749
RGR	0.0744	0.0783	0.0705	0.0447	0.0830	0.0698	0.0682	0.0985	0.0747	0.0816

Tibia Body Mass (Model: EVF)										
SRE	104.381									
Parameter	Model Average	MPC-D 107/7	MPC-D 100/66	MPC-D 100/62	MPC-D 100/98	MPC-D 100/70	MPC-D 100/61	MPC-D 107/4	MPC-D 100/64	MPC-D 107/2
Color	Black	Blue	Purple	Pink	Yellow	Orange	Red	Light Blue	Green	Brown
A	4322.222	4322.222	4322.222	4322.222	4322.222	4322.222	4322.222	4322.222	4322.222	4322.222
K	0.681	0.682	0.674	0.515	0.611	0.538	0.447	1.169	0.726	0.766
I	24.137	24.435	24.719	32.178	26.348	30.965	36.853	13.983	22.504	21.108
A0	12.522	11.6	11.6	12	14	11.6	12.4	12.9	12.9	13.7
Age	N/A	5	10	21	16	19	29	14	28	32
Sexual Maturity	25.288	25.584	25.881	33.701	27.630	32.421	38.607	14.654	23.583	22.131
Skeletal Maturity	28.386	28.676	29.009	37.798	31.082	36.340	43.327	16.458	26.486	24.885
RGR	0.170	0.170	0.169	0.129	0.153	0.135	0.112	0.292	0.182	0.191

Table 3.6. Annuli Subsampled Model Parameters

Femur Circumference (Model: Linear)										
SRE	11.207									
Parameter	Model Average	MPC-D 107/7	MPC-D 100/66	MPC-D 107/5	MPC-D 100/62	MPC-D 107/14	MPC-D 100/98	MPC-D 100/70	MPC-D 100/61	MPC-D 107/2
Color	Black	Blue	Purple	Violet	Pink	Grey	Yellow	Orange	Red	Brown
A	N/A	N/A	N/A	N/A	N/A	N/A	N/A	N/A	N/A	N/A
K	10.183	10.183	10.183	10.183	10.183	10.183	10.183	10.183	10.183	10.183
I	N/A	N/A	N/A	N/A	N/A	N/A	N/A	N/A	N/A	N/A
A0	63.656	65.9	59.2	66.2	63.1	67.8	59.2	66.3	66.6	58.6
Age	N/A	2	6	14	12	13	18	16	18	43
Sexual Maturity										
Skeletal Maturity										
RGR	10.183	10.183	10.183	10.183	10.183	10.183	10.183	10.183	10.183	10.183

Femur Body Mass (Model: Richardsm8.4)										
SRE	91.696									
Parameter	Model Average	MPC-D 107/7	MPC-D 100/66	MPC-D 107/5	MPC-D 100/62	MPC-D 107/14	MPC-D 100/98	MPC-D 100/70	MPC-D 100/61	MPC-D 107/2
Color	Black	Blue	Purple	Violet	Pink	Grey	Yellow	Orange	Red	Brown
A	4284.233	4284.233	4284.233	4284.233	4284.233	4284.233	4284.233	4284.233	4284.233	4284.233
K	0.946	0.946	0.946	0.946	0.946	0.946	0.946	0.946	0.946	0.946
I	41.899	41.955	41.270	41.654	42.215	42.215	41.904	41.557	42.058	42.321
A0	15.411	15.3	16.7	15.9	14.8	14.8	15.4	16.1	15.1	14.6
Age	N/A	4	12	26	22	24	29	28	30	51
Sexual Maturity	41.898	41.954	41.270	41.654	42.214	42.214	41.904	41.556	42.057	42.321
Skeletal Maturity	44.831	44.888	44.203	44.587	45.147	45.147	44.837	44.489	44.990	45.254
RGR	0.113	0.113	0.113	0.113	0.113	0.113	0.113	0.113	0.113	0.113

Table 3.6. Annuli Subsampled Model Parameters (continued)

Tibia Circumference (Model: Richards m8.4)									
SRE	12.270								
Parameter	Model Average	MPC-D 107/7	MPC-D 100/62	MPC-D 100/98	MPC-D 100/70	MPC-D 100/61	MPC-D 107/4	MPC-D 100/64	MPC-D 107/2
Color	Black	Blue	Pink	Yellow	Orange	Red	Light Blue	Green	Brown
A	410.077	410.077	410.077	410.077	410.077	410.077	410.077	410.077	410.077
K	0.579	0.579	0.579	0.579	0.579	0.579	0.579	0.579	0.579
I	26.191	26.073	25.550	26.136	26.104	26.263	26.455	26.423	26.553
A0	40.325	40.7	42.4	40.5	40.6	40.1	39.5	39.6	39.2
Age	N/A	7	21	15	17	23	25	34	38
Sexual Maturity	26.190	26.072	25.548	26.134	26.103	26.261	26.454	26.422	26.552
Skeletal Maturity	30.984	30.865	30.342	30.928	30.897	31.055	31.248	31.216	31.345
RGR	0.0689	0.0689	0.0689	0.0689	0.0689	0.0689	0.0689	0.0689	0.0689

Tibia Body Mass (Model: EVF)									
SRE	132.718								
Parameter	Model Average	MPC-D 107/7	MPC-D 100/62	MPC-D 100/98	MPC-D 100/70	MPC-D 100/61	MPC-D 107/4	MPC-D 100/64	MPC-D 107/2
Color	Black	Blue	Pink	Yellow	Orange	Red	Light Blue	Green	Brown
A	4333.399	4333.399	4333.399	4333.399	4333.399	4333.399	4333.399	4333.399	4333.399
K	0.705	0.705	0.705	0.705	0.705	0.705	0.705	0.705	0.705
I	23.269	23.105	23.041	23.692	23.729	22.885	23.236	23.546	23.009
A0	12.7	13.2	13.4	11.5	11.4	13.9	12.8	11.9	13.5
Age	N/A	4	15	15	15	19	22	30	33
Sexual Maturity	24.381	24.217	24.153	24.804	24.841	23.997	24.348	24.658	24.121
Skeletal Maturity	27.373	27.209	27.145	27.796	27.833	26.989	27.340	27.650	27.113
RGR	0.176	0.176	0.176	0.176	0.176	0.176	0.176	0.176	0.176

Table 3.6. Annuli Subsampled Model Parameters (continued)

Fibulae No metaphysis LAGs N=7 EVF								
SRE	4.547							
Parameter	Average	MPC-D 107/7	MPC-D 107/5	MPC-D 100/62	MPC-D 100/98	MPC-D 100/61	MPC-D 100/64a	MPC-D 107/2
Color	Black	Blue	Light Blue	Pink	Yellow	Red	Green	Brown
A	155.021	155.021	155.021	155.021	155.021	155.021	155.021	155.021
K	0.364	0.364	0.364	0.364	0.364	0.364	0.364	0.364
I	17.708	17.349	18.141	17.605	18.072	17.412	17.605	17.802
A0	12.5428 6	13.1	11.9	12.7	12	13	12.7	12.4
Age	N/A	2	11	11	15	17	26	34
Sexual Maturity	19.861	19.502	20.294	19.758	20.225	19.565	19.758	19.955
Skeletal Maturity	25.655	25.297	26.089	25.552	26.02	25.360	25.552	25.750
RGR	0.0910	0.0910	0.0910	0.0910	0.0910	0.0910	0.0910	0.0910

Table 3.7. All Age Estimates Produced from Models for *Tarbosaurus* Individuals

Specimen	Original						Couplet Subsample				LAG Subsample					
	Femur		Tibia		Fibula		Femur		Tibia		Femur		Tibia		Fibula	
	C	BM	C	BM	C	BM	C	BM	C	BM	C	BM	C	BM	C	BM
107/7	4	4	6	5	4	7	4	5	6	5	2	4	7	4	2	9
100/66	8	11	14	11			5	12	13	10	6	12	21	15		
107/5	18	22			16	24	13	21			14	26			11	25
100/62	14	18	36	20	16	24	11	18	33	21	12	22	21	15	11	24
100/98	22	26	16	16	20	25	16	24	14	16	18	29	17	15	15	27
100/61	23	26	29	24	23	75	17	24	22	29	18	30	23	19	17	32
100/70	20	25	20	18			15	23	15	19	16	28	17	15		
100/64a			35	32	34	52			32	28			34	30	26	42
100/64b					8	8									3	
107/2	54	55	37	34	45	44	38	41	33	32	43	51	38	33	34	50
107/4			24	22												
107/14	16	20					12	19			13	24				

Table 3.8. Age Estimates and Confidence Intervals of *Tarbosaurus* Individuals

Specimen	Average (yr)	Minimum (yr)	Maximum (yr)	Best Estimate (yr)
MPC-D 107/7	4.88	3.98	5.77	5
MPC-D 100/66	11.5	9.09	13.91	12
MPC-D 107/5	19	15.68	22.32	21
MPC-D 100/62	19.75	16.23	23.27	18
MPC-D 107/14	17.33	13.70	20.97	19
MPC-D 100/70	19.25	16.86	21.64	23
MPC-D 100/98	19.75	17.31	22.19	24
MPC-D 100/61	26.94	20.26	33.61	24
MPC-D 107/4	23	22.31	23.69	14*
MPC-D 100/64	34.5	29.83	39.17	28*
MPC-D 107/2	41.38	37.55	45.20	41

Averages derived from all available age estimates from Table 3.7. Minimum and Maximum ages are 95% Confidence Intervals based on Table 3.7. Best Estimate is based on Femur Body Mass model with Couplets Subsampled

Chapter 4: Discussion

Histological Trends

Throughout the sample, the cortex is predominantly composed of fibrolamellar tissue. The cortex of the nine smallest individuals invariably consists of a woven bone matrix in all hind limb elements sampled. The cortex of the three largest individuals begins to transition from a woven matrix proximal to the endosteal region to a more parallel-fibered matrix centrifugally. Lamellar bone in the form of an EFS is only found near the periosteal surface in the largest specimen (MPC-D 107/2). This transition to parallel-fibered tissue is abrupt and only persists for what appears to be a few years. Only the most peripheral cortex of the largest individuals preserves a bone matrix type other than woven bone suggesting that rapid growth is maintained for the majority of *Tarbosaurus* ontogeny and growth slows rather quickly in late life.

Similarly, vascularity remains constant for most of the sample. Femora and tibiae of the nine smallest individuals have consistently high vascularity with plexiform morphology, whereas the fibula is mostly high vascularity with longitudinal and reticular canal morphology. The three largest specimens exhibit a decrease in vascularity and the morphology of these primary osteons begin to change. Femora and tibiae shift to longitudinal and laminar morphology, whereas the fibulae shift to strictly longitudinal morphology. These changes are as abrupt as the changes in bone matrix type and take place over the course of a few years.

Overall, osteocyte lacunae shape and density follow this trend across all elements. The nine smallest individuals have large round osteocyte lacunae. Osteocyte lacunae density appears to fluctuate regionally in medium to large size individuals. Osteocyte lacunae thickness decreases

consistent with the observed change in matrix type and vascularity in the three largest individuals.

The amount of secondary remodeling depends mostly on whether the limb bone is a weight bearing bone or a non-weight bearing bone. Femora and tibiae overall preserve fewer secondary osteons and less dense haversian tissue than fibulae. Even in MPC-D 107/7, there is a significant amount of dense haversian tissue obscuring the cortex of the fibula. This expansion of dense haversian continues through ontogeny until the cortex of mature individuals are almost entirely remodeled. Weight bearing bones, on the other hand, rarely have remodeling to the same degree. Secondary osteons are mostly contained to the innermost third of the cortex and rarely accumulate into dense haversian tissue. MPC-D 100/63 is the only specimen to have more remodeling than average. This might be attributable to microfractures brought on by stress and loading that are being repaired given the location on the element of this section (near a muscle attachment). However, more careful study of this feature is needed to determine a possible etiology. This trend in remodeling supports previous observations that weight bearing bones, such as femora and tibiae, are the optimal choice when describing the histology of gigantic species since the rate of growth is faster than the rate of remodeling (Cullen *et al.*, 2020b).

Growth Mark Variation

Growth marks are highly variable throughout this sample. The presence of either a LAG or an annulus appeared to have no correlation with limb element or CGM circumference size (Table 4.1). Additionally, CGM counts vary across all elements for nearly all individuals. MPC-D 107/7 is the only individual to have the same total number of CGMs across all limb bones sampled.

Similarly, the successive distance of CGMs is highly variable in all individuals except for MPC-D 107/7 and MPC-D 100/66 (Fig. 3.47). As for the other specimens, there appears to be no consistent pattern of increase in distance in CGM spacing as specimens get larger or even a decrease in distance as specimens attained skeletal maturity. Specimens larger than MPC-D 100/66 also are more likely to preserve CGM couplets, triplets, or even quadruplets (Fig. 4.1; Table 3.1; 3.2). Additionally, not all elements within an individual preserve the same amount of couplets at the same position within the growth record (Fig. 3.47; Table 3.1; 3.2). Some of these couplets, as seen in MPC-D 100/62 and MPC-D 100/61, preserve highly disorganized woven bone that likely points to growth spurts. All of these observations would suggest that *Tarbosaurus* would have extremely variable growth, even between different weight bearing bones, through an individual's lifetime.

Growth marks usually form on an annual cycle (Castanet, 2004), however more recent studies have concluded that growth lines can also be deposited as a result of seasonality or other stressful events that restrict bone growth (Köhler *et al.*, 2012; Nacarino-Meneses & Köhler, 2018). A growing body of literature has observed that growth mark spacing is variable among extinct species (Werning, 2012; Cullen *et al.*, 2014; Woodward *et al.*, 2020; Chapelle *et al.*, 2021) and even extant species when the age is already known (Woodward *et al.*, 2014; Heck & Woodward, 2021). It may be that these couplets are forming under stressful situations throughout the year rather than strictly representing annual periodicity and such events affect growth uniquely across different bones. This would explain why CGM counts are more consistent and successive CGM distances are less variable in the two youngest specimens; stressful events would be less likely to

occur early in life after hatching if tyrannosaurs exhibited parental care and/or lived in packs as previously hypothesized (Currie, 1998).

Paleopathologies

The pathology within MPC-D 100/70 appears to be a chronic growth within the medullary cavity. Because the histological sample only provides a small window into the cortex of this specimen, it is impossible to know the extent of this pathology in the cortex of this specimen and whether it was malignant in nature. The diagnosis of this pathology falls outside of the scope of this project and would require gross examination of the specimen as well as additional histological sampling to understand the extent and nature of this pathology.

MPC-D 100/63 is observed to have highly disorganized fibrolamellar bone in the femoral cortex and extensive secondary remodeling in the tibial cortex in an unusual radial pattern (Fig. 3.39). It is possible this remodeling is following microcracks in the bone tissue (i.e., fatigue fractures).

While fatigue fractures are common in the tibia of active extant animals due to their repeated use in running (Daffner & Pavlov, 1992), this is the first occurrence found in a tyrannosaur.

Paradoxically, weight bearing bones in tyrannosaurs are effective at reducing stress loading brought on by their gigantic sizes (Padian *et al.*, 2016; Cullen *et al.*, 2020b). Additionally, there is overwhelming evidence that tyrannosaurs are highly active predators (Depalma *et al.*, 2013; Rothschild *et al.*, 2001) that had limb bones optimized to reduce energy expenditure when traveling just below their top speed (Dececchi *et al.*, 2020). Therefore, if this remodeling is indicative of fatigue fractures it may offer interesting insight into this particular individual's life in the form of increased and repetitive loading during locomotion. However, additional study

focusing on this unusual remodeling pattern is needed to determine if this hypothesis is supported. Because osteoporosis is not observed within this specimen, old age and/or nutrient deficiency can be ruled out as potential causes for this remodeling.

Developmental Plasticity

These results support a hypothesis of developmental plasticity within the growth of *Tarbosaurus bataar* on several levels. First, variation in the successive distance between CGMs suggest that a single bone will grow at different rates throughout its entire growth span. From year to year, it can appear as there is no pattern in increase or decrease in the amount of tissue deposited between CGMs within a single hind limb element (Fig. 3.44; 3.45; 3.46). Couplets can obscure this pattern further as these features could be interpreted as an entire year of virtually no growth. Modeling of individual bone growth can reveal distinct trends in bone growth that may be otherwise obscured through annual variation (Fig. 3.51; 3.55). As shown by MPC-D 100/64, even the same bone preserves different growth records depending on where it is sampled (Fig. 3.52). Sampling further from the mid-diaphysis can result in significantly faster growth and earlier maturation. As shown by previous literature, the metaphysis remodels differently than the mid-diaphysis of a long bone and can produce a different record (Enlow, 1963). Given the lack of remodeling previously reported in the mid-diaphysis by other researchers (Enlow, 1963) together with the results of our modeling, I highly caution future workers to restrict sampling to the mid-diaphysis or account for the documented differences in growth models between data derived from the mid-diaphysis verses more proximal or distal locations.

Second, growth varies intraskeletally as each limb bone from an individual is best fit to a different model (Table 3.4). These separate models all estimate different growth rates, inflections in growth, time to maturation, and even ages of specimens. This is compounded when body mass is estimated from bone circumference data, which then creates more unique models of growth (Fig. 3.51; 3.55). However, body mass models from all three bones provide a holistic view of growth to compare against (Fig. 3.58). With a range of possible growth trajectories, a more informed estimate of an individual's growth can be determined (Fig. 3.59).

Finally, I observe interskeletal variation in growth, depending on which bone is sampled. For example, tibial circumference-based models exhibit high individual variation in model parameters, yet this variation decreases when circumferences are transformed to body mass estimates. Fibular data have the inverse problem, with highly variable body mass models and constrained circumference models. Femoral models are consistently constrained across both data types, even when subsampled. Averaging the growth of individuals is shown to be an effective way to account for outlier individuals and accurately understand the growth of the species.

These results also support the growing histological evidence that dinosaur growth is more plastic than previously realized (Cullen *et al.*, 2014; Prondvai *et al.*, 2017; Woodward *et al.*, 2020; Chappelle *et al.*, 2021). Developmental plasticity is most likely a basal trait of Saurischia (but possibly all of Dinosauria) as the degree of variation in annual growth seen in *Tarbosaurus* is very similar to that of the basal sauropodomorph, *Massospondylus*. Woodward *et al.* (2020) found that reported juvenile specimens of *Tyrannosaurus* exhibit variable growth likely the result of environmental stressors. Additionally, adult specimens were re-examined, and these

specimens were shown to have variable growth, suggesting that life histories should be revised for these specimens (Woodward *et al.*, 2020). Our large sample of *Tarbosaurus* supports the hypothesis that tyrannosaurids had variable growth throughout life. While this study cannot assess whether this variation is a direct result of environmental stressors, annual growth variation has been shown to be the result of stressful life events (Köhler *et al.*, 2012; Cullen *et al.*, 2014). Further testing on the seasonality of the Nemegt formation could lend support to environmental stressors as a cause.

Determining the Most Accurate Model

As mentioned previously, weight bearing bones are the optimal choice when reconstructing growth. The fibula becomes increasingly remodeled by dense haversian tissue with age and, as a result, the cortex preserves less growth marks. Weight bearing bones preserve more of the cortex and therefore preserve more CGMs and a longer span of time in the individual's life. However, the tibiae and femora data produce significantly different models for growth and can give contradicting age estimates (Table 3.7).

MPC-D 107/2 attained skeletal maturity throughout all bones and is the ideal specimen to compare age estimates with. Complete CGM datasets produce a wide gap in age ranges based on both bone circumference and body mass estimates; tibial data estimate around 30 years to skeletal maturity, fibular data estimate around 40 years, and femoral data estimate around 50 years. However, subsampled circumference models that treated couplets as a single growth period produce estimated ages in the 30's for all elements. Additionally, when these specific growth data are given the same terminal age, MPC-D 107/2's femoral and tibial CGMs in active

growth have nearly identical growth trajectories with the only difference being that the tibia stops growing five years before the femur does. Based on the lack of variation in age estimation for MPC-D 107/2, our results suggest that modeling couplets as a single CGM is the most accurate method. These results also suggest that the femur circumference is the ideal proxy for age estimation since it is the last bone to achieve skeletal maturity. It should be noted that these conclusions are based solely on MPC-D 107/2, therefore future histological work should be done on more *Tarbosaurus* specimens of similar size to confirm this.

Comparing MPC-D 107/2 to FMNH PR 2081

To understand the heterochronic changes in growth strategies from *Tarbosaurus* to *Tyrannosaurus*, MPC-D 107/2 was compared to the skeletally mature *Tyrannosaurus* specimen FMNH PR 2081. Because the growth record of *Tyrannosaurus* has significant gaps when using the methods of Lee & O'Connor (2013), the best fit non-linear parametric model (von Bertalanffy) was fitted to just these two specimens to accurately compare similar records of preserved growth. Both models are significantly different in asymptotic size and growth rate (Fig. 4.2). The growth rate is observed to be the biggest difference between the two individuals with FMNH PR 2081 having a growth rate 31% faster than that of MPC-D 107/2. These results support a hypothesis of peramorphic acceleration in tyrannosaurid growth rates that take place sometime before late diverging tyrannosaurines migrate to North America and after the divergence of crown tyrannosaurines.

An important point to note is that age estimates for MPC-D 107/2 are significantly younger when modeled individually and model shape differs as well. This is due to the exclusion of data from

skeletally immature specimens that display unique annual growth from what is modeled by MPC-D 107/2. Therefore, it is logical to assume that FMNH PR 2081 is also underestimated in age and model shape would likely change with the inclusion of smaller *Tyrannosaurus* specimens in growth curve reconstructions.

Limitations in Method

The model-fitting methods of Lee & O'Connor (2013) are shown to currently be the best way to reconstruct growth curves, however, there are inherent limitations for a method such as this that should be considered. Even though nearly all organisms grow in a sigmoidal pattern (Zullinger *et al.*, 1984), some non-amniotes have been recorded to exhibit more complex growth known as secondary metamorphosis where organisms have two inflections and two asymptotes in their life history (Dortel *et al.*, 2015; Zylstra & Steidl, 2020). Such growth has been hypothesized for *Tyrannosaurus* based on a suite of morphological changes taking place between reported juveniles and sub-adult specimens (Carr, 2020). While our data does not indicate secondary metamorphosis to be present in the life history of *Tarbosaurus*, which is the sister taxon to *Tyrannosaurus*, the methods used in this study do not have the capabilities to model such complex models for growth and therefore cannot directly test such a hypothesis.

Another apparent limitation to this method is that the accuracy of the results is dependent on how complete and continuous the growth data is between specimens. Fitting non-linear models to data requires data at the inflection point, linear growth phase, and asymptote; accuracy is increased when data is continuous across these three important parts of the growth curve. Missing in one or two of these parts can drastically change growth curve reconstructions and give inaccurate

results (Fig. 4.3). Such changes are reflected in the comparison of growth curves between MPC-D 107/2 and FMNH PR 2081 (Fig. 4.2). This limitation is ever present when studying extinct animals as the fossil record creates preservation biases in how common an organism is preserved, which bones from an individual are preserved, and at what life stage an individual is preserved. This study benefits from a robust sample size because *Tarbosaurus* is commonly found in the Nemegt Formation, most specimens of *Tarbosaurus* are known from partial skeletons preserving multiple limb bones that can be examined; and specimens at multiple life stages have been found (Maleev, 1955b), allowing for overlap in growth records. However, some extinct species may only be known from a few or even one specimen and destructive sampling may only allow for growth curves to be based on a single individual. Therefore, future workers should use caution when reconstructing growth curves from a limited sample and be sure to account for uncertainty.

Finally, recent studies reconstructing the growth of extinct theropods, including the study in which these methods are based upon, modeled sexual maturity at 70-80% of the organism's maximum size (Lee & O'Connor, 2013; Prondvai, 2017). These studies assumed, based on their results, that the organism's growth curve was fast growing early in life (Lee & O'Connor, 2013; Prondvai, 2017). However, these results show *Tarbosaurus* to have a much more prolonged life history due to the inclusion of juvenile specimens. Therefore, if sexual maturity is indeed achieved at 75% maximum body size (Lee & O'Connor, 2013), then the models from this study would estimate *Tarbosaurus* achieving sexual maturity anywhere from early 20's to late 40's. This estimation is quite late in life compared to modern organisms who do not have such a prolonged life-history. From this, basing sexual maturity on size may not be an accurate proxy

for extinct organisms; likely sexual maturity correlates with age rather than relative size and would push these estimates for sexual maturity in *Tarbosaurus* to an earlier age and smaller size. However, further testing of the relationship between sexual maturity and age in extant animals is required to support such a hypothesis and falls outside the scope of this thesis

The Life History of *Tarbosaurus bataar*

Contrary to what has been previously published on tyrannosaur growth curves (Erickson *et al.*, 2004; Horner & Padian, 2004; Cullen *et al.*, 2020b) *Tarbosaurus* displays a more prolonged non-rapid growth stage that seems to last until the late teens (Fig. 4.4). Based on best model estimates (Table 3.8), this stage of life is when CGM couplets are first observed in MPC-D 100/62 at age 17 weighing roughly 242 kg as well as MPC-D 107/5 at age 19 weighing roughly 267 kg. When confidence intervals for the age of these individuals are considered (Table 3.8), CGM couplets could hypothetically begin to appear from ages 12-22. This suggests that environmental stressors are more likely to be experienced later in life. Additionally, this time period is when growth rates begin to increase, signifying the transition towards the rapid growth stage. Rapid growth lasts until around age 34, when 75% of maximum size is achieved (Fig. 4.4). This has been shown to closely correlate with sexual maturity (Lee & O'Connor, 2013b; Prondvai, 2017). Based on the differing EFS sizes in MPC-D 107/2 (Table 3.1; 3.2; 3.3), bones achieve skeletal maturity at different points in their growth, some even stopping during the rapid growth phase (Fig. 4.4). The fibula attained skeletal maturity first at age 31, followed by the tibia at age 33, and the femur attained skeletal maturity at age 38 when the individual effectively stops growing.

Within the Nemegt Formation, the prolonged non-rapid growth stage would mean that *Tarbosaurus* would be in a competitive size range with other small sized predators like *Adasaurus* and *Zanabazar* until about five years old and the medium sized predator *Alioramus* until about age 18-20. This age range of equaling and/or surpassing *Alioramus* in size coincides with the earliest onset of CGM couplets, indicating environmental stress, as well as the beginning of rapid growth that defines the end of the non-rapid growth stage. From this evidence, it could be possible that *Tarbosaurus* exhibited parental care for juveniles to reduce competition and stress between similarly sized predators. However, independent testing of ontogenetic changes in skull stress loading and/or isotope levels in tooth enamel would need to be conducted to further support this hypothesis. Additionally, further sampling of skeletally immature *Tarbosaurus* individuals that yield CGM couplets would disprove such a hypothesis.

REFERENCES

- Carr TD, (2020) “*A high-resolution growth series of Tyrannosaurus rex obtained from multiple lines of evidence*” PeerJ 8:e9192 DOI 10.7717/peerj.9192
- Castanet J, Croci S, Aujard F, Perret M, Cubo J, Margerie E de. (2004) “*Lines of arrested growth in bone and age estimation in a small primate: Microcebus murinus.*” Journal of Zoology 263: 31–39.
- Chapelle KEJ, Botha J, Choiniere JN. (2021) “*Extreme growth plasticity in the early branching sauropodomorph Massospondylus carinatus.*” Biol. Lett. 17: 20200843.
<https://doi.org/10.1098/rsbl.2020.0843>
- Cullen TM, Evans DC, Ryan MJ, Currie PJ, Kobayashi Y. (2014) “*Osteohistological variation in growth marks and osteocyte lacunar density in a theropod dinosaur (Coelurosauria: Ornithomimidae).*” BMC Evolutionary Biology 14, 231. (doi:10.7934/p1218)
- Cullen TM, Canale JI, Apesteguía S, Smith ND, Hu D, Makovicky PJ. (2020b) “*Osteohistological analyses reveal diverse strategies of theropod dinosaur body size evolution.*” Proc. R. Soc. B 20202258. <http://dx.doi.org/10.1098/rspb.2020.2258>
- Currie, PJ. (1998). “*Possible evidence of gregarious behavior in tyrannosaurids*” Gaia. 15: 271–277.
- Daffner RH & Pavlov H, (1992) “*Stress Fractures: Current Concepts*” AJR 159:245-252
- Dececchi TA, Mloszewska AM, Holtz TR, Jr., Habib MB, Larsson HCE (2020) “*The fast and the frugal: Divergent locomotory strategies drive limb lengthening in theropod dinosaurs.*” PLoS ONE 15(5): e0223698. <https://doi.org/10.1371/journal.pone.0223698>

Depalma RA, Burnham DA, Martin LD, Rothschild BM, Larson PL, (2013) “*Physical evidence of predatory behavior in Tyrannosaurus rex.*” PNAS 110:31 12560–12564

www.pnas.org/cgi/doi/10.1073/pnas.1216534110

Dortela E, Sardennea F, Bousquet N, Rivot E, Million J, Le Croizier G, Chassot E, (2015) “*An integrated Bayesian modeling approach for the growth of Indian Ocean yellowfin tuna*” Fisheries Research 163 (2015) 69–84 <http://dx.doi.org/10.1016/j.fishres.2014.07.006>

Enlow, D. H. (1963) “*Principles of Bone Remodeling: An Account of Post-Natal Growth and Remodeling Processes in Long Bones and the Mandible*” Charles C. Thomas, Springfield

Erickson, G.M., Makovicky, P.J., Currie, P.J., Norell, M.A., Yerby, S.A., Brochu, C.A. (2004) “*Gigantism and comparative life-history parameters of tyrannosaurid dinosaurs.*” Nature. 430, 772–775

Heck, C.T. & Woodward, H.N. (2021) “*Intrasketal bone growth patterns in the North Island Brown Kiwi (Apteryx mantelli): Growth mark discrepancy and implications for extinct taxa.*” Journal of Anatomy, 00, 1–21. <https://doi.org/10.1111/joa.13503>

Horner, J.R. and Padian, K. (2004) “*Age and growth dynamics of Tyrannosaurus rex.*” Proc. R. Soc. London B Biol. Sci. 271, 1875–1880

Köhler M, Marín-Moratalla N, Jordana X, Aanes R. (2012) “*Seasonal bone growth and physiology in endotherms shed light on dinosaur physiology.*” Nature 487:358–61

Lee & Lee AH, O’Connor PM. (2013) “*Bone histology confirms determinate growth and small body size in the noosaurid theropod Masiakasaurus knopfleri.*” Journal of Vertebrate Paleontology 33:865–76

Maleev, E., (1955b) “*New carnivorous dinosaurs from the Upper Cretaceous of Mongolia*”

Dokladi Akademii Nauk S.S. S.R. ,v. 104,p. 779-782.

Nacarino-Meneses C, Köhler M (2018) “Limb bone histology records birth in mammals.” PLoS ONE 13(6): e0198511. <https://doi.org/10.1371/journal.pone.0198511>

Padian K, Werning S, Horner JR. (2016) “*A hypothesis of differential secondary bone formation in dinosaurs.*” C.R. Palevol 15, 40–48. (doi:10.1016/j.crpv.2015.03.002)

Prondvai E, (2017) “Medullary bone in fossils: function, evolution and significance in growth curve reconstructions of extinct vertebrates” J . EVOL. BIOL. 30 440–460

Rothschild B, Tanke DH, Ford DL. (2001) “*Theropod stress fractures and tendon avulsions as a clue to activity*” In Tanke DH, Carpenter K, editors. Mesozoic vertebrate life. Bloomington: Indiana University Press; pp. 331–336.

Scott, R.D. & Heikkonen, J. (2012) “*Estimating age at first maturity in fish from change-points in growth rate.*” Mar. Ecol. Prog. Ser. 450: 147–157.

Werning S. (2012) “*The ontogenetic osteohistology of Tenontosaurus tilletti.*” PLoS ONE 7:e33539

Woodward HN, Horner JR, Farlow JO. 2014. “*Quantification of intraskeletal histovariability in Alligator mississippiensis and implications for vertebrate osteohistology.*” PeerJ 2:e422 <https://doi.org/10.7717/peerj.422>

Woodward HN, Tremaine K, Williams SA, Zanno LE, Horner JR, Myhrvold N, (2020) “*Growing up Tyrannosaurus rex: Osteohistology refutes the pygmy ‘Nanotyrannus’ and supports ontogenetic niche partitioning in juvenile Tyrannosaurus*” Sci. Adv.; 6 : eaax6250

Zullinger EM, Ricklefs RE, Redford KH (1984) “*Fitting Sigmoidal Equations To Mammalian Growth Curves*” Journal Of Mammalogy 65:4 607-636

Zylstra ER & Steidl RJ, (2020) “*A Bayesian state-space model for seasonal growth of terrestrial vertebrates*” *Ecological Modelling* 420 (2020) 108975

<https://doi.org/10.1016/j.ecolmodel.2020.108975>

FIGURES

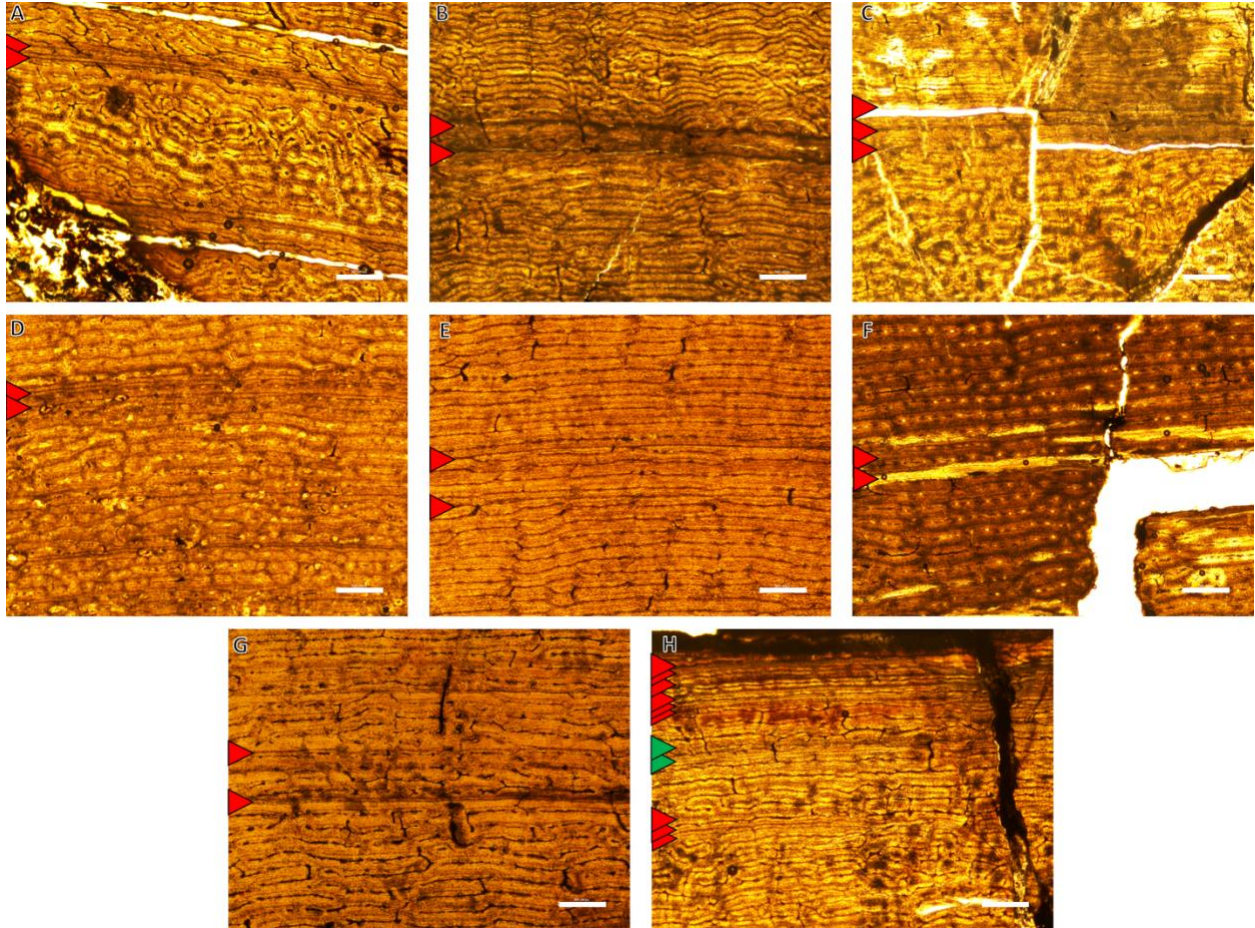


Figure 4.1. Examples of CGM couplet present within the sample. Plain-polarized images of MPC-D 107 femur (A), MPC-D 100/62 tibia (B), 100/70 femur (C), 100/98 femur (D), 100/61 tibia (E), 107/4 tibia (F), 100/64 femur (G), and 107/2 femur (H). Red arrows are LAGs, green arrows are multi-LAGs. Scale bar is 1mm.

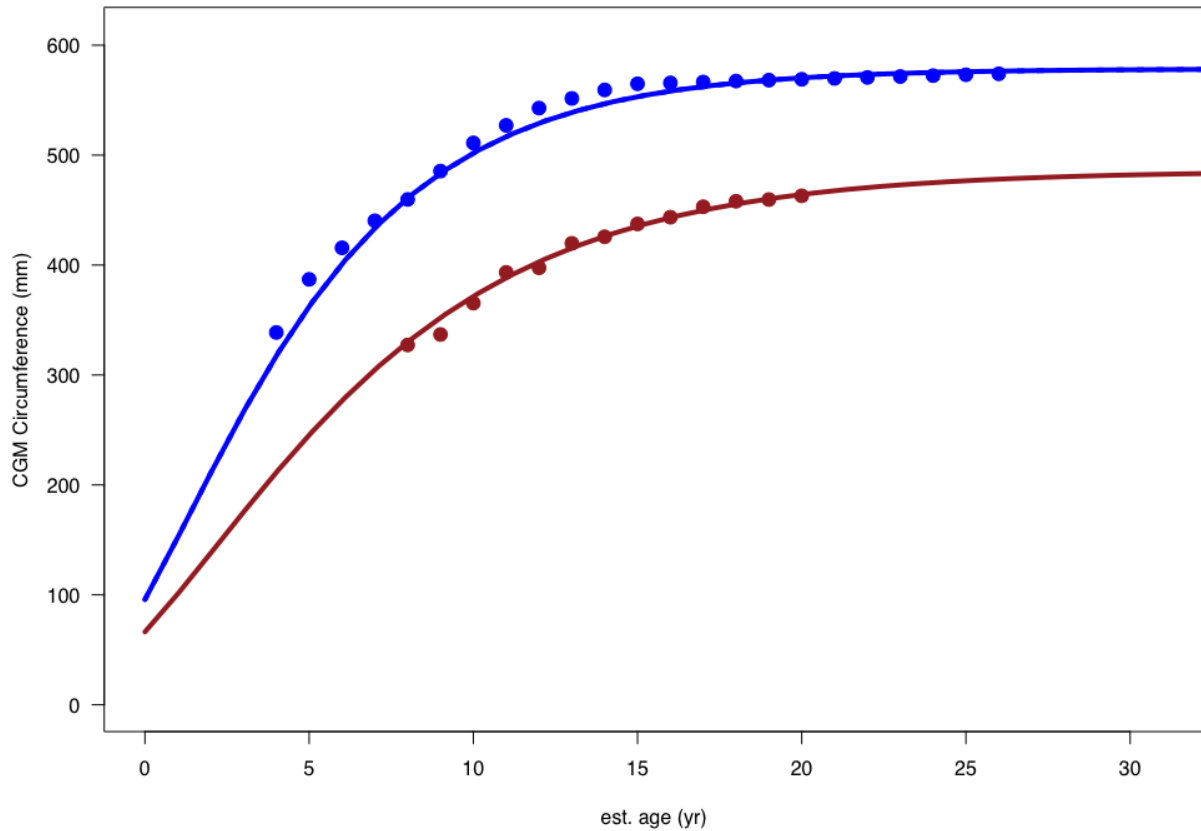


Figure 4.2. Growth curve reconstruction of FMNH PR 2081 (Blue) and MPC-D 107/2 (Brown). *T. rex* matures at roughly the same time as *T. bataar*, yet is significantly larger at maturation, suggesting accelerated growth in *T. rex* compared to its early diverging relative. Note the abbreviated and rapid growth early in life is due to a lack of sampling in skeletally immature individuals.

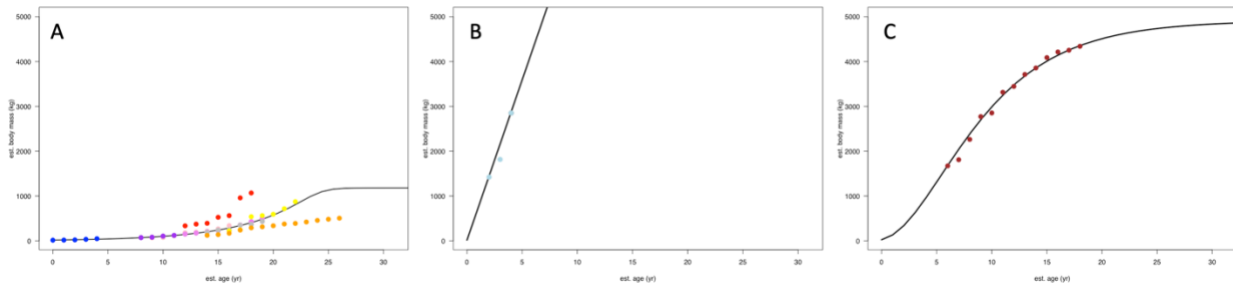


Figure 4.3. Selective sampling of growth data within this sample of *Tarbosaurus*. Reconstructing growth from incomplete data before the growth inflection (A), during the rapid growth phase (B), or at the asymptote (C) can produce biased and incorrect reconstructions.

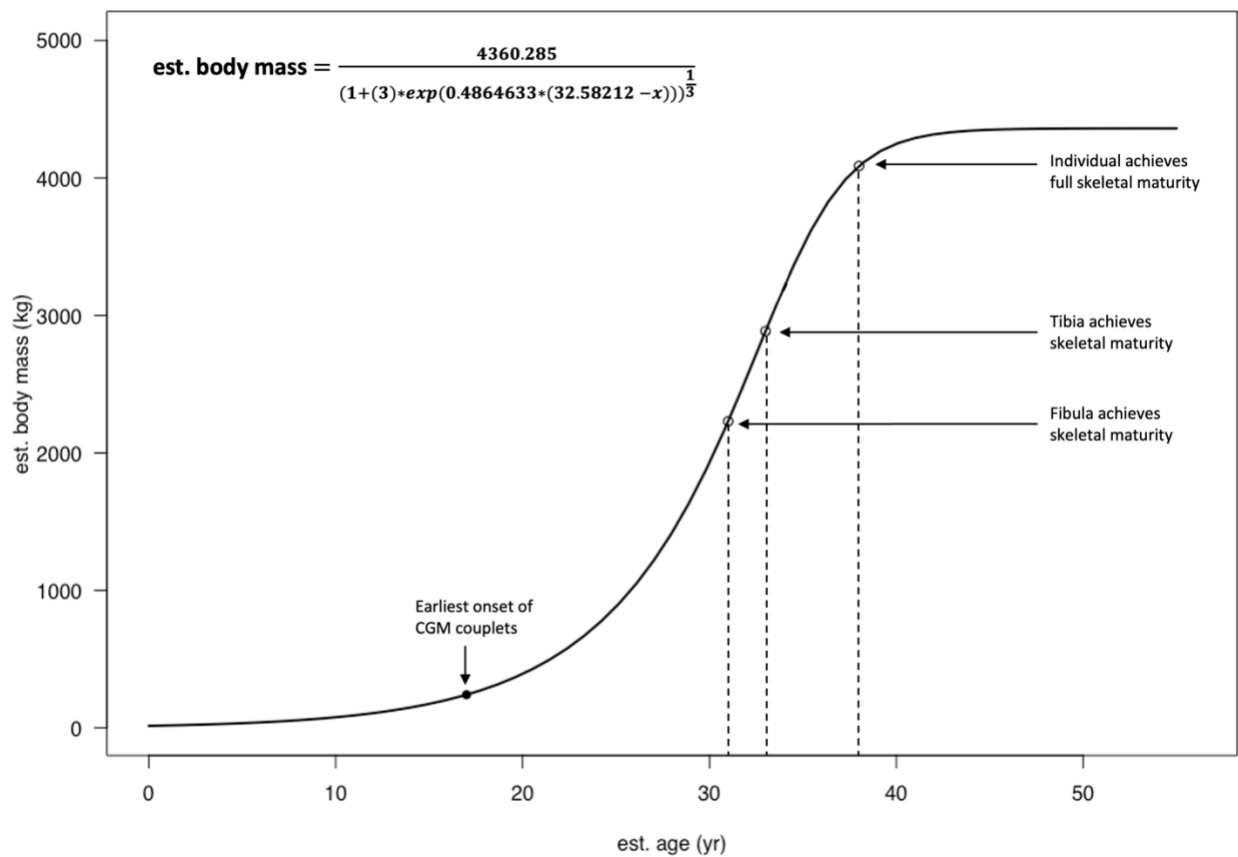


Figure 4.4. Best growth curve reconstruction with important life history events. Formula for growth calculates body mass estimate (kg) from known age determined from the femur.

TABLES

Table 4.1. CGM Types and Amounts Preserved in *Tarbosaurus* Limb Bones

Specimen	Limb Bone	LAGs	Annuli	Max CGM Count (EFS)	Min CGM Count (EFS)
MPC-D 107/7	Femur	3	2	5	5
	Tibia	3	2	5	5
	Fibula	3	2	5	5
MPC-D 100/66	Femur	2	2	4	4
	Tibia	0	5	5	5
	Fibula	2	3	5	5
MPC-D 107/5	Femur	10	0	10	8
	Fibula	4	3	7	7
MPC-D 100/62	Femur	9	0	9	8
	Tibia	8	4	12	10
	Fibula	3	3	6	6
MPC-D 107/14	Femur	5	1	6	6
MPC-D 100/70	Femur	7	2	9	7
	Tibia	10	1	11	11
	Fibula	4	4	8	8
MPC-D 100/98	Femur	13	1	14	13
	Tibia	13	2	15	12
	Fibula	9	7	16	16
MPC-D 100/61	Femur	7	2	9	7
	Tibia	9	2	11	9
	Fibula	4	4	8	7
MPC-D 107/4	Tibia	4	0	4	3
MPC-D 100/64	Tibia	13	1	14	13
	Fibula	9	0	9	9
	Fibula	4	3	7	7
MPC-D 100/63	Femur	N/A	N/A	N/A	N/A
	Tibia	N/A	N/A	N/A	N/A
MPC-D 107/2	Femur	5	9	24 (10)	13 (4)
	Tibia	5	0	14 (9)	14 (9)
	Fibula	3	6	20 (11)	20 (11)

Chapter 5: Conclusion

This multi-element and multi-individual study is the largest histological study to have been conducted on a theropod species. By examining the same limb elements across multiple individuals, my results show that *Tarbosaurus* deposits rapidly growing fibrolamellar tissue for the majority of this species' life history. Growth marks varied significantly across all elements, except for the two youngest specimens, as a result of CGM couplets. These couplets support the idea that CGMs do not deposit exclusively on an annual basis and support growth modulation in tyrannosaurs resulting from environmental stress.

Growth curve reconstructions reveal that the femur, tibia, and fibula of *Tarbosaurus* model unique growth patterns, but all infer exponentially rapid growth post-juvenile stages.

Examination of MPC-D 107/2 suggests that bones achieve skeletal maturity at different ages, with the femora being the last bone to stop growing. Therefore, the femur is the most accurate histological proxy for growth and age estimates. Examination of this individual also reveals age estimates are more constrained when CGM couplets are averaged, thus removing these couplets provides the most accurate record of growth. Our robust sampling across multiple age classes suggest that the juvenile stage is much more prolonged than originally documented and lasts at least 20 years. The shift towards rapid growth also coincides with the onset of CGM couplets within weight-bearing bones. These events may suggest a lack of environmental stress in juvenile *Tarbosaurus* likely the result of parental care.

These results highlight many inherent limitations of histology and the growth curve reconstructions based upon them. Sufficient sampling across multiple elements and multiple

individuals of different yet overlapping ontogenetic stages is crucial as to not introduce bias into results. Additionally, the current lack of knowledge on CGM couplets presents a serious issue when determining the relevance of certain growth marks. Despite this, the current method is the most accurate way thus far to reconstruct growth and measures should be taken to account for uncertainty. Future work on extant animals centered around the ontogenetic relationship between limb-bone scaling and body mass increase as well as the physiological cause and effects of CGM couplets will be instrumental in addressing these limitations.

This study provides the most in-depth analysis of a tyrannosaur's life history to date. Based on previous literature, *Tarbosaurus* experienced peramorphic acceleration in growth rates compared to early-diverging North American taxa. Additionally, based on comparisons between MPC-D 107/2 and FMNH PR 2081, *Tyrannosaurus* exhibits roughly a 30% increase in growth rates compared to *Tarbosaurus*. This has implications for an extreme acceleration of growth rates in late-diverging tyrannosaurs after their introduction to Asia and before their re-emergence in North America. More comprehensive histological sampling across tyrannosaurs has the potential to reveal exaggerated evolution of growth dynamics.

Appendix: Pictures of Limb Bone Samples Before Histological Processing



Figure 5.1. MPC-D 107/7 before histological processing.



Figure 5.2. MPC-D 100/66 before histological processing.



Figure 5.3. MPC-D 107/5 before histological processing.



Figure 5.4. MPC-D 100/62 before histological processing.



Figure 5.5. MPC-D 107/14 before histological processing.



Figure 5.6. MPC-D 100/70 before histological processing.



Figure 5.7. MPC-D 100/98 before histological processing.



Figure 5.8. MPC-D 100/61 before histological processing.



Figure 5.9. MPC-D 107/4 before histological processing.



Figure 5.10. MPC-D 100/64 before histological processing.



Figure 5.11. MPC-D 100/63 before histological processing.



Figure 5.12. MPC-D 107/2 before histological processing.